

1 Title: Oscillations support short latency co-firing of neurons during human
2 episodic memory formation

3
4 Authors: Frédéric Roux¹, George Parish¹, Ramesh Chelvarajah^{1,2}, David T. Rollings², Vijay Sawlani^{1,2}, Hajo
5 Hamer³, Stephanie Gollwitzer³, Gernot Kreiselmeyer³, Marije Ter Wal¹, Luca Kolibius⁴, Bernhard
6 Staresina^{1,5}, Maria Wimber^{1,4}, Matthew W. Self⁶, Simon Hanslmayr^{*1,4}

7
8 **Affiliations:**

9 ¹School of Psychology, University of Birmingham, Birmingham B15 2TT, United Kingdom

10 ²Complex Epilepsy and Surgery Service, Neuroscience Department, Queen Elizabeth Hospital, Birmingham B15
11 2TH, United Kingdom

12 ³Epilepsy Center, Department of Neurology, University Hospital Erlangen, 91054 Erlangen, Germany

13 ⁴Institute of Neuroscience and Psychology, University of Glasgow, Glasgow G12 8QB, United Kingdom

14 ⁵Department of Experimental Psychology, University of Oxford, Oxford, OX2 6GG, United Kingdom

15 ⁶Department of Vision and Cognition, Netherlands Institute of Neuroscience, an institute of the Royal Netherlands
16 Academy of Art and Sciences (KNAW), Amsterdam, the Netherlands

17
18 **Abstract:** Theta and gamma oscillations in the medial temporal lobe are suggested to play a critical role for human memory formation via establishing synchrony in neural assemblies. Arguably, such synchrony facilitates efficient information transfer between neurons and enhances synaptic plasticity, both of which benefit episodic memory formation. However, to date little evidence exists from humans that would provide direct evidence for such a specific role of theta and gamma oscillations for episodic memory formation. Here we investigate how oscillations shape the temporal structure of neural firing during memory formation in the medial temporal lobe. We measured neural firing and local field potentials in human epilepsy patients via micro-wire electrode recordings to analyze whether brain oscillations are related to coincidences of firing between neurons during successful and unsuccessful encoding of episodic memories. The results show that phase-coupling of neurons to faster theta and gamma oscillations correlates with co-firing at short latencies (~20-30 ms) and occurs during successful memory formation. Phase-coupling at slower oscillations in these same frequency bands, in contrast, correlates with longer co-firing latencies and occurs during memory failure. Thus, our findings suggest that neural oscillations play a role for the synchronization of neural firing in the medial temporal lobe during the encoding of episodic memories.

47 **Introduction**
48

49 Episodic memory relies on efficient information transmission within the medial temporal lobe
50 (1-3). More specifically, if one group of neurons drives neural discharges of another group of
51 neurons, synaptic modifications can occur which transform fleeting experiences into durable
52 memory traces (4). The strengthening of synaptic connections between neurons that are active
53 during the experience of an episode depends critically on the temporal structure of neural firing
54 (5-8). Evidence that has accumulated over several decades suggests that coordinated rhythmic
55 activity may provide a candidate mechanism to establish fine-grained temporal structure on
56 neural firing (9-11). Accordingly, brain oscillations at theta (~3 – 9 Hz) and gamma (~ 40 – 80
57 Hz) frequencies in the human medial temporal lobe (MTL) have been proposed to promote the
58 formation of memories through the synchronization of neural firing in the MTL (1, 12-14).

59
60 Studies in animals showed that correlated neural firing is fundamentally involved in the
61 strengthening of synaptic connections (7). Consistent with a critical role of neural
62 synchronization studies in humans using invasive and non-invasive electrophysiological
63 recordings demonstrated that theta and gamma oscillations in the MTL are correlated with
64 memory encoding (1, 15). For instance, stronger phase-coupling of neural firing in theta (16)
65 oscillations has been observed during successful compared to unsuccessful encoding. A similar
66 result has been obtained in macaques for the high gamma oscillations (>60 Hz; (17)).
67 Furthermore, increased cross-frequency coupling between theta-phase and the power of gamma
68 oscillations for successfully encoded memory items has also been reported in the human medial
69 temporal lobe (18, 19). Therefore, it can be hypothesized that increased synchronization between
70 neural spiking and theta and gamma oscillations is positively related to memory encoding,
71 presumably via inducing efficient information transmission between neural ensembles.

72
73 However, efficient information transmission, and synaptic plasticity as a result thereof, may not
74 only be reflected in the absolute level of synchronization, but also in the frequency at which this
75 synchronization occurs. Neurons integrate input over time, with the rate of relaxation of the
76 membrane potential dictating the length of the integration window (10-30 ms for neocortical
77 principal cells; (9)). Relatively faster oscillations integrate neural spikes over shorter time
78 windows compared to relatively slower oscillations. One advantage of such a tighter temporal
79 packing of spikes of an upstream neuron is that it is more likely to overcome the firing threshold
80 of a downstream neuron because the individual spikes build on each other before the membrane
81 potential fully drops back to baseline (20, 21). Therefore, a neural assembly which synchronizes
82 firing at faster oscillations is more likely to drive a down-stream neural assembly compared to
83 synchronization at slower oscillations. This may be the reason for why fast (~65 Hz), but not
84 slow (~40 Hz), gamma oscillations in rodents (22), and humans (23) have been demonstrated to
85 reflect memory encoding processes.

86
87 This study aims to advance our understanding of how brain oscillations within the human MTL
88 mediate neural firing in the service of episodic memory formation. Our understanding of this
89 process is limited because previous studies have either investigated neural oscillations only in the
90 local field potential, or have focused on single frequency bands (i.e., theta or gamma), or have
91 used simple recognition tasks which do not fully tap into the complex association processes
92 underlying episodic memory. A recent study demonstrated a role of sleep spindles for

modulating short-latency co-firing between neurons in the lateral anterior temporal cortex (24), which is consistent with the idea that oscillations in principle can regulate efficient information transfer between neurons. However, little is known about the relevance of such co-firing between neurons or groups of neurons during human memory formation. This study aims to fill these gaps by simultaneously recording LFPs and neural firing in parallel from multiple micro-wire electrodes during an associative episodic memory task (Figure 1A). Our results show that successful memory formation is correlated with spike-LFP coupling at relatively faster theta and gamma oscillations as opposed to relatively slower oscillations. Furthermore, we show that gamma oscillations are coupled to the phase of theta oscillations specifically for successful memory trials, and that successful memory trials are characterized by short-latency co-firing of neurons consistent with synaptic plasticity principles such as spike-timing-dependent-plasticity (STDP)(6).

Results

Memory task and behavior

Nine patients with refractory epilepsy participated in 40 sessions of an associative episodic memory task (Figure 1A). During the encoding phase of the task, the patient was presented with several trials each containing a picture of an animal (cue), which was shown for 2 seconds. Then a pair of images appeared which either showed a face and a place, two faces or two places. The patients were instructed to link the three elements of the episode together by mentally imagining a narrative (e.g. “I saw a tiger in the zoo with Stephen Fry”) and press a button to indicate whether the invented narrative or combination of images was plausible or implausible, then the next trial followed. All images were trial unique. After the encoding phase and a brief distractor test, memory performance was assessed by means of a cued recall test. During the test phase the picture of the animal was presented for 2 seconds and the patient indicated how many stimuli they could remember (0, 1 or 2). If they indicated to remember at least one image then a screen with four images appeared, and the patient selected the two images that they thought were paired with the cue originally. Trials for which both images were correctly recalled are labelled ‘hit’, all other trials (i.e., 1 image or both wrong) are labelled ‘miss’. Therefore, contrasting hits with misses isolates neural processes which support the complete memorization of an episode (as opposed to incomplete memories or no memory at all). Any such process has to start when enough information is available for the patient to imagine the episode, which is at the onset of the paired images (i.e., 2 seconds after the onset of the cue). Therefore, all subsequent analysis focused on the time window that followed the onset of the paired images (2-3 seconds; highlighted in Figure 1A).

On average patients correctly recalled both associated items on 75.43% (s.d.: 13.3) of the trials (Figure 1B). Note that this is well above chance level (16.6%). The remaining miss trials were approximately evenly distributed between incomplete memories (i.e., only one association recalled; 12.6%) or completely forgotten (i.e., both incorrect; 11.9%). Across sessions the proportion of full misses (i.e. both incorrect) was significantly below chance ($t_{39}=-1.92$; $p<0.05$). However, the proportion of fully forgotten trials appears to be higher than expected purely by chance. This is likely driven by a tendency of participants to either fully remember an episode, or completely forget it, as demonstrated previously in behavioral work (25). Investigation of

139 differences between the two types of misses (i.e., both incorrect versus one incorrect) was not
140 feasible due to insufficient trial numbers.

141 **Within-region spike-LFP coupling to fast gamma oscillations correlates with memory**

142 Neural spiking and LFP activity were recorded with Behnke-Fried hybrid depth-electrodes from
143 MTL regions (Figure 1C). Most electrodes (73%) were located in the hippocampus, the rest was
144 located in adjacent MTL regions. Altogether 232 putative single and multi-units were recorded
145 of which 218 were used for further analysis (14 units were rejected because of too low firing
146 rates; see Methods). These units were classified into single-units and multi-units using an
147 automatic procedure based on waveshape homogeneity and inter-spike intervals (26), resulting in
148 82 putative single-units and 136 putative multi-units (Figure 1 – figure supplement 1). Neural
149 firing during encoding was not modulated by memory for the time window of interest (2-3
150 seconds). However, hits showed a sustained increase in firing rate compared to misses at a later
151 time window (>3 seconds; Figure 1 – figure supplement 2). LFPs for hits and misses also did not
152 differ in terms of event-related potentials or inter-trial phase coherence (Figure 1 – figure
153 supplement 3-4). However, expected differences between hits and misses were obtained in broad
154 band power (27), with hits showing decreased low frequency but increased high frequency
155 power.

156 Synchronization of neural firing of a single- or multi-unit to the population activity can be
157 measured with spike-field coupling (SFC). SFC can occur at two different spatial levels, locally
158 (within a region) or distally (across regions; Figure 2A). Locally, SFC indicates the firing of a
159 neuron (or neurons for multi-units) being entrained to its surrounding LFP. Distally, SFC likely
160 indicates that the firing of a neuron (or neurons) elicits post-synaptic currents in another region.
161 Because postsynaptic currents reflect the aggregated input to a neuron, distal spike-field coupling
162 is usually interpreted as a functional measure of connectivity, with the spike providing region
163 being the up-stream sender, and the LFP providing region being the down-stream receiver (28-
164 30). Accordingly, we split spike-LFP pairs into these two categories, i.e., local and distal
165 couplings. SFC was measured with the pairwise phase-consistency index (PPC)(31), which is not
166 biased by the number of observations (e.g., spikes, trials). For distal couplings all possible
167 pairings were considered; that is no constraints were imposed based on anatomy. Connectivity
168 was therefore measured in a purely data-driven way.

169 During the time window of interest (2-3 seconds), 192 significantly (Rayleigh test; $p_{corr} < 0.05$;
170 FDR-correction) coupled spike-LFP pairs were found in the high-frequency range (40-80 Hz), of
171 which 53 were coupled to the local LFP (4.87 % of all possible combinations) and 139 coupled
172 to distal LFPs (2.49% of all possible combinations, Figure 2A). The number of locally coupled
173 pairs was significantly higher than chance (Randomization test; $p < 0.0001$), whereas the number
174 of distally coupled pairs was not ($p > 0.35$). Local spike-field coupling showed a pronounced peak
175 in the fast gamma range (~65 Hz), which was substantially stronger compared to distal couplings
176 (T-test; $p_{corr} < 0.05$; Figure 2B; FDR-correction). When calculating local spike-LFP coupling it is
177 necessary to interpolate spikes to prevent high frequency artefacts (32), however, this
178 interpolation can again potentially introduce artefacts and inflate spike-LFP coupling especially
179 for channels where spikes are coupled to the LFP of that same channel (which were ~20% of the
180 data). To address this issue we split the local spike-LFP coupling data into channel pairs where
181 the spikes and LFPs were measured on the same microwire, and where spikes and LFPs were
182 measured on different microwires (but on the same bundle of B-F electrodes; see Figure 2B,

right). The PPC profile for both was highly similar, suggesting that spike interpolation did not artificially inflate the spike-LFP coupling. Importantly, the peak frequency of local spike-field coupling varied as a function of memory formation such that hits showed stronger spike-field coupling at a higher frequency (~70 Hz) than misses (~62 Hz; T-test; $p_{corr} < 0.05$; FDR-correction; Figure 2C). This effect was also significant when using sessions as random variable (T-test; $t_{19}=2.21$; $p=0.02$; Cohen's $d = 0.49$). A similar yet slightly weaker effect was also observed when excluding data where spikes and LFPs were measured on the same microwire (see Figure 2C, right; T-test; $p_{uncorr} < 0.05$).

This pattern suggests a shift in frequency, with hits showing spike-field coupling at a higher gamma frequency compared to misses. To test whether this shift of gamma frequency occurred consistently across spike-LFP pairs a peak detection analysis was conducted where gamma peak frequencies for hits and misses were extracted and compared for each pair. The results confirmed that hits were characterized by significantly faster gamma frequencies compared to misses (T-test; $t_{36}=1.96$; $p=0.029$; Cohen's $d = 0.32$; Figure 2D - left). Again, excluding data where spikes and LFPs were measured on the same microwire replicated this shift in peak frequency for hits compared to misses ($t_{28}=1.75$; $p=0.045$; Cohen's $d = 0.32$; Figure 2D - right). Figure 2E shows this effect for one example multi-unit, which couples to a slightly slower gamma rhythm for misses compared to hits. A control analysis, which effectively controls for a possible selection bias due to unbalanced trial numbers revealed similar results (Figure 2 – figure supplement 1).

A set of control analyses were carried out to address possible concerns about non-stationarity of the signal. First, we carried out a series of simulations to ensure that the Wavelet filters used here yield correct phase estimates for non-stationary signals (Figure 2 – figure supplement 2). Second, we repeated the analysis using a Hilbert transform instead of a Wavelet transform in combination with a bandpass filter (band-width of 4 Hz for theta and 8 Hz for gamma; see Figure 2 – figure supplement 3). We also analyzed the power spectra of the LFP signal at spike times to ensure the presence of a meaningful physiological signal in the phase providing LFP signal (Figure 2 – figure supplement 4), albeit this is not strictly needed for obtaining meaningful spike-LFP coupling results (33, 34). We also tested whether a similar shift in peak gamma frequency as observed for spike-LFP coupling is present in LFP power, and whether memory-related differences in peak gamma spike-LFP are correlated with differences in peak gamma power (Figure 2 – figure supplement 5). Both analyses showed no effects, suggesting that the effects in spike-LFP coupling were not coupled to, or driven by similar changes in LFP power. In addition, we also repeated the above spike-LFP analyses using only LFPs for ‘silent’ microwires, i.e. channels where no spikes have been detected (Figure 2 – figure supplement 6). Finally, we tested whether the absolute amount of spike-LFP coupling differed between hits and misses by comparing peak PPC values between hits and misses. No significant differences in peak PPCs were observed for the raw PPC values (T-test; $t_{36}=-1.7098$; $p=0.09$) and the selection-bias controlled data (T-test; $t_{36}=1.135$; $p=0.26$).

In the above analysis all MTL regions were pooled together to allow for sufficient statistical power. Results separated by anatomical region are reported in Figure 2 – figure supplement 7 for the interested reader. However, these results should be interpreted with caution because electrodes were not evenly distributed across regions and patients making it difficult to disentangle whether any apparent differences are driven by actual anatomical differences, or idiosyncratic differences between patients.

227 Taken together, the phase of fast gamma oscillations temporally organizes spikes within a
228 region. Later fully remembered episodes (hits) are distinguished from incomplete or forgotten
229 episodes (misses) by the frequency to which spikes are coupled to; with fast gamma oscillations
230 benefiting memory formation, and slow gamma oscillations being detrimental for memory
231 formation. This effect is unlikely to be caused by differences in stimulus evoked activity since
232 neither ERPs nor firing rates showed a memory related difference in the time window of interest
233 (Figure 1 – supplements 2-4).

234

235 Cross-regional Spike-LFP coupling to fast theta oscillations correlates with memory

236 The same spike-field coupling analysis as above was carried out for the low frequency ranges (2
237 – 40 Hz). We identified 103 locally coupled (9.46%), and 387 distally coupled (6.93%) spike-
238 field pairs (Rayleigh-test; $p_{corr} < 0.05$; FDR corrected; Figure 3A). For both local and distal
239 couplings the number of significant pairs exceeded chance level (Randomization test; both
240 $p < 0.0001$). Local couplings showed a peak PPC at around 5 Hz (and another peak at 13 Hz),
241 whereas distal couplings showed a peak at around 8-9 Hz (Figure 3B). Local spike-field
242 couplings were robustly stronger than distally coupled pairs in the beta frequency range (20-30
243 Hz).

244 For local spike-LFP coupling no significant differences ($p_{uncorr} > 0.05$) between hits and misses
245 were observed for the low frequency range. In contrast, distally coupled spike-field pairs showed
246 stronger coupling for hits compared to misses in the fast theta frequency range (8-10 Hz) and
247 higher spike-field coupling for misses compared to hits in the slower theta frequency range (5
248 Hz; Figure 3C, T-test; $p_{corr} < 0.05$; FDR-corrected). The stronger spike-field coupling in the fast
249 theta band for hits compared to misses was also found to be significant when using sessions (T-
250 test; $t_{20}=3.25$; $p=0.002$; Cohen's $d=0.71$) as random variable. No significant differences between
251 hits and misses were obtained for locally coupled spike-field pairs.

252 Like the memory related difference in gamma peak frequency, a shift in peak frequency also
253 drove the memory-related difference in distal theta spike-field coupling. This was confirmed by a
254 peak detection analysis showing that hits exhibited a slightly faster peak in theta spike-field
255 coupling compared to misses (T-test; $t_{206}=3.49$; $p=2.99 \times 10^{-4}$; Cohen's $d=0.24$; Figure 3D). This
256 effect is shown for one example single-unit which is distally coupled to a slow theta oscillation
257 for misses, and to a fast theta oscillation for hits (see Figure 3 – figure supplement 1 for a control
258 analysis on selection bias). As for gamma, control analyses addressing concerns about non-
259 stationarity of the signal and the existence of meaningful theta power in the phase providing LFP
260 signal are shown in Figure 2 – figure supplements 2-3. Like the effects in local gamma coupling
261 these effects are unlikely to be due to changes in stimulus evoked activity (Figure 1 – figure
262 supplement 2-4), and/or due to theta rhythmicity in the spiking of neurons themselves (Figure 3 –
263 figure supplement 4). As for gamma, we also tested whether a similar shift in peak theta
264 frequency is present in LFP power, and whether there is a correlation between the memory-
265 related differences in peak theta spike-LFP and peak theta power (Figure 3 – figure supplement
266 5). Both analyses showed no effects, suggesting that the effects in spike-LFP coupling were not
267 coupled to, or driven by similar changes in LFP power. We also repeated the above analysis for
268 spike-LFP pairs by only using ‘silent’ LFP channels (i.e. channels were no SUA/MUA activity
269 was detected (see Figure 3 – figure supplement 6) to address possible concerns about artefacts
270 introduced by spike interpolation. Finally, we report the distal spike-LFP results separated by

271 anatomical region in Figure 3 – figure supplement 7, which did not reveal any apparent
272 differences in the memory related modulation of theta spike-LFP coupling between regions.

273 To assess the direction of information flow of distal theta spike-LFP coupling, and to test
274 whether this flow of information has any bearing on memory performance, we compared the
275 Phase Slope Index (PSI) between hits and misses. Positive values indicate that the spike
276 providing signal is the sender and the LFP providing signal is the receiver and vice versa. The
277 results indicate above chance PSIs for hits peaking in the fast theta band (7-8 Hz). In addition,
278 hits show significantly higher PSIs compared to misses (Fig. 4), whereas PSIs for misses do not
279 differ from zero. PSI results separated by anatomical regions are reported in Figure 4 – figure
280 supplement 1, which revealed that the PSI results were mostly driven by within regional
281 coupling.

282 In agreement with the results obtained for local gamma oscillations we observed that distal theta
283 spike-LFP coupling varied as a function of memory formation, with hits showing spike coupling
284 at faster theta peak frequencies compared to misses. Thus, the present findings reveal two
285 distinct cell populations that synchronize either to local gamma rhythms or distal theta rhythms,
286 and a functional relationship between the peak frequency of gamma and theta phase coupling and
287 memory formation. Importantly, directional coupling analyses demonstrate that the spike
288 providing signal is the upstream sender and the LFP providing signal is the downstream receiver.
289 This result likely does not indicate that one single neuron can drive the entire LFP in a receiving
290 region. Instead, it likely indicates that the spikes of a large population of neurons, of which we
291 happen to sample one, provide input to a receiving region. This direction of information flow
292 was dependent on memory success, suggesting that successful memory formation correlates with
293 efficient cross-regional information transfer.

295 Theta and gamma oscillations are coupled for hits but not for misses

296 The above results show that successful memory formation relies on gamma oscillations
297 synchronizing neurons at a local level, and theta oscillations at ~8 Hz synchronizing neurons
298 across regions. Intriguingly, peak frequencies of both oscillations showed a similar relationship
299 with memory formation, with faster frequencies being associated with successful memory. This
300 raises the question of whether gamma and theta oscillations are also temporally coordinated. For
301 this analysis we considered electrodes from regions where the LFP was locally coupled to spikes
302 in the gamma range and distally coupled to spikes in the low frequency (theta) range. More than
303 half of the electrodes (58%) were available for this analysis (Figure 5A). Cross-frequency
304 coupling was calculated by means of phase-amplitude coupling using the modulation index (35).
305 Importantly, theta and gamma frequencies were adjusted to their peak frequency (see methods)
306 for each condition to account for the systematic difference in peak frequencies between hits and
307 misses and to ensure the presence of a physiologically meaningful oscillation in both conditions
308 (36)(see also Figure 2 – figure supplement 4, and Figure 3 – figure supplement 3). Theta phase to
309 gamma power coupling was evident in single trials (Figure 5B-C). Hits showed stronger theta
310 phase to gamma amplitude coupling compared to misses (Figure 5D; Wilcoxon test; $z=3.7$;
311 $p=8.92*10^{-5}$, Cohen's $d=0.39$). This increased cross-frequency coupling for hits compared to
312 misses was also significant when pooling the data across sessions (Wilcoxon test; $p=0.0386$;
313 Cohen's $d=0.41$). Cross-frequency coupling can be subject to several confounds, which we
314 addressed by a series of control analyses (see Methods and Figure 5 – figure supplement 1). We

315 also analyzed whether the memory-dependent effects of cross-frequency coupling differ between
316 anatomical regions (see Figure 5 – figure supplement 2). This analysis revealed that the results
317 were mostly driven by the hippocampus, however we urge caution in interpreting this effect due
318 to the large sampling imbalance across regions. Finally, to address concerns about possible
319 broadband power artifacts introduced by spike interpolation we replicated the results by
320 excluding high-frequency power providing channels with SUA/MUA activity (see Figure 5 –
321 figure supplement 3).

322

323

324 **Short co-firing latencies predict successful memory formation**

325 One effect of the relative frequency increase of theta/gamma oscillations may be a more efficient
326 transmission of information between neural assemblies. This can be demonstrated by considering
327 two neurons which both have the same preferred phase of firing (e.g. maximal excitation), and
328 which are both coupled by an oscillation with a constant phase lag of $\pi/4$ (with neuron 1 leading
329 and neuron 2 lagging). If the two neurons are coupled at a frequency of 8 Hz, then neuron 2
330 would fire ~ 31 milliseconds after neuron 1 (i.e., 8 Hz equals a period length of 125 ms, divided
331 by 4 = 31.25). If the neurons are, however, coupled at 4 Hz then neuron 2 would fire ~ 62
332 milliseconds after neuron 1. To test this hypothesis, we analyzed neural co-firing at different
333 time lags by computing the cross-correlation of spike trains between theta up-stream single-
334 /multi-units (i.e., the distally coupled unit) and their corresponding gamma down-stream single-
335 /multi-unit (i.e., the locally coupled unit; Figure 6A). Overall, 32 pairs were available for this
336 analysis, 24 of which showed above threshold co-firing (see Figure 6 – source data 1 for detailed
337 information about each pair). Cross-correlations for hits and misses were each compared to a
338 trial-shuffled baseline and transformed to z-scores effectively eliminating biases introduced by
339 different trial numbers.

340 Compared to baseline, hits showed significant above chance co-firing at lags 20–40ms, whereas
341 co-incidences for misses peaked at 60 ms (T-test; $p_{corr} < 0.05$; FDR-correction; Figure 6B). In
342 addition, hits showed stronger co-firing compared to misses at 20 ms (T-test; $p_{corr} < 0.05$; FDR-
343 correction; Figure 6B). A peak detection analysis revealed that co-firing for hits peaked
344 significantly earlier compared to misses ($t_{21} = -3.201$; $p = 0.004292$; Cohen's $d = -0.68$; Figure 6D).
345 This result held also when using a more conservative approach, i.e., pooling the data across
346 number of single-/multi-units ($t_{11} = -3.337$; $p = 0.00663$; Cohen's $d = -0.96$). Intriguingly, this
347 memory related co-firing effect was observed only when selecting pairs of single-/multi-units
348 that were both locally coupled to gamma, and distally coupled to theta. Analyzing all possible
349 pairs of distally coupled theta units showed no differences in peak co-incidences between hits
350 and misses ($t_{126} = -0.78$; $p = 0.432$). In addition, a completely unconstrained co-firing analysis
351 where all pairs possible pairings of units were considered also showed no systematic difference
352 in co-firing lags between hits and misses (Figure 6 – figure supplement 1). This is quite
353 remarkable given that statistical power for these latter two analyses was substantially higher.
354 This pattern of results suggests that the coupling of down-stream neurons to local fast gamma
355 oscillations is crucial for observing the memory dependent effect of co-firing at critical time
356 windows. To test for a similar effect in the reverse direction (i.e., local gamma coupled unit -->
357 distal theta coupled unit) the same co-incidence analysis was carried out for negative lags.
358 Intriguingly, misses showed peak co-firings at shorter negative latencies (i.e., closer to 0)

359 compared to hits (Figure 6 – figure supplement 2; $t_{14}=-2.866$; $p=0.0124$; Cohen's $d= -0.74$). This
360 result is consistent with the STDP framework, whereby a negative time lag leads to a decrease of
361 synaptic connectivity (5, 6). As for the above analysis we also investigated any apparent
362 differences in co-firing between anatomical regions. These results are reported in Figure 6 –
363 figure supplement 3 and show that the earlier co-firing for hits compared to misses was
364 approximately equivalent across regions. The co-firing analyses were replicated with different
365 smoothing parameters (see Figure 6 – figure supplement 4). No significant differences in firing
366 rates between hits and misses were found ($p>0.3$), and on correlations between firing rates and
367 the co-firing latencies were obtained ($R=-0.06$; $p>0.7$), suggesting that firing rates had no
368 influence on the observed co-firing differences between hits and misses.

369 Together, these results suggest that successful memory formation correlates with shorter
370 latencies of co-firing between down-stream and up-stream neurons. Notably, this effect is
371 selective for pairs of single-/multi-units that are both distally theta coupled and locally gamma
372 coupled.

374 Discussion

375 We investigated neural firing, spike-LFP coupling and co-firing of single-/multi-units during the
376 early encoding stage of complex associations into episodic memory. Our results demonstrate that
377 successful memory formation during this early stage is correlated with a fine-grained pattern of
378 local and distal neural synchronization reflected predominantly in theta and gamma oscillations.
379 On a local level, neural firing coupled to relatively fast gamma oscillations predicts memory
380 success, whereas coupling to relatively slower gamma oscillations predicts memory errors. A
381 similar relationship was obtained on a distal level (i.e., spikes and LFPs recorded from different
382 electrodes) where coupling at relatively faster theta oscillations occurred during hits and
383 coupling at relatively slower theta oscillations was observed during misses. Directional
384 connectivity analyses suggested that the single-/multi-units were the up-stream sender and the
385 LFP the down-stream receiver. Furthermore, gamma oscillations were coupled to the phase of
386 theta, particularly for hits but not for misses, suggesting that successful memory formation is
387 related to the coordination between the two oscillations. Finally, and most crucially, we found
388 that the co-firing of pairs of single-/multi-units was correlated with memory formation such that
389 co-firing at short but not long latencies predicted successful memory. These findings link theta
390 and gamma oscillatory dynamics to neural firing and are consistent with current theories that
391 emphasize the role of oscillations for synchronizing neural assemblies to support memory
392 processes (1, 9, 12, 15).

393 Enhanced local spike-LFP coupling for later successfully recognized pictures in the high gamma
394 but not low gamma band has been observed in the hippocampal formation of macaques (17). We
395 replicate this finding here in humans with an associative episodic memory task. However, in
396 contrast to this previous study we observed a shift in the peak gamma frequency rather than just
397 an increase in spike-LFP coupling which could be due to differences in the task requirements,
398 recording location, analysis techniques or species-specific differences. Other studies in rodents
399 have identified different roles for fast vs slow gamma oscillations in the hippocampus, with fast
400 gamma oscillations reflecting the routing of information into the hippocampus and slow gamma
401 oscillations reflecting the routing of information out of the hippocampus (22). Consistent results
402 were obtained in humans showing that fast gamma oscillations positively predict encoding,

whereas slow gamma oscillations positively predict retrieval of memories (23). Our results are consistent with these studies in suggesting that relatively fast gamma oscillations, but not slow gamma oscillations, are beneficial for memory encoding, and demonstrate this phenomenon on the level of spike-LFP coupling. As suggested in theoretical papers (9, 12) the coupling of spikes at fast gamma oscillations may support memory formation because of the precise temporal packaging that it entails. Such tighter temporal compression of spikes increases the chances of an up-stream neural assembly to drive their down-stream partners (9). Indeed, this was observed in the co-firing analysis where we found shorter co-firing lags for successful memory trials compared to unsuccessful memory trials. To this end, our results are consistent with the idea that fast gamma oscillations correlate with more efficient neural communication, therefore supporting memory formation processes. However, it must be acknowledged that our results do not show a direct correlation between gamma oscillations and the lag of co-firing, let alone a causal role of fast gamma oscillations for short latency co-firing. Such relationships should be investigated in future studies.

Paralleling the results for local gamma spike-LFP coupling a frequency shift was also observed for distal theta spike-LFP couplings. Here, coupling at relatively faster theta oscillations correlated with later memory success, whereas coupling at relatively slower theta oscillations correlated with memory errors. Dissociations between slow and fast theta oscillations in humans have been reported previously (37, 38), albeit slow theta in these studies was considerably slower than reported here (i.e., ~2-4 Hz as opposed to 4-6 Hz). Therefore, the relatively slower theta reported in the current experiment may not reflect this classic slow theta frequency band (39). Instead, they may reflect frequency differences of spike-LFP coupling within the faster theta (4-10 Hz) band which may change as a function of cognitive states, such as memory outcome. It is well documented that the frequency of theta correlates positively with running speed in rodents (40) and humans (38), and that running-speed induced changes correlate with memory outcome (41). A recent theoretical paper speculated that variations in running speed in rodents may reflect different levels in excitatory input to the hippocampal system, which in humans can be equated with attention (42). It is therefore conceivable, and consistent with computational modelling studies (43), that the frequency of theta is subject to modulation of the level of excitation or cognitive states which correlate with memory outcome. On a functional level, an increase of frequency in theta spike-LFP coupling could have the same role on neural signal transmission as observed for gamma, i.e., enhancing the likelihood of an up-stream sender to drive their down-stream partners by temporal compression of spikes. Consistent with this interpretation increased directional coupling from spikes to LFPs was observed for theta for successful memory trials (Fig. 4). This result is in line with previous studies demonstrating a crucial role of inter-areal theta phase synchronization for memory formation (3). However, no attempt was made here to analyze long-range connectivity in a fine-grained anatomical manner, i.e. by differentiating between hippocampal subfields or layers due to difficulties in asserting the exact locations of microwires. Instead, connectivity patterns between spike providing and LFP providing electrodes were analyzed in a purely data-driven way. This is a limitation that should be addressed by future studies using sophisticated localization techniques.

Theta and gamma oscillations not only showed parallel relationships between spike-LFP frequency and memory, but also demonstrated cross-frequency phase-to-amplitude coupling. Gamma amplitude co-fluctuated with theta phase with the degree of this cross-frequency coupling being positively related to memory (i.e., stronger theta-gamma coupling for hits

448 compared to misses). This result is in line with a previous study reporting similar results (19) and
449 extends these findings to microwire recordings and links it with spike-LFP coupling.
450 Furthermore, this result shows that the amplitude of local gamma oscillations rhythmically
451 synchronizes to the phase of theta which mediates neural synchrony between regions,
452 particularly if memory formation is successful. This result is consistent with current network
453 models where fast oscillations regulate local connectivity, slower oscillations regulate long-range
454 connectivity, and cross-frequency coupling enables efficient interfacing between the local
455 gamma and the long-range theta networks (44-46).

456 The net result of a tighter synchronization of spikes locally at gamma, distally at theta, and
457 increased synchronization between theta and gamma, is likely to be increased efficiency in
458 neural communication. One way to quantify the efficiency of neural communication is to
459 measure the time it takes for an up-stream neural assembly to drive their down-stream partners.
460 Indeed, we observed that co-firing between neurons occurred at earlier lags for successful
461 memory trials compared to erroneous memory trials. On a synaptic level such co-firing at earlier
462 lags would lead to a strengthening of synaptic connections with the amount of strengthening
463 decaying exponentially with the lag – known as spike-timing-dependent-plasticity (6). These
464 results are consistent with previous findings (24) and support the idea that oscillations play a
465 crucial role for memory formation because they enable efficient signal transmission and thereby
466 affect synaptic plasticity (1, 9, 12).

467 The idea that synchronized inter-regional oscillations reflect effective communication has
468 recently been questioned by a study showing that inter-regional phase synchronization can be a
469 consequence rather than the cause of connectivity (47). Oscillatory activity in a local circuit will
470 be reflected in postsynaptic activity (i.e. the LFP) of any area that it projects to. Consequently,
471 giving rise to phase locking in the LFP between the two areas which highlights a weakness of
472 LFP based connectivity measures and raises the need for additional methods to disambiguate
473 between scenarios where oscillations establish communication between regions, and where they
474 simply are a consequence thereof. To this end, we not only report a memory dependent shift
475 from slower to faster frequencies in theta and gamma spike-LFP coupling, but critically also
476 report a memory dependent shift in spike-to-spike coupling, with hits showing earlier co-firing
477 compared to misses. This finding is consistent with the idea that nested coupling of fast theta and
478 gamma oscillations enable efficient neural communication. However, whether this shift of co-
479 firing lag is caused by a speed up of theta and gamma oscillations remains an open question.

480 Notably, the neural co-firing analysis indicates a bidirectional flow of information between the
481 hippocampus and surrounding MTL areas, such as the entorhinal cortex (see Figure 6 – figure
482 supplement 3; Figure 6 – source data 1). This result parallels other studies in humans showing
483 that successful encoding of memories depends not only on the input from surrounding MTL
484 areas into the hippocampus, but also on the output of the hippocampal system into those areas,
485 and indeed on the dynamic recurrent interaction between these input and output paths (48, 49).

486 Our study also has several limitations and caveats that need to be considered when interpreting
487 the results. First, sample size of patients is relatively low ($N=9$), however, not unprecedented in
488 the field; a seminal study showing increased theta phase coupling of neural firing for later
489 successfully remembered items reported 9 patients and 14 sessions (16). To offset the low N in
490 patients several sessions were carried out per patient yielding 40 sessions overall. Second, single-
491 units and multi-units were analyzed together. This was necessary because of the limited number

of recorded single-units. Therefore, we cannot disambiguate between synchronization of neural populations or individual neurons, which is particularly relevant for the co-firing analysis. As a result, we cannot infer whether the observed oscillations co-occur with synchronized firing of pairs of individual neurons, or synchronized firing between cell assemblies. Third, all effects reported here were observed in a relatively early time window, i.e., the first second after the stimuli appeared on the screen (2-3 seconds after cue-onset; see Fig. 1A). This analysis window was chosen because it reflects the earliest possible time point when memory formation can happen, i.e., when the full information of the memory is presented. This might indicate that the observed differences between correct and erroneous memory trials reflect initial memory processing steps such as the routing of information into the appropriate MTL regions. Interestingly, these early modulations of neural synchronization by memory encoding were observed in the absence of modulations of firing rates, which is consistent with previous results in humans (16) and macaques (12), but contrasts with Zheng et al. (50). Studies in macaques showed that attention increases spike-LFP coupling whilst not affecting firing rates (51). It is therefore conceivable that these initial network dynamics reflect attentional processes, which act as a gate keeper to the hippocampus and thereby set the stage for later memory forming processes (52). However, the observed synchronization processes may be less reflective of the actual binding process per se, linking the stimuli into a coherent memory trace which supposedly happen at later processing stages (18). Further experiments are needed to address these issues in detail.

Materials and Methods

Patients

Nine patients with refractory epilepsy volunteered to participate in the experiments. Mean age of patients was 37 years (s.d.: 9.1; range: 26-53). All but two patients were right-handed. On average patients suffered 15.6 years from epilepsy. All patients had temporal lobe epilepsy with either a left (N=3), right (N=3) or bilateral focus (N=3). Each patient participated in at least one experimental session, and in most cases more than one session such that overall data from 40 sessions was available for analysis.

Patients were treated in one of three hospitals, the Queen Elizabeth University Hospital Birmingham (N=6), the Epilepsy Centre at the University Hospital in Erlangen (N=1), or the Vrije Universiteit Medisch Centrum Amsterdam (N=2). Ethical approvals were given by National Research Ethics Service (NRES), Research Ethics Committee (Nr. 15/WM/0219), the ethical review board of the Friedrich-Alexander Universität Erlangen-Nürnberg (Nr. 124_12 B), and the Medical Ethical Review board of the Vrije Universiteit Medisch Centrum (Nr. NL55554.029.15), for Birmingham, Erlangen and Amsterdam respectively. Informed consent to participate in the experiments and consent to publish the results was obtained from the patients prior to data collection.

Task and procedure

All participants completed at least one session of an associative episodic memory task which required patients to form trial unique associations between three images (Figure 1A). In one

session, several blocks of the memory task were carried out. One block comprised of three phases, an encoding phase, a distractor phase and a recall phase. During encoding, participants were first presented with an image cue of an animal for 2 seconds, followed by a pair of 2 images made up of any combination of a well-known face or a well-known place (i.e., face-place, face-face, or place-place pairs; presented for 2 s). The initial number of trials was set according to the patient's cognitive abilities as estimated by the experimenter. This number was then reduced if the hit rate fell below 66.25%, or increased if the hit rate surpassed 73.75%, effectively adjusting task difficulty according to the participant's ability. On average, participants completed 19.1 trials (S.D.: 10.3; range: 2-82) per block. Participants were asked to vividly associate these triplets of images. Participants were encouraged to make up a story, which would link the three images to help them memorize the associations. For each triplet, participants were asked whether the story they came up with (or combination of pictures) was plausible or implausible. This plausibility judgment was used to keep participants on task rather than to yield a meaningful metric. Participants were self-paced in providing a judgment, and the following trial began immediately afterward. After encoding, the distractor phase was carried out which required participants to make odd/even judgments for 15 sequentially presented random integers, ranging from 1 to 99. Feedback was given after every trial. After completion of the distractor task, the retrieval phase commenced. Participants were presented with every animal image cue that was presented in the earlier encoding stage and, 2 s later, were asked how many of the associated face or place images they remembered (participants had the option of responding with 0, 1, or 2). If the participant remembered at least 1 image, they were then asked to select the pair of images from a panel of 4 images shown during the previous encoding block (2 targets and 2 foils). The experimental script did not log how many images the patient indicated that they thought to remember. Foils were drawn from images, which were also presented in the preceding encoding phase but were paired with a different animal cue. Image positions on the screen were randomized for each trial. Therefore, a given association could either be remembered completely (i.e., both images correctly identified), remembered partially (i.e., only one image correctly identified), or fully forgotten (i.e., no image recalled or both incorrect).

Notably, the chance level in this task is 16.6%, and not 50% as one might initially assume. This is because the participant selects two stimuli out of 4 in two sequential steps. The chance of getting the first stimulus correct is 50% (i.e., 2 out of 4). The chance of getting the second stimulus also correct is 33% (i.e., 1 out of 3). The combined probability for both choices being correct therefore is $0.5 * 0.3 = 0.166$ or 16.67%. Similarly, the chance of getting both stimuli incorrect is also 16.67%. Getting one stimulus correct is the most probable outcome with a likelihood of 66.67 %. Therefore, partial hits/misses (i.e., 1 correct, 1 incorrect) are likely to also contain a high proportion of lucky guesses. Partial hits/misses and full misses were combined into one miss category. Participants were self-paced during the recall stage, though the experiment ended after a runtime of 40 min in total. All participants completed the task on a laptop brought to their bedside.

Recording Data

To record behavioural responses and to present instructions and stimuli, a Toshiba Tecra laptop (15.6 inch screen) was used in the hospitals in Birmingham and Erlangen. In Amsterdam, an ASUS laptop was used (15.6 inch screen). All laptops operated on Windows 7, 64-Bit.

582 Psychophysics Toolbox Version 3 (53) was used with MATLAB 2014 or MATLAB 2009b
583 (Amsterdam). For responses, the following buttons were used: up-down-left-right arrows to
584 select the images during the recall phase, and the ‘End’ key on the Numpad was used to confirm
585 the selection. During encoding the ‘up’ and ‘down’ arrow keys were used to give the
586 plausible/implausible ratings, respectively. During the distractor phase the ‘left’ and ‘right’
587 arrow keys were used to give the odd/even judgements, respectively.

588 Electrophysiological data were recorded from Behnke-Fried hybrid micro-macro electrodes (Ad-
589 Tech Medical Instrument Corporation, Oak Creek, WI). Each Behnke-Fried hybrid electrode
590 contained 8 platinum-iridium high impedance microwires with a diameter of 38 µm, and one low
591 impedance microwire with the same diameter extending from the tip. Different referencing
592 schemes were used across the hospitals/patients in order to yield the best signal-to-noise ratio in
593 the different environments (i.e., yield highest number of visible spikes in raw data). For 5
594 patients the high-impedance contacts were referenced against either a low-impedance microwire
595 or macro-contact, thus yielding a more global signal. For the remaining 4 patients high-
596 impedance contacts were referenced against another “silent” (i.e., containing no visually
597 detectable spikes) high impedance wire, thus yielding a more local signal. As part of the pre-
598 processing data were re-referenced to yield a comparable local referencing scheme across all
599 datasets (see below). The data were recorded continuously throughout the experiment on an
600 ATLAS Neurophysiology system (Neuralynx Inc.) with a sampling rate of 32 kHz (Birmingham
601 and Amsterdam) or 32.768 kHz (Erlangen) and stored as a raw signal for processing and
602 analysis.

603 Data Analysis

604 The code used for data analysis is available at <https://osf.io/fngz8/>.

605 **Behaviour:** Neural activity during the encoding phase was separated into hits and misses
606 according to memory performance in the subsequent recall phase. Hits constitute trials where
607 both items were later correctly retrieved (i.e., complete memory); Misses constitute trials where
608 at least one item was remembered incorrectly or where the patient indicated that they did not
609 remember any item (i.e., incomplete memories or fully forgotten). Reaction times of the
610 plausibility ratings indicate the time from onset of the cue (i.e., animal image) to the button press
611 and were calculated per subject by using the median across trials. Reaction times were 15.01
612 seconds on average (s.d. 5.79) for hits and 15.26 seconds misses (s.d. 6.85) and did not differ
613 significantly ($t_8=0.44$; $p>0.5$).

614 **Electrode localization:** Electrodes were localized for using one of the following procedures. For
615 patients recorded in Birmingham and Erlangen, pre- and post-implantation T1 structural MRIs
616 (MP-Rage) were co-registered and normalized to MNI space using SPM8
617 (<https://www.fil.ion.ucl.ac.uk/spm/software/spm8/>). If both scans were available the
618 normalization parameters were estimated on the pre-implantation MRI, and these parameters
619 were then applied on the post-implantation MRI. For two patients, only the post implantation
620 MRI was available. For these two patients normalization parameters were estimated and applied
621 to this post implantation MRI. The location of the microwire bundle was either clearly visible as

627 an image artifact in the post implantation MRI. If not, then the location of the microwire bundle
628 was inferred visually by extrapolating the electrode trajectory by 5 millimetres.

629 For patients recorded in Amsterdam pre-implantation structural T1 scans and post-implantation
630 CT scans were available. These were overlaid and normalized using the same procedure as
631 described above using SPM8. The microwire contacts were clearly visible in the CT scans,
632 therefore the location could be estimated directly in all cases.

633 **Spike Sorting:** Spikes of recorded neurons were extracted offline from high-frequency activity
634 (500Hz-5kHz). Spike detection and sorting was done using Wave_clus (54). All units with at
635 least 50 spikes in either condition (hits, misses), a mean spike count > 2 and mean firing rate > 1
636 Hz during the encoding period (0-4s) were submitted to further analysis. The resulting units were
637 further visually inspected to reject noise based on waveshape, spike distribution across trials, and
638 inter-spike intervals. Across all patients and sessions 218 units were retained for analysis. As a
639 final step units were classified into single-units and multi-units following an automatic procedure
640 developed by Tankus et al. (26), which has been shown to closely match classification of trained
641 researchers. This algorithm uses two criteria to classify units, which are inter-spike intervals
642 (ISIs) and variability of the spike waveshape. Concerning the first criterion, a given unit is
643 classified as a multi-unit if more than 1% of ISIs are smaller than 3ms (which would violate the
644 refractory period of firing of neurons). For the second criterion, the variability of the spike
645 waveshape is computed in the time window of the rising flank of the spike waveshape (see
646 Figure S1B). The end of the rise time was the peak of the spike waveshape. The beginning of the
647 rise time was estimated following the procedure described in Tankus et al. (26) using the time-
648 point of the maximum curvature (i.e., second derivative) within an area at the start of the spike
649 wave-shape. Spike waveshape variability (i.e., criterion 2) was then calculated by dividing the
650 sum of the standard deviation by the height of the spike wave.
651

$$c2 = \frac{\sum_i^j s(t_i)}{m(t_j) - m(t_i)}$$

652 Where i = start of the rise time and j = end of the rise time, and m = voltage at time t. This
653 second criterion, c2, can be understood as the inverse of the signal-to-noise ratio where a low
654 value means low variability in spike waveshape. Following Tankus et al. (26) we labelled a
655 given unit as a SU if c2 was < 3. The distribution of both criteria across all units is shown in
656 Figure S1A; waveshapes and ISIs for representative SUs and MUs are shown in Figure S1C.
657

658 **Firing Rate and Spike Density:** Time stamps of spikes during the encoding phase were extracted
659 and converted to continuous time series containing 0s (no spike) and 1s (spike) at a sampling rate
660 of 1kHz. These time series were cut into trials with a duration of 14 seconds centred to cue onset
661 (i.e., animal image), starting at -7 seconds. These trial-based spike time series were then
662 convolved with a gaussian window of 250 ms length to yield spike density time series per trial.
663 These trial-based time series were averaged separately for hits and misses. Finally, a
664 normalization procedure according to (55) was carried out to account for the vast variability of
665 firing rates between neurons (some neurons fire very sparsely whereas other fire at a very high
666 rate). Normalized firing density was calculated according to the formula below, where z (t) =
667 normalized firing rate, sd(t) = spike density, $\mu(bl)$ = mean spike density in baseline interval,
668 $\sigma(bl)$ = standard deviation of spike density in baseline interval, and λ = regularization parameter
669

671 (set to 0.1; see (55)). This regularization parameter was necessary to avoid extreme values for
672 cases where no or only few spikes were present in the baseline. The baseline interval was set to -
673 1000 ms to -125 ms (i.e., half of the Gaussian window length).

674

$$z(t) = \frac{sd(t) - \mu(bl)}{\sigma(bl) + \lambda}$$

675

676 LFP pre-processing: The continuous raw data was imported using the Neuralynx data reader
677 provided by U. Rutishauser (7th release,
678 <https://www.urut.ch/new/serendipity/index.php?/pages/nlxtomatlab.html>). A Butterworth low-
679 pass filter was applied (filter order 2) at 300 Hz. In some channels/sessions an artifact from the
680 TTL pulse was visible, which was removed by subtracting the average artefact from the single
681 trial using a linear regression. Spikes were removed by linearly interpolating the signal from 2
682 ms before the spike to 6 ms after the spike (32). Line noise at 50 Hz was removed using a
683 template subtraction method. This method estimates the line noise signal by fitting a sinusoid at
684 noise frequency and then subtracting it from the signal. Because the line noise can be assumed to
685 be stationary (whereas brain signals are not stationary) this approach effectively removes line
686 noise whilst retaining physiological activity. This approach is therefore preferable to a band-stop
687 filter, which does not retain physiological activity at line noise frequency. Finally, the continuous
688 LFP data was segmented into epochs of 14 seconds duration centred at cue onset during
689 encoding (i.e., animal image), downsampled to 1 khz using Fieldtrip (56), and stored for further
690 analysis.

691 The LFP data was cleaned from artefacts and re-referenced as follows. For artefact rejection a
692 two-step procedure was carried out which first identified noisy channels, and then noisy trials.
693 To reject noisy channels the root mean square amplitude (RMSA) in the time window of interest
694 (-0.5 to 5 seconds around cue onset) was calculated for each channel and z-transformed (where
695 the mean and standard deviation were obtained across channels). Channels with a z-value above
696 3 were rejected. On the trial level, a similar procedure was carried out on those channels retained
697 after the first step. The RMSA was averaged in the time window of interest (-0.5 to 5 seconds)
698 and z-transformed across trials. Trials with a z-value of over 4 were rejected. Furthermore, z-
699 scores were calculated for the raw amplitude. Trials with a maximum raw amplitude z-score of
700 above 4 were also rejected. Lastly, only channels with a minimum of 25 remaining trials were
701 submitted to further analysis.

702 Finally, the data were re-referenced to yield a comparable signal across patients and to extract
703 the field potential on a very local level. To this end each microwire channel was re-referenced to
704 the mean amplitude of its neighbouring microwire channels (i.e., wires on the same bundle).
705 Bundle refers to the 8 high-impedance contacts within one Behnke-Fried hybrid electrode.
706 Instead of simply subtracting the average signal, however, we used an orthonormalization
707 procedure termed Gram-Schmidt Correction (see https://en.wikipedia.org/wiki/Gram–Schmidt_process). This procedure projects two signals into a sub-space where both signals don't
708 share any variance, i.e., they are orthonormal to each other (their sum = 0). This is an effective
709 way of subtracting those parts of a signal, which are shared between an individual channel and
710 its neighbours (such as volume conduction; see (57)). Furthermore, by only subtracting those
711 parts of the signal that are shared between the two sources this method is less prone to
712 introducing noise from the reference into the referenced channel.

715 **Spike Field Coupling:** The following procedure was used to calculate spike field coupling (SFC)
716 and to assess differences in SFC between hits and misses. As an overview, this procedure
717 calculated spike field couplings for every possible pairing of units (spikes) and LFP channel.
718 Therefore, a given pairing could either constitute coupling at the local level (i.e., spike and LFP
719 come from the same channel, or from the same bundle), or coupling at a distal level (i.e., spike
720 and LFP come from different bundles; see Figure 2 and 3). Each pair was first tested for
721 significant spike field coupling and then submitted to further analysis to compare SFC between
722 hits and misses.

723 As a first step, phase was calculated using Fieldtrip. Different parameters were used for low (2-
724 40 Hz) and high frequency ranges (40-80 Hz); i.e., using a 6-cycle wavelet for low frequencies in
725 steps of 1 Hz and a 12-cycle wavelet for high frequencies in steps of 2 Hz. We used these
726 different parameter settings for the two frequency to best capture their temporal dynamics and to
727 deal with data volume. The exact cut-off frequency of 40 Hz was chosen because of a previous
728 paper from our group where we showed that the fast gamma oscillation (between 50-80 Hz) in
729 the hippocampus is specifically related to memory encoding (23). In addition, for high
730 frequencies only the first derivative was taken before calculating phase. Phases at spike times
731 were extracted and split according to whether they occurred the time window of interest, which
732 was 1 second after the face/place stimuli were shown (2 – 3 seconds after Cue onset). If at least
733 30 spikes were available, then the data was admitted to the next step. For a given spike-LFP pair
734 a Raleigh test using the Circ_Stat Toolbox (<http://www.jstatsoft.org/v31/i10>) was calculated at
735 each frequency to assess whether phase distributions were different from a uniform distribution.
736 An FDR correction (58) was applied to correct for multiple comparisons across frequencies. If
737 this corrected p-value was below 0.05 then the spike-LFP pair was submitted to the next step. In
738 this step, pairwise phase consistency was calculated for three conditions, (i) across all trials (hits
739 and misses together), (ii) only for hits (i.e., later completely remembered trials), and (iii) only for
740 misses (i.e., partially remembered and fully forgotten trials).

741 To statistically assess whether the number of significant spike – LFP couplings identified in the
742 above procedure was above chance a randomization test was carried out. This test was run
743 separately for locally coupled and distally coupled spike – LFP pairs. To this end, trials for the
744 spike providing data and phase (i.e., LFP) providing data were shuffled. All other parameters
745 (including number of hit and miss trials) were held constant. These shuffled data were then
746 subjected to the same Raleigh test (FDR corrected) as above. For each possible spike-LFP pair
747 100 such shuffled tests were carried out and the data was stored. From these shuffled data a
748 distribution of the number of ‘significant’ spike-LFP pairs (i.e., Raleigh test $p < 0.05$; FDR
749 corrected) was generated by drawing 10000 samples, counting the number of significant spike-
750 LFP pairs for each sample.

751 To extract the peak frequency of spike field coupling a peak detection on the individual PPC
752 spectra was run using the findpeaks command in Matlab. For theta the PPC spectrum was
753 restricted to a frequency range between 3 to 13 Hz, and for gamma between 45 to 75 Hz. The
754 peak PPC had to surpass a threshold of 0.005 for both hits and misses, to ensure that meaningful
755 PPC was present in both conditions.

756 **Non-stationarities of LFP:** One may be concerned about non-stationarities of the signal and
757 whether such non-stationarities affect the phase estimations obtained with the here applied
758 Wavelet analysis. A specific concern is that the phase obtained from the Wavelet analysis is not

760 correct when the instantaneous frequency of the LFP signal does not match the frequency of the
761 Wavelet. This concern was addressed in two ways.

762 In a first step, a simulation was carried out where an oscillator in the LFP signal transitions
763 randomly between frequencies with a mean frequency of 6 Hz fluctuating between 3.5 to 9 Hz,
764 thus exhibiting strong non-stationaries across a wide range. Spikes of a hypothetical neuron were
765 simulated to be locked to the trough of this non-stationary oscillator (see Fig. S6A-B). White
766 noise was added to the simulated signal. The results of this simulation demonstrate that the mean
767 frequency of spike phase locking at 6 Hz is correctly retrieved by the Wavelet analysis (Figure
768 S6C). Crucially, the mean phase of spiking is also correctly retrieved (Figure S6D). The same
769 simulation has been carried out for the high-frequency range with similar results. From this we
770 can conclude that our Wavelet based approach is well suited to recover the mean frequency and
771 mean phase of coupling between a spiking neuron and a non-stationary oscillator.

772 In a second step, we repeated the spike-LFP coupling analysis using a combination of band-pass
773 filter and Hilbert transformation. The band-pass filter (Butterworth) was set to a width of 4 Hz
774 for the low frequency range, and 8 Hz for the high frequency range, thus leaving ample
775 opportunity for variations in instantaneous frequency. Trials were segmented as before to 14
776 seconds centred at the onset of the cue stimulus (i.e., animal), to ensure that filter artifacts at the
777 beginning and end of the trial are well out of the time window of interest (i.e., 2-3 seconds after
778 cue onset). The band-pass filter was implemented using the `ft_preprocessing` command in
779 `fieldtrip` centred at discrete steps of 1 Hz between 3 to 40 Hz (i.e., 3 = 1 to 5 Hz; 4 = 2 to 6 Hz;
780 ... 40 = 38 to 42 Hz) and 2 Hz between 40 to 80 Hz (i.e., 40 = 36 to 44 Hz; 42 = 38 to 46 Hz; ...
781 80 = 76 to 84 Hz). Phase was estimated using the Hilbert transform as implemented in `fieldtrip`
782 (`ft_preprocessing`) and phase variance was obtained using pair-wise phase consistency (PPC) as
783 described above. The results of this analysis are reported in Supplementary Figure S7.

784
785 Directionality of distal theta spike-field coupling: To assess the direction of information between
786 spikes and distally coupled LFPs the Phase Slope Index (PSI) was applied (59). The PSI is a
787 frequency resolved measure to discern the direction of information flow between two neuronal
788 regions or time series (A and B). Like many other directional coupling measures, the PSI
789 assumes a time delay for a signal to travel from A to B. If the speed of travel is constant, then the
790 phase difference between sender and recipient increases with frequency and a positive slope of
791 the phase spectrum can be expected. Hence, a positive phase slope indicates that A is the sender
792 and B is the receiver, and vice versa. We preferred the phase slope index over Granger causality
793 as it requires less assumptions and is less sensitive to noise (59). The PSI was calculated using
794 the `ft_connectivityanalysis` function in `fieldtrip` using a bandwidth of 5 Hz (i.e., phase slopes are
795 estimated over a 5 Hz window). Spike time series were convolved with a Gaussian window (25
796 ms) to yield a continuous spike density signal. The raw PSI values were baseline corrected using
797 a z-transformation to ensure an unbiased comparison between hits and misses. To this end, trials
798 for the spike providing signal were shuffled 100 times and submitted to the same PSI analysis as
799 the real data. This shuffling was carried out separately for hits and misses, thereby keeping the
800 number of overall spikes constant. The mean and standard deviation across shuffles was
801 calculated and used for z-transformation of the PSI values of the real (i.e., un-shuffled) data.
802 Finally, a minimum of 60 spikes was imposed to allow for a meaningful analysis of directional
803 information flow between the two signals (see Figure 4 – figure supplement 2 for a control
804 analysis with a minimum of 30 spikes which obtained similar results to those shown in Figure 4).

806 SFC control analysis for selection bias: In the above analysis only spike-LFP pairs, which show
807 significant phase coupling across all trials are subjected to further analysis. This could introduce
808 a potential bias, especially for cases where firing rates and trials are not evenly distributed
809 between conditions (hits vs. misses). This concern would be especially problematic if the results
810 would show an overall increase in spike-field coupling for hits vs. misses, as opposed to
811 differences in peak frequencies as shown here. Nevertheless, we accounted for this issue by
812 means of a control analysis. In this control analysis, PPC values for a given spike-LFP pair were
813 calculated for 5000 instances where the trials for spike providing and LFP providing data were
814 shuffled. As above, all other parameters (importantly number of hit and miss trials were kept
815 constant). After each shuffle a Raleigh test as above was carried out across all trials. If this test
816 retained a p-value <0.05 (FDR-corrected) PPC spectra were calculated for ‘pseudo-hits’ and
817 ‘pseudo-misses’. These spectra therefore contain the same selection bias as in the real analysis
818 because the ratio between hits and misses has been kept constant, and therefore provide a
819 baseline for hits and misses which can be used to effectively correct for this bias. Accordingly,
820 PPC values for each spike-LFP pair for the real data were z-transformed using this baseline by
821 subtracting the mean across ‘significant’ shuffle runs and dividing by the standard deviation.
822 This bias corrected data was submitted the same peak detection analysis as the real data and
823 similar results were obtained (see Figure S5).

824 Theta-Gamma Interaction: To assess the spatial overlap of local SFC in the gamma range and
825 distal SFC in the low frequency range the number of spike-LFP pairs were counted that exhibited
826 both phenomena in the same region (i.e., same microwire bundle). Cross-frequency coupling
827 (CFC) was then analysed for these overlapping pairs of locally and distally coupled spike-LFP
828 channels. To this end, both theta and gamma LFPs were taken from the same bundle of
829 microwires and therefore were recorded in the same region (or at least in very close proximity;
830 see Figure 4A-B). The PAC analysis therefore does reflect the temporal coordination of theta and
831 gamma oscillations in a local region. It is only that the locally recorded theta is phase locked to a
832 spike recorded in another, distally coupled, region. For each channel pair the peak gamma
833 frequency, and the peak theta frequency was extracted from the PPC spectra. Importantly, these
834 peaks were extracted separately for hits and misses, to account for the difference in frequency
835 between the two conditions. Peaks at gamma were restricted to a frequency range between 50 to
836 80 Hz, and 5 to 11 Hz for theta. Phase for the lower frequencies (i.e., theta) and power for the
837 higher frequencies (i.e., gamma) were calculated using the same Wavelet parameters as above
838 (i.e., 6 cycles for theta, 12 cycles for gamma). Cross-frequency coupling was then calculated via
839 the Modulation Index (35) using the function ‘ModIndex_v2.m’ provided by Adriano Tort with a
840 binning parameter of 18 bins
841 (https://github.com/cineguerrilha/Neurodynamics/blob/master/16ch/Comodulation/ModIndex_v2.m). The MI was calculated separately for hits and misses. Because the MI is affected by trial
842 numbers, a normalization procedure was applied to yield a bias free CFC measure for hits and
843 misses. To this end, trials for the phase providing channel were shuffled and MI was calculated
844 after each shuffle (N=200). This was done separately for each condition (hits and misses) to
845 generate a baseline MI under the null for each condition. The mean and standard deviation across
846 the shuffled data was then used to z-transform the MI of the real data.

847 Power Analysis: Power of LFP data was calculated using the same wavelet parameters for high
848 and low frequency ranges as above. Raw power values were z-transformed for each channel

separately using a common procedure for analysing subsequent memory effects (23, 60, 61). Power values for each channel, frequency band and trial, were first averaged across time (-0.5 to 5 seconds). Then the median and standard deviation of this time-averaged power across trials was calculated. Power values for each channel, frequency bin and trial were then z-transformed by subtracting median power and dividing by standard deviation. Trials containing outlier power values (i.e., maxima > 2.5 of standard deviation of maxima across trials) were discarded. Finally, trials were split according to conditions (hits and misses) and averaged. Power for low frequencies was calculated for channels which showed a significant SFC in the low frequency range, whereas power for high frequencies was calculated only for those channels showing significant SFC in the high frequencies.

An additional power analysis was carried out to assess the presence of a meaningful signal at the frequencies where spike-LFP coupling was observed (see Figure S8). To this end power at spike times was extracted for distally coupled LFPs in the low frequency range, and locally coupled LFPs in the gamma frequency range using the same Wavelet filter as used for SFC analysis. Power spectra were 1/f corrected by fitting and subtracting a linear function to the log-log transformed power spectra. The resulting spectra were then back transformed to linear space and centred at the peak frequency of PPC. Lastly, power values were normalized for each LFP channel by subtracting the mean across the whole spectrum and dividing by the standard deviation across the whole spectrum.

Inter-trial Phase Consistency: Inter-trial phase consistency was calculated for the lower frequency range (i.e., 2 – 40 Hz) using pairwise phase consistency (PPC)(31). Phase for each single trial was extracted using the same Wavelet transformation (6 cycles) as above. PPC spectra were limited to a frequency range of interest (2-13 Hz), comprising the slow and fast theta range. PPC spectra were calculated for hits and misses separately and only for those channels showing significant SFC in the low frequency ranges.

Spike Power Analysis: To test for the presence of theta rhythmicity within the spiking of neurons an FFT analysis was carried out on the spike density time series. Spike time series were convolved with a Gaussian window (25 ms) to yield a continuous spike density signal for the time window of interest (2-3 seconds after cue onset). These trials were then submitted to a FFT analysis using the `ft_freqanalysis` command in fieldtrip, with a Hanning taper and frequency smoothing of +/- 2 Hz. Results are shown in Figure S9.

Theta Waveshape Asymmetry: To assess the presence of asymmetric theta waveforms, which could give rise to spurious cross-frequency coupling at harmonics of theta, two control analyses were performed. For the first control analysis, MIs were calculated exactly the same way as for the real data, except that for each LFP signal the gamma frequency was taken as the 8th harmonic of the theta in that signal (i.e., for theta = 9 Hz, gamma = 9 * 8 = 72 Hz). We took the 8th harmonic as this was the frequency that was on average closest to the observed gamma frequency (i.e., 64 – 72 Hz). The 8th harmonic was estimated based on the dominant theta frequency separately for hits and misses. Next, we calculated the difference in MI between hits and misses. If asymmetric theta gives rise to the difference in CFC the real data then this effect should even be stronger in the control data where gamma was centred at the harmonic of theta. However, we observed the opposite pattern, with the real data showing stronger differences between hits and misses compared to the harmonic control data (Figure S10A).

In a second control analysis, the asymmetry index was calculated following the procedure described in (62). To this end, the LFP data for hits and misses was filtered at the theta phase providing frequency band +/- 2 Hz used for CFC analysis, using a Butterworth bandpass filter implemented in Fieldtrip. Then the filtered data was cut to the time window of interest (2-3 seconds) and peaks and troughs were identified using the ‘findpeaks’ function in Matlab. Thereafter, peaks and troughs of the filtered data were adjusted by matching them with peaks and troughs in the unfiltered data. This matching process searched for local maxima and minima in a time window of a quarter cycle length of the theta frequency (i.e., 5 Hz = 200/4 = 50 ms) centred at the peak located in the filtered data. The time stamps of these adjusted peaks and troughs were then used to calculate the asymmetry of the theta waveshape using the formula below. Where T_{asc} is the duration of the ascending flank, T_{desc} is the duration of the descending flank, and ω is the cycle length of the theta frequency. T_{asc} was calculated by subtracting the time stamp of the trough from its subsequent peak (i.e., T peak(t+1) – T trough(t)); T_{desc} was calculated by subtracting the time stamp of the peak from its subsequent trough (i.e., T trough(t+1) – T peak(t)). Therefore, both T_{asc} and T_{desc} always yield positive values. The asymmetry index (AI) is a normalized measure ranging between -1 and 1 with negative values indicating longer durations of descending flanks, and positive values indicating longer durations for ascending flanks.

$$AI = \frac{T_{asc} - T_{desc}}{\omega}$$

To verify that this index detects the presence of asymmetric waveforms a dataset recorded in the rodent entorhinal cortex was used as a positive control (courtesy of Ehren Newman). The data comprised 10 minutes of open field navigation of the rodent. Clear ongoing theta activity was present in this data and indeed a strong asymmetry could be detected (Figure S10C). For the human data, AIs were averaged across trials for hits and misses separately to yield one AI per channel. AIs between hits and misses were compared using a paired samples T-test. No difference in asymmetry between hits and misses was obtained (see Figure S10D), which further rules out an influence of asymmetric waveshapes on the observed cross-frequency coupling results.

Co-firing Analysis: Co-firings between pairs of single/multi-units (referred to as units in the below) at different time lags were calculated via cross-correlations using the xcorr function in Matlab. To this end, spike time series for each unit were concatenated across trials to yield one vector and convolved with a Gaussian envelope with a width of 25ms (~10ms full width half maximum). We chose this time window because it should represent a good balance between integrating over a long-enough time window and thus allowing for some jitter in neural firing between pairs of neurons, whilst still being temporally specific (63). To test whether this choice critically affected our results, we repeated the analysis for different window sizes, i.e. 15, 35, and 45 ms (see Figure 6 – figure supplement 4). Cross-correlations were calculated for pairs of putative ‘sending’ units, and putative ‘receiving’ units. Putative sending units were units, which showed a significant distal SFC in the low frequency range, and where the distally coupled LFP was in addition locally coupled to a unit in the high frequency (gamma) range. This locally gamma coupled unit was taken as the putative receiving unit. Accordingly, the pairs were chosen such that the region where the sending unit was coupled to is the same as the region where the

local coupling occurs. This resulted in a relatively low number of neural pairs ($N=24$), because two conditions needed to be met. More specifically, for a pair of units to be considered as such the putative sending unit needed to show significant distal low frequency coupling to the region where the putative receiving unit was located; additionally, the receiving unit needed to be significantly coupled to local gamma oscillations. This selection and labelling of units into sending and receiving units is supported by the directional coupling analysis (see Fig 4). Altogether, 5 patients contributed data to this analysis, with a median of 5 pairs per patient, and a minimum and maximum of 2 and 8 pairs per patient, respectively (see Supplementary Table S1). Cross-correlations between putative sending and putative receiving units were calculated separately for hits and misses. To correct for a potential bias of numbers of spikes, cross-correlation values for hits and misses were z-transformed according to a shuffled baseline. To this end, trials for the putative receiving unit were shuffled 2000 times and submitted to the same cross-correlation analysis as the real data. This shuffling was carried out separately for hits and misses, thereby keeping the number of overall spikes constant. The mean and standard deviation across shuffles was calculated and used for z-transformation of the cross-correlation values of the real (i.e., un-shuffled data). As a final step, only cross-correlations for pairs of neurons where the average co-incidence (mean across hits and misses) exceeded 1 at any lag were admitted to statistical analysis. This step ensured that only pairs of neurons with meaningful co-firings were used. To compare the latencies of co-firing between hits and misses a peak detection was carried out using the ‘findpeaks’ function in Matlab.

Acknowledgments

We like to thank all patients for taking time to participate in the experimental sessions. We also thank Markus Siegel for providing useful comments on previous versions of the manuscript and Pieter Roelfsema for supporting us with data collection. S.H. was supported by grants from the European Research Council (Nr. 647954), and the Economic and Social Research Council (ES/R010072/1). M.tW. and M.W. were supported by a grant from the European Research Council (StG-715714).

Figure Legends – Main Figures

Figure 1. The memory task and behavioral results. (A) During encoding patients had to memorize three associated stimuli consisting of an animal, and either a pair of face images, a pair of place images, or a pair of face-place images. The light blue bar highlights the time window that was used for the analysis of LFP and neural spiking data. (B) Memory performance during the cued recall test is shown for all patients and sessions. Note that chance level in this task for hits and misses is 16.6 and 83.3 %, respectively (indicated by dashed horizontal lines), and not 50% for both (see methods for further details). (C) Electrode locations are plotted overlaid onto a template brain in MNI space. Color codes indicate whether an electrode provided LFP, spiking, both, or no data. (D) Distribution of electrodes and recorded single- and multi-units is shown across MTL regions (Ent. Ctx.: Entorhinal Cortex; ATL.: Anterior Temporal Lobe; Amyg.: Amygdala; Phc.: Parahippocampal Cortex).

Figure 2. Spike-field coupling results for gamma. (A) Number of significant ($p_{corr}<0.05$) locally (pink) and distally (green) coupled spike-field pairs are shown. The histograms on the right show the results of a randomization procedure testing how many pairs would be expected under the null hypothesis. (B, left) Pairwise phase consistency (PPC) is plotted for local and distal spike-field pairs. Filled circles indicate significant differences ($p_{corr}<0.05$). Shaded areas indicate standard error of the mean. (B, right) PPC is shown for channels where the spike and LFP providing microwire were the same (dashed line), or where they came from different microwires (solid line). (C)

989 Pairwise phase consistency (PPC) is shown separately for hits and misses (top panel), and for the difference between
990 the two conditions (bottom panel) for locally coupled spike-field pairs. The data from all local spike-LFP pairs is
991 shown on the left, whereas on the right data where spikes and LFPs come from the same microwire were excluded.
992 Filled black circles indicate significant differences ($p_{corr} < 0.05$). Grey circles indicate statistical trends ($p_{uncorr} < 0.05$).
993 Shaded areas indicate standard error of the mean. (D) Peak frequency in PPC across all spike-field pairs is shown for
994 hits and misses (top), and for the difference (hits-misses, bottom). The data from all local spike-LFP pairs is shown
995 on the left, on the right data where spikes and LFPs come from the same microwire were excluded. The solid bar
996 indicates the mean, shaded areas indicate standard error, the box indicates standard deviation, and the bars indicate
997 5th and 95th percentiles. (E) Local gamma spike-field coupling is shown for one example multi-unit recorded from
998 the entorhinal cortex. Phase histograms on top indicate phase distribution for hits at 62 Hz (blue) and misses at 58
999 Hz (red). Spike wave shapes on the right are plotted by means of a 2D histogram.

1000
1001 **Figure 3. Spike-field coupling results for the lower frequencies.** (A) Number of significant ($p_{corr} < 0.05$) locally
1002 (pink) and distally (green) coupled spike-field pairs are shown. The histograms on the right show the results of a
1003 randomization procedure testing, with the red dashed line indicating the empirically observed value. (B) PPC is
1004 plotted for local and distal spike-field pairs. Black circles indicate significant differences ($p_{corr} < 0.05$). Grey circles
1005 indicate trends ($p_{uncorr} < 0.05$). Shaded areas indicate standard error of the mean. (C) PPC is shown separately for hits
1006 (blue) and misses (red), and for the difference between the two conditions (magenta) for distally coupled spike-field
1007 pairs. The top panels show PPC values for the theta frequency range, the bottom panel shows all frequencies up to
1008 40 Hz. Shaded areas indicate standard error of the mean. Black circles indicate significant differences ($p_{corr} < 0.05$).
1009 (D) Peak frequency in PPC across all distal spike-field pairs is shown for hits and misses (top), and for the
1010 difference (hits-misses). Box plots indicate the same indices as in Fig 2D. (E) Distal theta spike-field coupling is
1011 shown for one example single-unit recorded from the left posterior hippocampus, and the LFP recorded from the left
1012 entorhinal cortex. Phase histograms on top indicate phase distribution for hits at 9 Hz (blue) and misses at 5 Hz
1013 (red). Spike wave shapes on the right are plotted by means of a 2D histogram.

1014
1015 **Figure 4. Directional coupling analysis of distal spike-LFP coupling using Phase Slope Index (PSI).**

1016 A) A schematic of the analysis is shown. Spike time series were convolved with a Gaussian window, and the PSI
1017 was calculated between the spike time series (green) and the distally coupled LFP (pink). B) The left plot shows
1018 normalized PSI (i.e., z-values) for hits (blue) and misses (red). Hits show significantly positive PSIs throughout the
1019 theta frequency range, peaking at ~ 8 Hz (blue circles; $p_{corr} < 0.05$). The right plot shows the difference in PSI
1020 between hits and misses. Hits show significantly higher PSIs compared to misses, especially in the high theta range
1021 (black circles; $p_{corr} < 0.05$).

1022
1023 **Figure 5. Theta to gamma cross frequency coupling results.** (A) Percentage of overlapping local gamma (pink)
1024 and distal theta (green) spike-field pairs are shown. (B) Spikes and band-pass filtered LFP data for one example
1025 single trial are shown. The top row shows spikes from a multi-unit in the left parahippocampal cortex which are
1026 coupled to the LFP in the right middle hippocampus (green). The gamma LFP from the same region (right mid
1027 hippocampus) is shown below (pink) as well as spikes from a multi-unit in the same region that is coupled to this
1028 gamma oscillation. Note the gamma power increase around theta troughs. (C) Theta phase sorted gamma power (y-
1029 axis centered to gamma peak frequency) is shown for all trials for the data shown in (B). The bottom panel shows
1030 averaged normalized band-pass filtered LFP data (black) and unfiltered LFP data (grey). (D) Co-modulograms are
1031 shown for hits and misses. Modulations indices(35), which indicate the strength of cross-frequency coupling, are
1032 plotted in terms of z-values where means and standard deviations were obtained from a trial shuffling procedure.
1033 The difference between hits and misses is shown as z-values obtained from a non-parametric Wilcoxon signrank test
1034 masked with $p_{corr} < 0.05$ (FDR-corrected). The panel in the bottom right shows the individual differences between hits
1035 and misses across the whole dataset (N=83 pairs).

1036
1037 **Figure 6. Co-firing analysis results for theta-gamma coupled assemblies.** (A) A schematic of the co-firing
1038 analysis is shown. Pairs of putative up-stream (green) and putative down-stream (pink) units were selected for the
1039 co-firing analysis. Co-firing was measured by cross-correlating spike time series (convolved with a Gaussian
1040 envelope). Cross-correlations indicate the latency of firing of a putative down-stream neuron (pink) in response to a
1041 putative up-stream neuron (green). (B) Spike cross-correlations for hits and misses are plotted in terms of z-values
1042 derived from a trial shuffling procedure. Hits (blue) show increased co-firing between putative up-stream and

1044 putative down-stream neurons at around 20-40 ms ($p_{corr} < 0.05$), whereas misses (red) peak at 60 ms ($p_{corr} < 0.05$).
1045 Shaded areas indicate standard error of the mean. Differences between co-firing of hits and misses is plotted on the
1046 right. Hits show higher co-firing at 20 ms compared to misses ($p_{corr} < 0.05$). (C) Co-firing data is shown for one
1047 example pair of units. (D) Results of the co-firing peak detection analysis. The distribution of the peak lag is shown
1048 for hits (blue) and misses (red), and for the difference for each pair of neurons (pink). Hits exhibit significantly
1049 shorter lags of co-firing compared to misses ($p < 0.005$).
1050

1051 **Figure Legends – Figure supplements**

1052

1053 **Figure 1 – figure supplement 1. Automatic classification of Single- and Multi-Units according to Tankus et al.**
1054 (26). A) A scatter plot shows the distribution of the two criteria according to which neurons were classified into
1055 single-units and multi-units. Criterion 1 (y-axis) is the percentage of ISIs < 3ms. Criterion 2 (x-axis) is the
1056 variability of the spike waveshape in the rise time window. If a given unit shows less than 1% of ISIs < 3ms, and
1057 low variability of waveshapes (<3) then is labelled a single-unit (red dots), otherwise it is labelled a multi-unit (blue
1058 dots). B) The variability of the spike waveshape in the rise time window is shown for one example single-unit. The
1059 green shaded area highlights the rise time window which starts at the maximum curvature pre-peak, and ends at the
1060 peak. Waveshape variability is computed dividing the summed standard deviation in the rise time window by the
1061 rise height (i.e. peak-to-trough difference). C) Waveshapes and ISIs are plotted for 4 example SUAs (top row) and 4
1062 example MUAs (bottom row).

1063 **Figure 1 – figure supplement 2. Firing rate effects during memory encoding.** (A) Averaged normalized
1064 population spike densities are plotted for hits and misses. Hits show a sustained increase in firing after 3 seconds
1065 compared to misses. Shaded areas indicate standard error of the mean. (B) The difference between hits and misses is
1066 shown for the three time windows of interest. A significant increase for hits > misses was only observed for the
1067 response time period. (C) and (D) Two example single units are shown. Wave shapes on the top right are plotted by
1068 means of 2D histograms (see (64)). The plots beneath the raster plots show the normalized spike densities for hits
1069 (blue) and misses (red).
1070

1071 **Figure 1 – figure supplement 3. Stimulus evoked LFP activity is shown by means of inter-trial phase**
1072 **coherence (ITPC) and event related potentials (ERPs).** (A) ITPC is plotted by means of phase locking value
1073 (PLV). The data shows a robust evoked response at the onset of the cue stimulus (0 sec.) and the onset of the
1074 association stimulus (2 sec.) albeit the latter appears to be slightly weaker. (B) The ERP is shown averaged across all
1075 trials, electrodes and sessions. (C) The ERP is shown for hits (blue) and misses (red). Note that no differences
1076 between ERP components between hits and misses is observed.
1077

1078 **Figure 1 – figure supplement 4. LFP power and intertrial phase coherence (ITPC) results are shown.**
1079 (A) Power for high (top) and low frequencies are plotted for hits, misses and the difference. Time axis indicates time
1080 from cue onset. The dashed lines indicate the time window of association period. (B) Power during the association
1081 period is shown for hits (blue) and misses (red) and the difference (pink). Low frequencies show decreased power
1082 for later remembered associations, whereas high frequencies show increased power for later remembered
1083 associations which is a typically observed pattern (27). Concerning the higher frequency range, hits show increased
1084 power in a slow (45 – 50 Hz) and a fast gamma band (65 – 80 Hz) compared to misses. Filled black circles indicate
1085 $p < 0.05$, FDR-corrected. (C) ITPC results are shown by means of pairwise phase consistency (PPC) for hits, misses
1086 and the difference. Increased phase concentration across trials is observed for the low theta frequency band at the
1087 onset of the cue stimulus, as would be expected, and somewhat weaker at the onset of the association stimulus (cf.
1088 Fig. S2). (D) PPC results are shown for the association time window (2-3 sec.) for hits, misses and the difference.
1089 No significant difference between hits and misses was observed, albeit hits showed a trend for increased phase
1090 coherence at 4 Hz compared to misses ($p < 0.05$; uncorrected; grey filled circle).
1091

1092 **Figure 2 – figure supplement 1. Selection bias control analysis**

1093 Results of a control analysis are shown to rule out a possible bias on the Spike-Field Coupling results due to
1094 unbalanced trial numbers. The control analysis replicated the original results showing faster gamma frequencies for
1095 hits compared to misses (compare Figure 2 in main text).
1096

1097
1098 **Figure 2 – figure supplement 2. Simulation of the effects of a non-stationary oscillator on Wavelet analysis.** A)
1099 A signal is simulated that randomly transitions between slower and faster frequencies with a mean frequency of 6
1100 Hz (range: 3.5 – 9 Hz). White noise is added to the signal. Spikes are shown on the bottom (red ticks). Spikes are
1101 locked to the trough. An epoch of 42 seconds has been simulated but here only 5 seconds are shown. B)
1102 Instantaneous frequency is plotted (derived from the simulated signal before adding noise using ‘instfreq’ in
1103 Matlab). Note the strong non-stationarities in frequency. C) PPC spectrum shows a clear peak at the true mean
1104 frequency of 6 Hz. D) The phase histogram shows the phase derived from Wavelet analysis at 6 Hz. Mean angle of
1105 the spike phase is shown in blue, the ground truth phase angle is shown in red.
1106

1107 **Figure 2 – figure supplement 3. Spike-LFP coupling results obtained with bandpass filtering and Hilbert
1108 transformation.**

1109 A) Spike-LFP coupling for the high frequency range for local (pink) and distal (green) pairs is shown. Local spike-
1110 LFP pairs show higher phase coupling compared to distal pairs in the high gamma range (black dots; $p_{corr} < 0.05$). B)
1111 Top: Spike-LFP coupling is shown for the gamma frequency range for local pairs only for hits (blue) and misses
1112 (red). Bottom: The difference between hits and misses is shown. Black dots indicate $p_{corr} < 0.05$ (FDR corrected). C)
1113 Gamma peak frequency in PPC across all local spike-field pairs is shown for hits and misses (top), and for the
1114 difference (hits-misses). Box plots indicate the same indices as in Fig 3D in the main manuscript. Hits trend towards
1115 faster gamma frequencies compared to misses ($t_{32}=1.56$; $p=0.06$).
1116

1117 **Figure 2 – figure supplement 4. Power for phase providing gamma frequencies.**

1118 The 1/f corrected power spectra are shown for hits (blue) and misses (red) centred on the peak gamma frequency of
1119 spike-LFP coupling. To demonstrate the existence of a meaningful signal in the phase providing frequency range
1120 (i.e. peak in the power spectrum) a paired samples t-test was calculated, where the power in the peak (a) was
1121 contrasted with the power at the edges (b1 and b2). Power values were averaged for hits and misses. For the gamma
1122 range, power at the peak was significantly higher compared to the power at the edges ($t_{52}=2.38$; $p<0.05$).
1123

1124 **Figure 2 – figure supplement 5. Relationship between gamma SFC and Power.** Left: Power is shown for hits,
1125 misses and the difference between hits and misses for channels whose LFP was locally coupled to neural firing in
1126 gamma. No significant differences between hits and misses were observed. Middle: Differences in gamma peak
1127 power between hits and misses are shown. No significant differences in gamma peak frequency between hits and
1128 misses were observed ($p>0.15$). Right: A scatter plot with the hits-miss differences in gamma peak frequency in
1129 local spike-LFP coupling (x-axis), and gamma peak frequency in power is shown. The correlation was very close to
1130 zero. These results show that the memory-related effects in gamma spike-LFP coupling were not driven by similar
1131 effects in power.
1132

1133 **Figure 2 – figure supplement 6. Further control analyses for possible spike-interpolation artefacts.** (A)
1134 Differences between hits and misses in PPC are shown for channel pairs where spikes were recorded on different
1135 microwires than the LFP (but located on the same bundle of the B.F. electrode) and where no SUA/MUA activity
1136 was detected on the LFP channel (i.e. ‘silent’ microwire). Black dots indicate $p < 0.05$ uncorrected, asterisks indicate
1137 $p < 0.05$ (T-test; one-tailed).
1138

1139 **Figure 2 – figure supplement 7. Local gamma Spike – LFP coupling results split by anatomical regions.** Most
1140 local gamma SFCs (~2/3) were found in the Hippocampus (Hipp) followed by the Amygdala (Amyg) and
1141 Entorhinal Cortex (Ent Ctx.). The general pattern of SFC at slightly faster gamma frequencies for hits compared to
1142 misses was found in all three regions. A non-parametric ANOVA (Kruskal-Wallis test) with the difference in
1143 gamma peak frequency between hits and misses as dependent variable and anatomical region as independent
1144 variable revealed no significant effect ($F_{2,35}=0.61$; $p>0.5$). Black dots indicate $p < 0.05$ uncorrected. Shaded areas
1145 indicate SEM.
1146

1147 **Figure 3 – figure supplement 1. Selection bias control analysis for distal theta SFC**

1148 Results of a control analysis are shown to rule out a possible bias on the Spike-Field Coupling results due to
1149 unbalanced trial numbers. The control analysis replicated the original results showing faster gamma frequencies for
1150 hits compared to misses (compare Figure 3 in main text).
1151

1152 **Figure 3 – figure supplement 2. Spike-LFP coupling results obtained with bandpass filtering and Hilbert
1153 transformation.**

1153
1154 A) Spike-LFP coupling for the low frequency range for local (pink) and distal (green) pairs is shown. Distal spike-
1155 LFP pairs show a tendency for higher phase coupling compared to local pairs in the high theta range (grey dots; p_{uncorr}<0.05). B) Top: Spike-LFP coupling is shown for the theta frequency range for distal pairs only for hits (blue) and misses (red). Bottom: The difference between hits and misses is shown. Black dots indicate p_{corr}<0.05 (FDR corrected). C) Theta peak frequency in PPC across all distal spike-field pairs is shown for hits and misses (top), and for the difference (hits-misses). Box plots indicate the same indices as in Fig 3D in the main manuscript. Hits demonstrate significantly faster theta frequencies compared to misses ($t_{175}=2.73$; p<0.005).

1160
1161 **Figure 3 – figure supplement 3. Power for phase providing theta frequencies.**

1162 The 1/f corrected power spectra are shown for hits (blue) and misses (red) centred on the peak theta frequency of
1163 spike-LFP coupling. To demonstrate the existence of a meaningful signal in the phase providing frequency range
1164 (i.e. peak in the power spectrum) a paired samples t-test was calculated, where the power in the peak (a) was
1165 contrasted with the power at the edges (b1 and b2). Theta power at the peak was significantly higher compared to
1166 the power at the edges ($t_{374}=2.44$; p<0.01).

1167
1168 **Figure 3 – figure supplement 4. Spike Power Analysis.**

1169 An FFT analysis is shown for continuous spike density time series to test whether spikes themselves showed clear
1170 peaks in the theta frequency range. No peaks were obtained neither for hits (blue) nor for misses (red), and no
1171 significant differences between hits and misses were observed ($p_{corr}>0.05$).
1172

1173 **Figure 3 – figure supplement 5. Relationship between distal theta SFC and Power.** Left: Power is shown for
1174 hits, misses and the difference between hits and misses for channels whose LFP was distally coupled to neural firing
1175 in theta. An unspecific decrease in power for hits compared to misses across the lower frequency range was
1176 observed (black dots indicate p<0.05, FDR corrected). Middle: Differences in theta peak power between hits and
1177 misses are shown. No significant difference in theta peak frequency between hits and misses was observed (p>0.9).
1178 Right: A scatter plot with the hits-miss differences in theta peak frequency in spike-LFP coupling (x-axis), and theta
1179 peak frequency in power is shown. The correlation was very close to zero. These results show that the memory-
1180 related effects in distal theta spike-LFP coupling were not driven by similar effects in power.

1181 **Figure 3 – figure supplement 6. Control analyses for possible spike-interpolation artefacts.** Distal theta spike-
1182 LFP coupling results are shown filtered for LFP channels which did not show any SUA/MUA activity (i.e. ‘silent’
1183 microwires). This analysis replicated the results shown in the main manuscript which suggests that spike
1184 interpolation had no bearing on the memory-related spike-LFP coupling effects. Black dots indicate p<0.05, FDR
1185 corrected. *** indicates p<0.001.
1186

1187 **Figure 3 – figure supplement 7. Distal theta Spike – LFP coupling results split by anatomical regions.** Distal theta SFC
1188 results were summarized to reflect coupling within the hippocampus (Hipp. -> Hipp.), between the
1189 Hippocampus and surrounding MTL areas (i.e. MTL+: Amygdala, Entorhinal Cortex, Parahippocampal Cortex, and
1190 anterior Temporal Lobe) and within the MTL+. This was done to yield reasonable datapoints for anatomical
1191 comparisons. The general pattern of faster distal theta SFC for hits compared to misses was replicated in all
1192 anatomical regions. A non-parametric ANOVA (Kruskal-Wallis test) with the difference in theta peak frequency
1193 between hits and misses as dependent variable and anatomical region as independent variable revealed no significant
1194 effect ($F_{3,204}=0.804$; p>0.4). Black dots indicate p<0.05, FDR corrected. Shaded areas indicate SEM.
1195

1196 **Figure 4 – figure supplement 1. Phase slope index (PSI) results split by anatomical regions.** Directional
1197 coupling results between Hippocampus and adjacent MTL areas (i.e. MTL+: Amygdala, Entorhinal Cortex,
1198 Parahippocampal Cortex, and anterior Temporal Lobe) is shown. Asterisks indicate significant difference from 0 (t-
1199 test; p<0.05; one-tailed). The results replicate the general pattern of the spike being the sender and the LFP being the
1200 receiver for hits (left) which reaches significance for within hippocampal Spike-LFP pairs and within MTL+ Spike-
1201 LFP pairs (left panel). Both regions also show a significantly higher Spike □ LFP direction for hits compared to
1202 misses. A non-parametric ANOVA (Kruskal-Wallis test) with the difference in PSI (hits- misses) as dependent
1203 variable and anatomical region as independent variable revealed a significant effect ($F_{3,302}=4.518$; p<0.005),
1204 indicating that the memory dependent effect in PSI was mostly driven by within regional coupling with the
1205 Hippocampus and MTL+.

1206
1207 **Figure 4 – figure supplement 2. Phase slope index (PSI) results using a minimum of 30 spikes.**
1208

1209
1210 **Figure 5 – figure supplement 1. Harmonic and asymmetric waveshape control analysis** A) The results of a
1211 harmonic control analysis are shown where the gamma power providing frequency was taken as the 8th harmonic of
1212 the theta phase providing frequency. The panel on the left shows the modulation index (MI) of the real data, the
1213 middle panel plots the MI from the harmonic control, and the panel on the right shows the difference. The white
1214 square highlights the window that was used for statistical analysis shown in (B). CFC for the real data is stronger
1215 than in the harmonic control data, ruling out an influence of asymmetric theta waveshapes. (C) Theta waveshape
1216 was quantified by the asymmetry index (see (13)) and is shown for a rodent LFP dataset recorded in the entorhinal
1217 cortex during an open field navigation task (courtesy of Ehren Newman). A strong asymmetry is present with the
1218 ascending flank covering less time than the descending flank. (D) The results of same analysis are shown for the
1219 theta providing channels in humans for hits (blue) and misses (red). Waveshapes appear much more symmetric
1220 compared to rodents (note the difference in scale on the x-axis between C and D), albeit both exhibit a slight
1221 asymmetry in the same direction as observed in rodents (ascending < descending flank). Importantly, no difference
1222 between hits and misses was observed in waveshape asymmetry, thus further ruling out an influence of asymmetric
1223 theta waveshape on the observed cross-frequency coupling results.
1224

1225 **Figure 5 – figure supplement 2. Cross-frequency coupling results split by anatomical regions.** Cross-frequency
1226 coupling results are shown for the Hippocampus (Hipp.), the Entorhinal Cortex (Ent. Ctx.) and the Amygdala
1227 (Amyg.). The results for the Entorhinal Cortex and Amygdala were combined due to low number of available data
1228 points. Cross-frequency coupling is shown by means of the z-transformed modulation index (MI; see Methods). The
1229 results show that hits demonstrated above chance cross-frequency coupling in the Hippocampus only (left subpanel,
1230 Wilcoxon Tests, $p<0.01$), which also demonstrated significantly higher MI for hits compared to misses (right
1231 subpanel, Wilcoxon Tests, $p<0.001$). A non-parametric ANOVA (Kruskal-Wallis test) with the difference in MI
1232 (hits- misses) as dependent variable and anatomical region as independent variable revealed a significant effect
1233 ($F_{1,302}=4.58$; $p<0.05$), indicating that the memory dependent effect in cross-frequency coupling was mostly driven
1234 by the Hippocampus. However, caution should be taken in interpreting this result due to the uneven number of
1235 samples between the two regions, and the uneven distribution of electrodes across patients.
1236

1237 **Figure 5 – figure supplement 3. Cross-frequency coupling results using only ‘silent’ microwire channels for**
1238 **gamma power estimation.** Hits show significantly stronger MI compared to misses (Wilcoxon test; $z=4.47$;
1239 $p=3.96 \cdot 10^{-6}$).
1240

1241 **Figure 6 – figure supplement 1. Co-firing analysis using all possible pairs of SUAs/MUAs.** Cross-correlations
1242 between all possible pairs of units are shown for hits and misses for (A) negative lags and (B) positive lags. No
1243 differences in co-firing lags between hits and misses were obtained. However, higher simultaneous or near-
1244 simultaneous co-firing was observed for hits compared to misses (B). Black dots indicate $p<0.05$, FDR corrected.
1245

1246 **Figure 6 – figure supplement 2. Co-firing analysis at negative lags.**

1247 A) The results for the co-firing analysis at negative lags (putative down-stream neuron fires before putative up-
1248 stream neuron) are shown. Hits show significant above chance co-firings at lags -70 to -50, and -30 to -10 ms
1249 ($p_{corr}<0.05$), whereas misses show strongest co-firing only at lag -10 ms ($p_{uncorr}<0.05$). The co-firing difference
1250 between hits and misses is shown on the right, showing strongest differences at lags -60 to -40 ms ($p_{uncorr}<0.05$). B)
1251 Results of the co-firing peak detection analysis are plotted. Compared to hits, misses exhibit peak co-firings at
1252 shorter negative latencies (i.e. closer to 0; $t_{14}=-2.82$; $p<0.05$). C) A schematic of the STDP function is shown.
1253 Notably, the results shown in A and B, suggest that hits showed a tendency for putative down-stream neurons (pink)
1254 to fire *long* before putative up-stream neurons (green), whereas misses showed a tendency towards co-firing at a
1255 much *shorter* lag (-10 ms). This latter pattern would lead to a strong punishment of the synaptic connections (LTD),
1256 and hence weaker memories. Therefore, these results, albeit statistically weaker than the results for positive lags
1257 reported in the main manuscript (Figure 5), are fully consistent with STDP.
1258

1259 **Figure 6 – figure supplement 3. Co-firing analysis split by anatomical regions.** Cross correlations are shown
1260 between pairs of SUAs/MUAs where the upstream and the downstream units are both within the Hippocampus

(Hip→Hip), where the upstream unit is in the Hippocampus and the downstream unit in the MTL+ (i.e. Parahippocampal cortex, Entorhinal Cortex, or Amygdala; MTL+→Hip), or where the upstream unit is in the MTL+ and the downstream unit is in the Hippocampus (Hip→MTL+). A trend for earlier co-firing can be observed for all three subregions, with Hippocampal co-firing reaching significance (* p<0.05) and the Hip→MTL+ and MTL+→Hip trending towards significance (+ p<0.1). A non-parametric ANOVA (Kruskal-Wallis test) with the difference in peak co-firing (hits- misses) as dependent variable and anatomical region as independent variable revealed no significant effect ($F_{2,20} = 0.44$; p>0.6).

Figure 6 – figure supplement 4. Co-firing analysis for different lengths of gaussian windows (i.e. smoothing). The cross-correlation analysis of spike trains between putative up-stream and putative down-stream neurons is reported with different smoothing parameters, i.e. different lengths of the gaussian window that was used to convolve the spike trains before calculating the cross-correlations. The basic pattern of co-firing at earlier lags for hits compared to misses was replicated across all window lengths, except for the shortest one (15 ms) where the results trended towards significance (p=0.053). Black dots indicate p<0.05 FDR corrected, grey dots indicate p<0.05 uncorrected, * indicate p<0.05, and + indicate p<0.1 (T-tests).

References

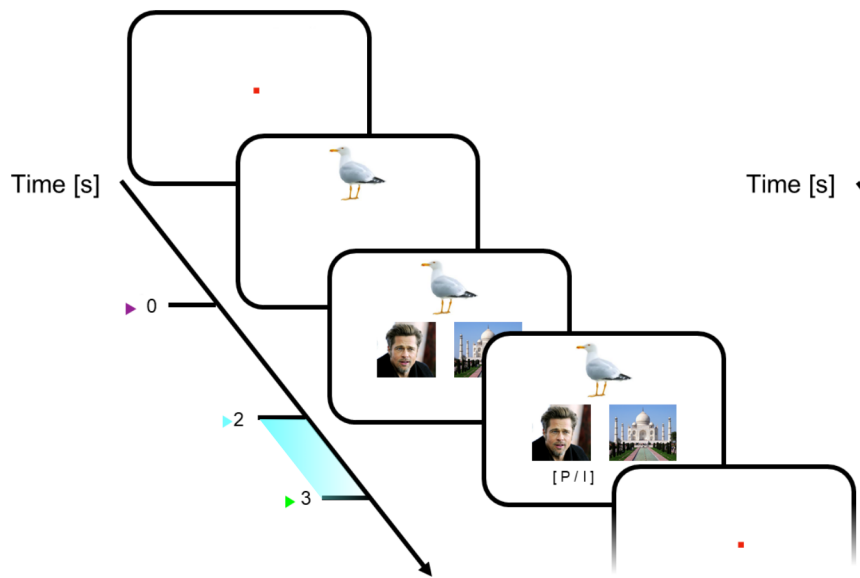
1. J. Fell, N. Axmacher, The role of phase synchronization in memory processes. *Nat Rev Neurosci* **12**, 105-118 (2011).
2. J. Fell *et al.*, Human memory formation is accompanied by rhinal-hippocampal coupling and decoupling. *Nat Neurosci* **4**, 1259-1264 (2001).
3. E. A. Solomon *et al.*, Dynamic Theta Networks in the Human Medial Temporal Lobe Support Episodic Memory. *Curr Biol* **29**, 1100-1111 e1104 (2019).
4. E. R. Kandel, The molecular biology of memory storage: a dialogue between genes and synapses. *Science* **294**, 1030-1038 (2001).
5. H. Markram, J. Lubke, M. Frotscher, B. Sakmann, Regulation of synaptic efficacy by coincidence of postsynaptic APs and EPSPs. *Science* **275**, 213-215 (1997).
6. G. Bi, M. Poo, Synaptic modification by correlated activity: Hebb's postulate revisited. *Annu Rev Neurosci* **24**, 139-166 (2001).
7. D. O. Hebb, *The organization of behavior; a neuropsychological theory*, A Wiley book in clinical psychology (Wiley, New York,, 1949), pp. xix, 335 p.
8. V. Wespatat, F. Tennigkeit, W. Singer, Phase sensitivity of synaptic modifications in oscillating cells of rat visual cortex. *J Neurosci* **24**, 9067-9075 (2004).
9. G. Buzsaki, Neural syntax: cell assemblies, synapsembles, and readers. *Neuron* **68**, 362-385 (2010).
10. P. Fries, Rhythms for Cognition: Communication through Coherence. *Neuron* **88**, 220-235 (2015).
11. W. Singer, Neuronal synchrony: a versatile code for the definition of relations? *Neuron* **24**, 49-65, 111-125 (1999).
12. M. J. Jutras, E. A. Buffalo, Synchronous neural activity and memory formation. *Curr Opin Neurobiol* **20**, 150-155 (2010).
13. P. T. Huerta, J. E. Lisman, Bidirectional synaptic plasticity induced by a single burst during cholinergic theta oscillation in CA1 in vitro. *Neuron* **15**, 1053-1063 (1995).
14. J. M. Hyman, B. P. Wyble, V. Goyal, C. A. Rossi, M. E. Hasselmo, Stimulation in hippocampal region CA1 in behaving rats yields long-term potentiation when delivered to the peak of theta and long-term depression when delivered to the trough. *J Neurosci* **23**, 11725-11731 (2003).
15. S. Hanslmayr, B. P. Staresina, H. Bowman, Oscillations and Episodic Memory: Addressing the Synchronization/Desynchronization Conundrum. *Trends Neurosci* **39**, 16-25 (2016).
16. U. Rutishauser, I. B. Ross, A. N. Mamelak, E. M. Schuman, Human memory strength is predicted by theta-frequency phase-locking of single neurons. *Nature* **464**, 903-907 (2010).
17. M. J. Jutras, P. Fries, E. A. Buffalo, Gamma-band synchronization in the macaque hippocampus and memory formation. *J Neurosci* **29**, 12521-12531 (2009).
18. B. J. Griffiths, M. C. Martin-Buro, B. P. Staresina, S. Hanslmayr, Disentangling neocortical alpha/beta and hippocampal theta/gamma oscillations in human episodic memory formation. *Neuroimage* **242**, 118454 (2021).

- 1315 19. B. Lega, J. Burke, J. Jacobs, M. J. Kahana, Slow-Theta-to-Gamma Phase-Amplitude Coupling in Human
1316 Hippocampus Supports the Formation of New Episodic Memories. *Cereb Cortex* **26**, 268-278 (2016).
- 1317 20. M. Voroslakos *et al.*, Direct effects of transcranial electric stimulation on brain circuits in rats and humans.
Nat Commun **9**, 483 (2018).
- 1319 21. C. D. Geisler, J. M. Goldberg, A stochastic model of the repetitive activity of neurons. *Biophys J* **6**, 53-69
1320 (1966).
- 1321 22. L. L. Colgin *et al.*, Frequency of gamma oscillations routes flow of information in the hippocampus. *Nature*
1322 **462**, 353-357 (2009).
- 1323 23. B. Griffiths *et al.*, Directional coupling of slow and fast hippocampal gamma with neocortical alpha/beta
1324 oscillations in human episodic memory. *Proc Natl Acad Sci U S A* **in press** (2019).
- 1325 24. C. W. Dickey *et al.*, Travelling spindles create necessary conditions for spike-timing-dependent plasticity
1326 in humans. *Nat Commun* **12**, 1027 (2021).
- 1327 25. B. H. Joensen, M. G. Gaskell, A. J. Horner, United we fall: All-or-none forgetting of complex episodic
1328 events. *J Exp Psychol Gen* **149**, 230-248 (2020).
- 1329 26. A. Tankus, Y. Yeshurun, I. Fried, An automatic measure for classifying clusters of suspected spikes into
1330 single cells versus multiunits. *J Neural Eng* **6**, 056001 (2009).
- 1331 27. J. F. Burke, A. G. Ramayya, M. J. Kahana, Human intracranial high-frequency activity during memory
1332 processing: neural oscillations or stochastic volatility? *Curr Opin Neurobiol* **31**, 104-110 (2015).
- 1333 28. G. Buzsaki, E. W. Schomburg, What does gamma coherence tell us about inter-regional neural
1334 communication? *Nat Neurosci* **18**, 484-489 (2015).
- 1335 29. S. Liebe, G. M. Hoerzer, N. K. Logothetis, G. Rainer, Theta coupling between V4 and prefrontal cortex
1336 predicts visual short-term memory performance. *Nat Neurosci* **15**, 456-462, S451-452 (2012).
- 1337 30. S. N. Jacob, D. Hahnke, A. Nieder, Structuring of Abstract Working Memory Content by Fronto-parietal
1338 Synchrony in Primate Cortex. *Neuron* **99**, 588-597 e585 (2018).
- 1339 31. M. Vinck, M. van Wingerden, T. Womelsdorf, P. Fries, C. M. Pennartz, The pairwise phase consistency: a
1340 bias-free measure of rhythmic neuronal synchronization. *Neuroimage* **51**, 112-122 (2010).
- 1341 32. J. Jacobs, M. J. Kahana, A. D. Ekstrom, I. Fried, Brain oscillations control timing of single-neuron activity
1342 in humans. *J Neurosci* **27**, 3839-3844 (2007).
- 1343 33. D. Bush, N. Burgess, Advantages and detection of phase coding in the absence of rhythmicity.
Hippocampus **30**, 745-762 (2020).
- 1344 34. T. Eliav *et al.*, Nonoscillatory Phase Coding and Synchronization in the Bat Hippocampal Formation. *Cell*
1345 **175**, 1119-1130 e1115 (2018).
- 1346 35. A. B. Tort, R. Komorowski, H. Eichenbaum, N. Kopell, Measuring phase-amplitude coupling between
1347 neuronal oscillations of different frequencies. *J Neurophysiol* **104**, 1195-1210 (2010).
- 1348 36. J. Aru *et al.*, Untangling cross-frequency coupling in neuroscience. *Curr Opin Neurobiol* **31**, 51-61 (2015).
- 1349 37. B. C. Lega, J. Jacobs, M. Kahana, Human hippocampal theta oscillations and the formation of episodic
1350 memories. *Hippocampus* **22**, 748-761 (2012).
- 1351 38. A. Goyal *et al.*, Functionally distinct high and low theta oscillations in the human hippocampus. *Nat
1353 Commun* **11**, 2469 (2020).
- 1354 39. J. Jacobs, Hippocampal theta oscillations are slower in humans than in rodents: implications for models of
1355 spatial navigation and memory. *Philos Trans R Soc Lond B Biol Sci* **369**, 20130304 (2014).
- 1356 40. U. Slawinska, S. Kasicki, The frequency of rat's hippocampal theta rhythm is related to the speed of
1357 locomotion. *Brain Res* **796**, 327-331 (1998).
- 1358 41. G. R. Richard *et al.*, Speed modulation of hippocampal theta frequency correlates with spatial memory
1359 performance. *Hippocampus* **23**, 1269-1279 (2013).
- 1360 42. G. Buzsaki, D. Tingley, Space and Time: The Hippocampus as a Sequence Generator. *Trends Cogn Sci* **22**,
1361 853-869 (2018).
- 1362 43. J. Lefebvre, A. Hutt, J. F. Knebel, K. Whittingstall, M. M. Murray, Stimulus statistics shape oscillations in
1363 nonlinear recurrent neural networks. *J Neurosci* **35**, 2895-2903 (2015).
- 1364 44. J. E. Lisman, O. Jensen, The theta-gamma neural code. *Neuron* **77**, 1002-1016 (2013).
- 1365 45. F. Roux, P. J. Uhlhaas, Working memory and neural oscillations: alpha-gamma versus theta-gamma codes
1366 for distinct WM information? *Trends Cogn Sci* **18**, 16-25 (2014).
- 1367 46. A. von Stein, J. Sarnthein, Different frequencies for different scales of cortical integration: from local
1368 gamma to long range alpha/theta synchronization. *Int J Psychophysiol* **38**, 301-313 (2000).
- 1369 47. M. Schneider *et al.*, A mechanism for inter-areal coherence through communication based on connectivity
1370 and oscillatory power. *Neuron* **109**, 4050-4067 e4012 (2021).

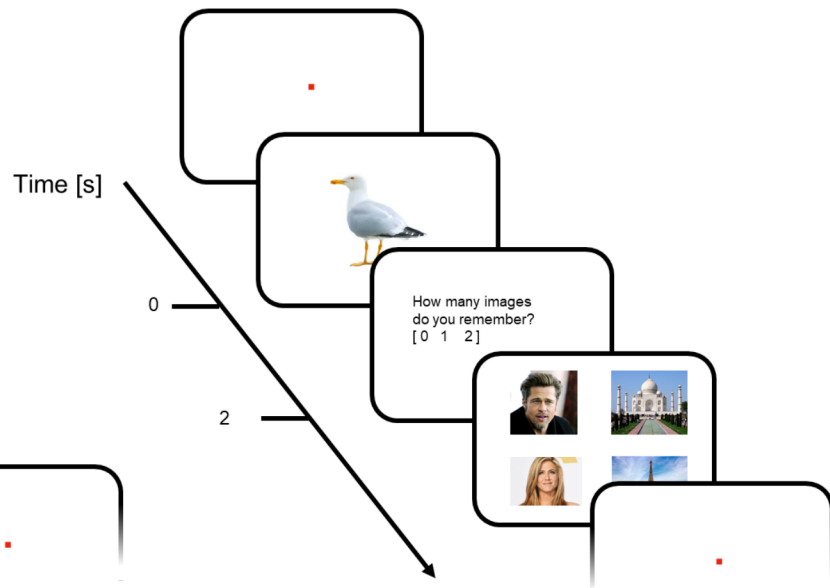
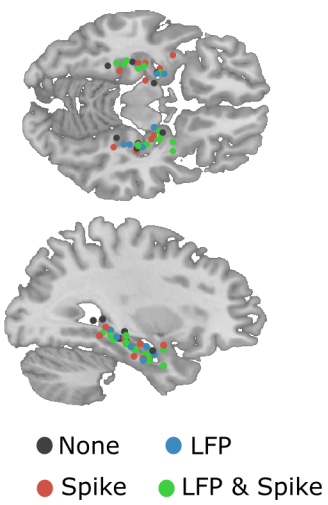
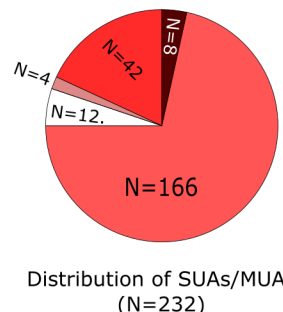
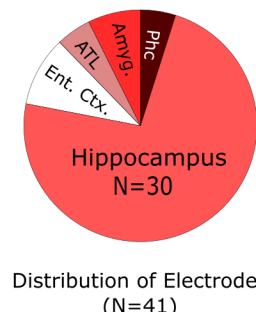
- 1371 48. A. Maass *et al.*, Laminar activity in the hippocampus and entorhinal cortex related to novelty and episodic
1372 encoding. *Nat Commun* **5**, 5547 (2014).
- 1373 49. R. Koster *et al.*, Big-Loop Recurrence within the Hippocampal System Supports Integration of Information
1374 across Episodes. *Neuron* **99**, 1342-1354 e1346 (2018).
- 1375 50. J. Zheng *et al.*, Neurons detect cognitive boundaries to structure episodic memories in humans. *Nat
1376 Neurosci* **25**, 358-368 (2022).
- 1377 51. P. Fries, J. H. Reynolds, A. E. Rorie, R. Desimone, Modulation of oscillatory neuronal synchronization by
1378 selective visual attention. *Science* **291**, 1560-1563 (2001).
- 1379 52. M. Moscovitch, The hippocampus as a "stupid," domain-specific module: Implications for theories of
1380 recent and remote memory, and of imagination. *Can J Exp Psychol* **62**, 62-79 (2008).
- 1381 53. D. H. Brainard, The psychophysics toolbox. *Spatial vision* **10**, 433-436 (1997).
- 1382 54. R. Q. Quiroga, Z. Nadasdy, Y. Ben-Shaul, Unsupervised spike detection and sorting with wavelets and
1383 superparamagnetic clustering. *Neural Comput* **16**, 1661-1687 (2004).
- 1384 55. M. J. Ison, R. Quian Quiroga, I. Fried, Rapid Encoding of New Memories by Individual Neurons in the
1385 Human Brain. *Neuron* **87**, 220-230 (2015).
- 1386 56. R. Oostenveld, P. Fries, E. Maris, J. M. Schoffelen, FieldTrip: Open source software for advanced analysis
1387 of MEG, EEG, and invasive electrophysiological data. *Comput Intell Neurosci* **2011**, 156869 (2011).
- 1388 57. J. F. Hipp, D. J. Hawellek, M. Corbetta, M. Siegel, A. K. Engel, Large-scale cortical correlation structure
1389 of spontaneous oscillatory activity. *Nat Neurosci* **15**, 884-890 (2012).
- 1390 58. Y. Benjamini, Y. Hochberg, Controlling the False Discovery Rate - a Practical and Powerful Approach to
1391 Multiple Testing. *J R Stat Soc B* **57**, 289-300 (1995).
- 1392 59. G. Nolte *et al.*, Robustly estimating the flow direction of information in complex physical systems. *Phys
1393 Rev Lett* **100**, 234101 (2008).
- 1394 60. P. B. Sederberg *et al.*, Hippocampal and neocortical gamma oscillations predict memory formation in
1395 humans. *Cereb Cortex* **17**, 1190-1196 (2007).
- 1396 61. J. F. Burke *et al.*, Synchronous and asynchronous theta and gamma activity during episodic memory
1397 formation. *J Neurosci* **33**, 292-304 (2013).
- 1398 62. M. A. Belluscio, K. Mizuseki, R. Schmidt, R. Kempter, G. Buzsaki, Cross-frequency phase-phase coupling
1399 between theta and gamma oscillations in the hippocampus. *J Neurosci* **32**, 423-435 (2012).
- 1400 63. M. R. Cohen, A. Kohn, Measuring and interpreting neuronal correlations. *Nat Neurosci* **14**, 811-819
1401 (2011).
- 1402 64. J. Niediek, J. Bostrom, C. E. Elger, F. Mormann, Reliable Analysis of Single-Unit Recordings from the
1403 Human Brain under Noisy Conditions: Tracking Neurons over Hours. *PLoS One* **11**, e0166598 (2016).

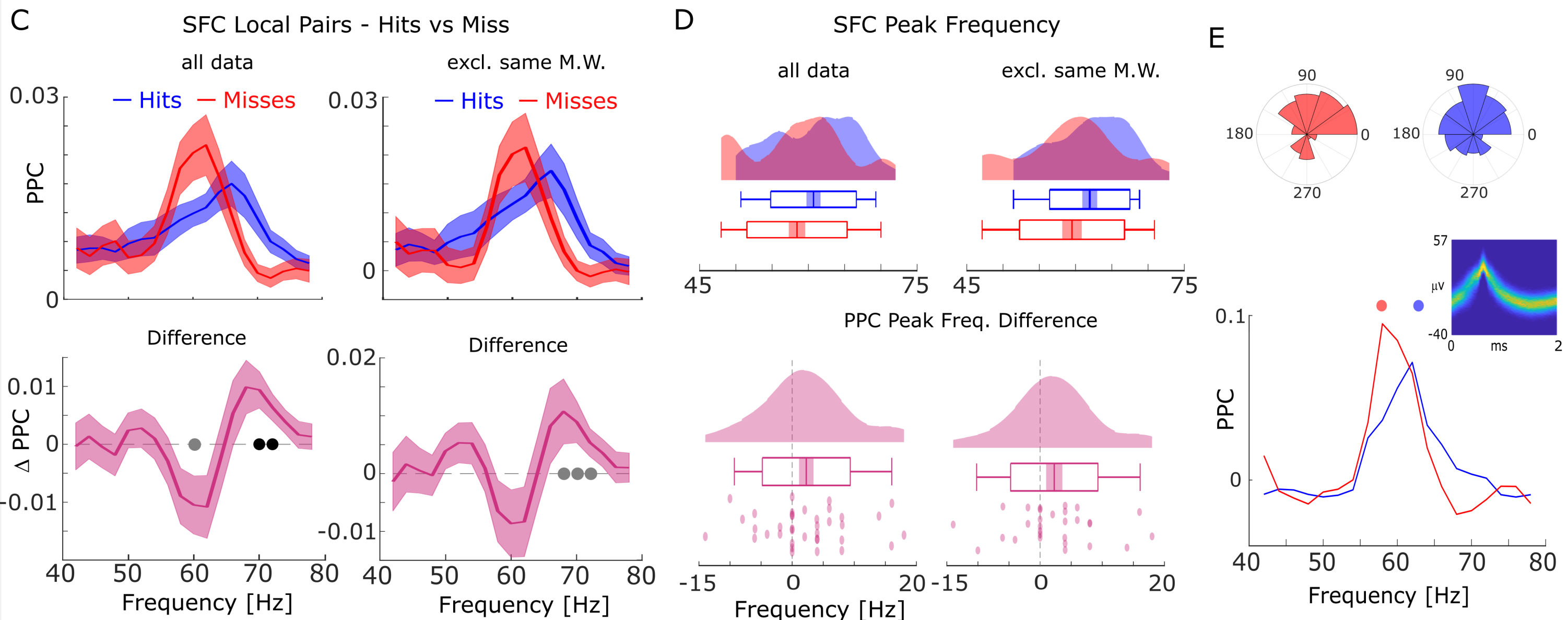
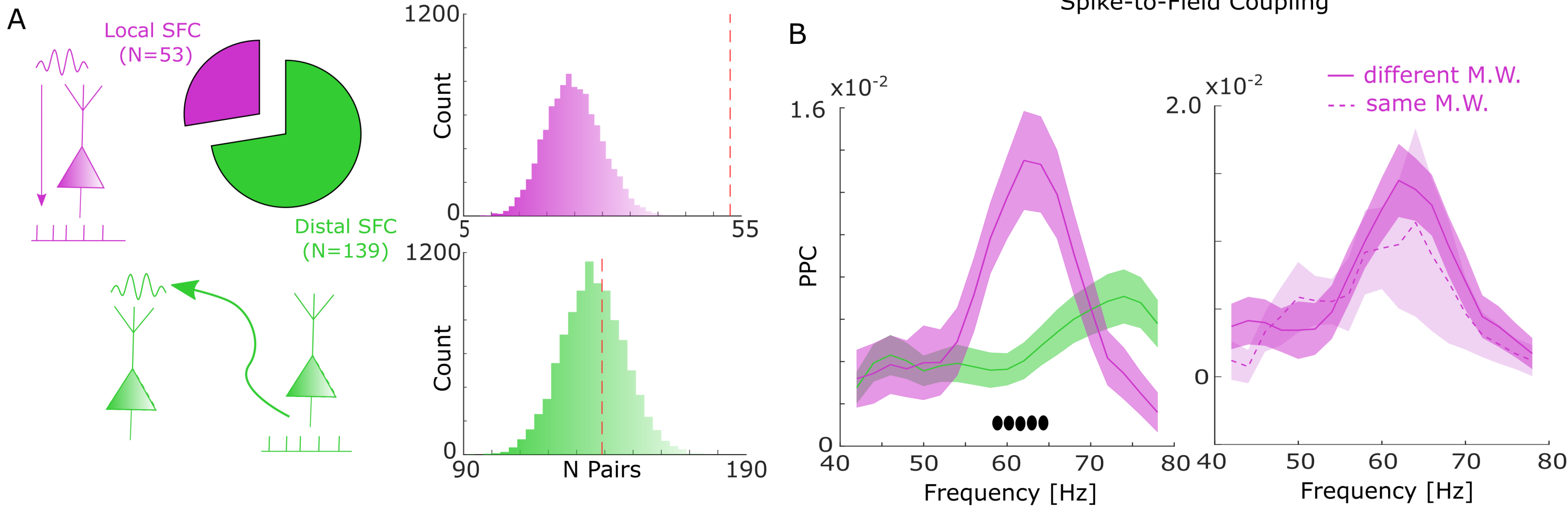
A

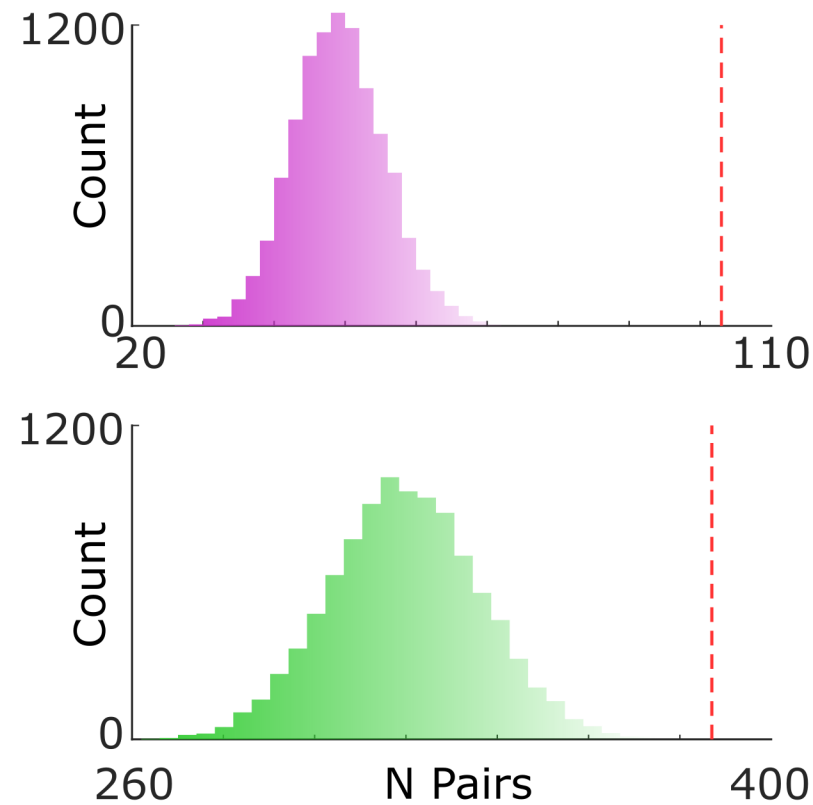
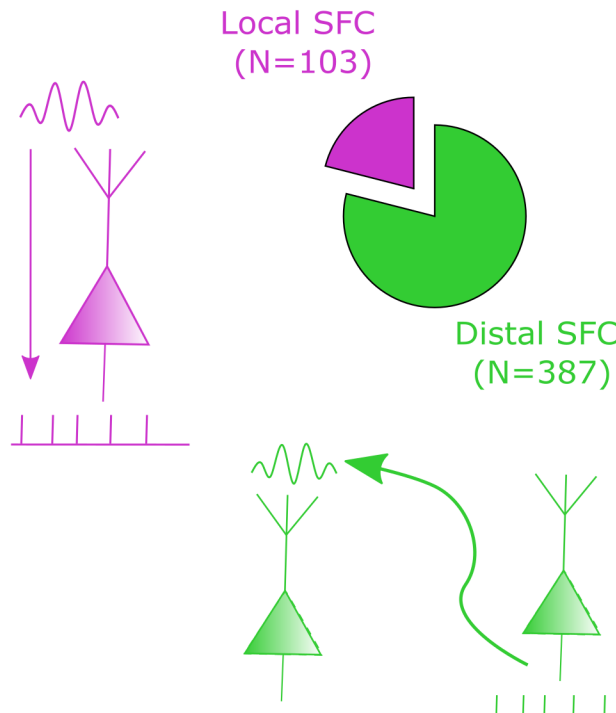
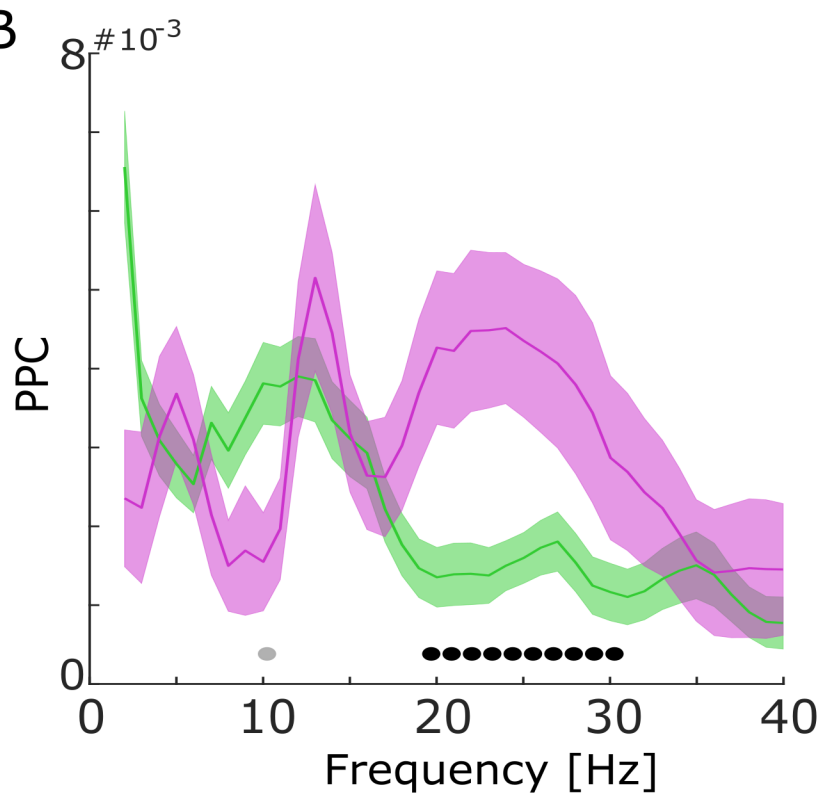
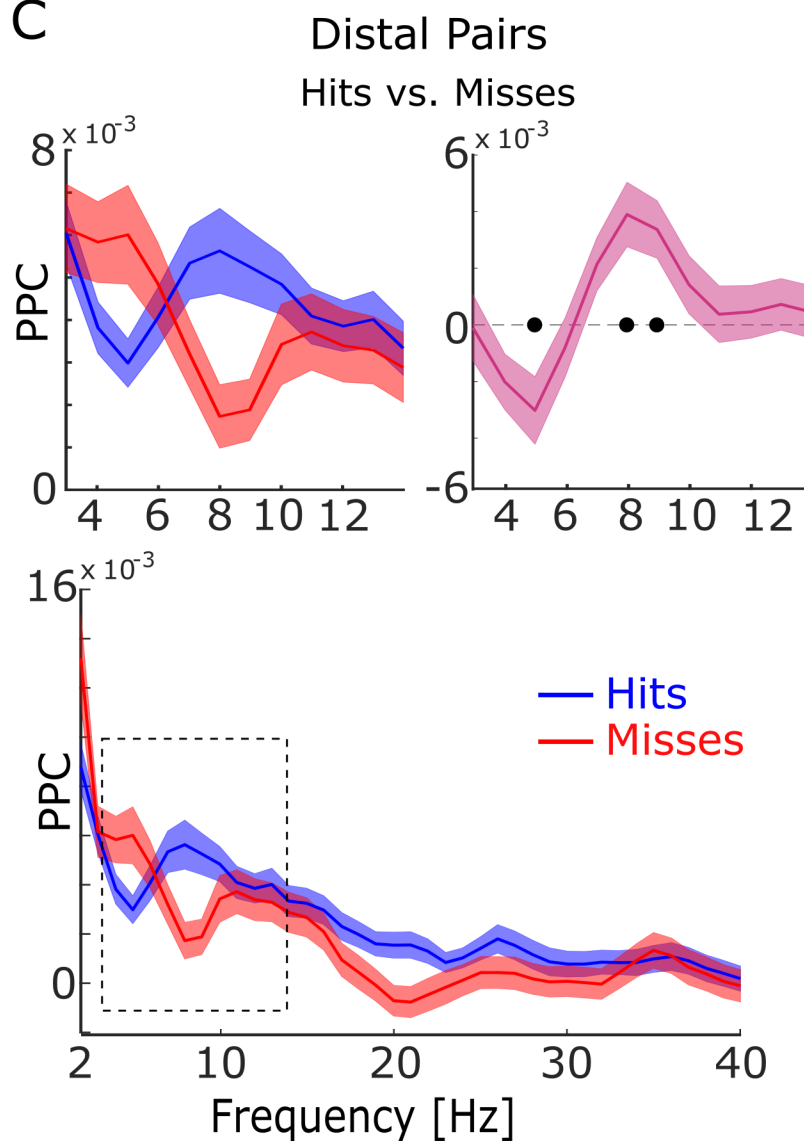
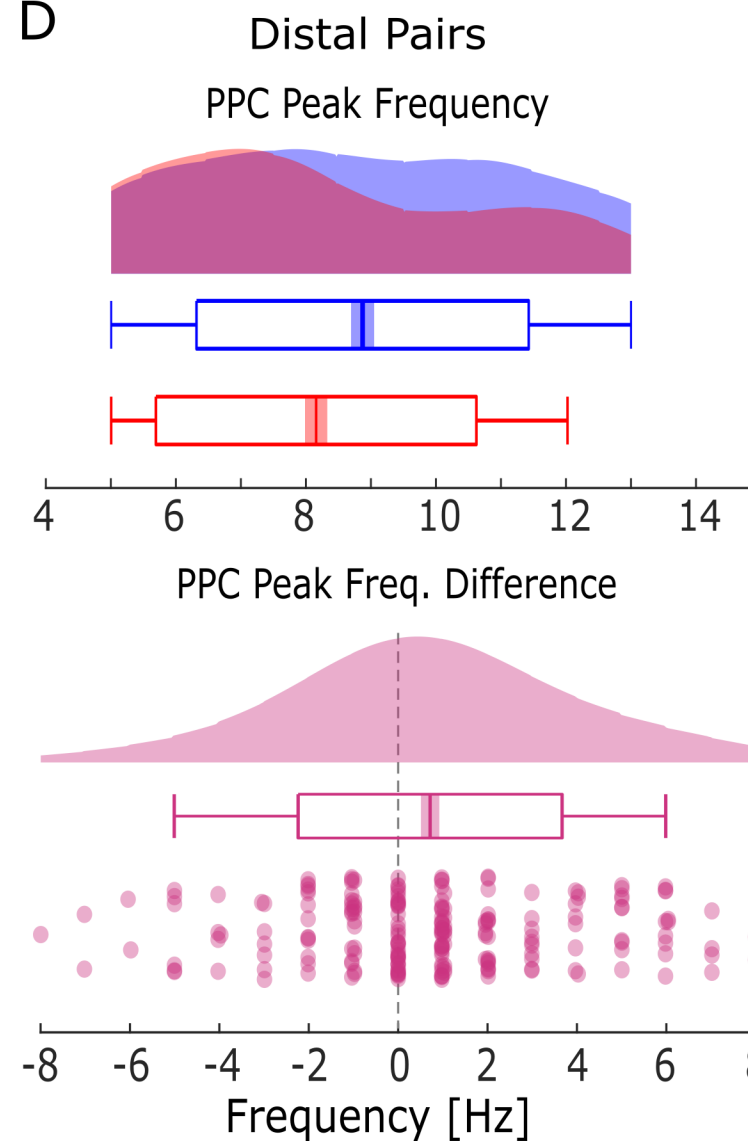
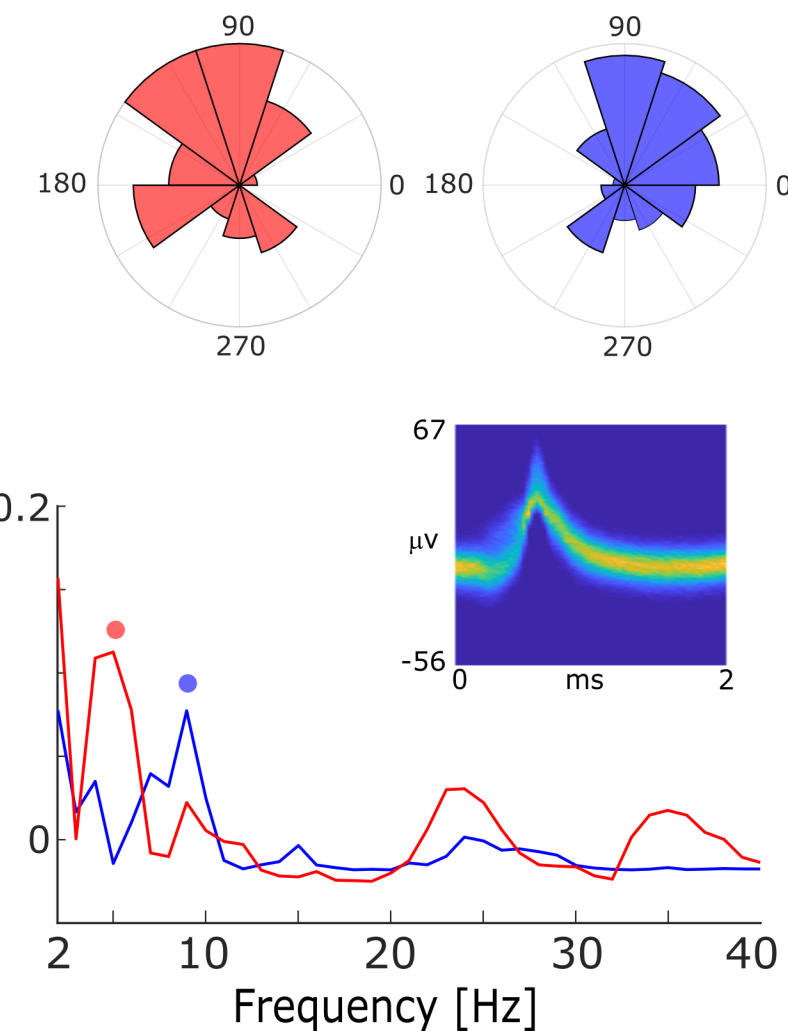
Associative Encoding



Cued Recall

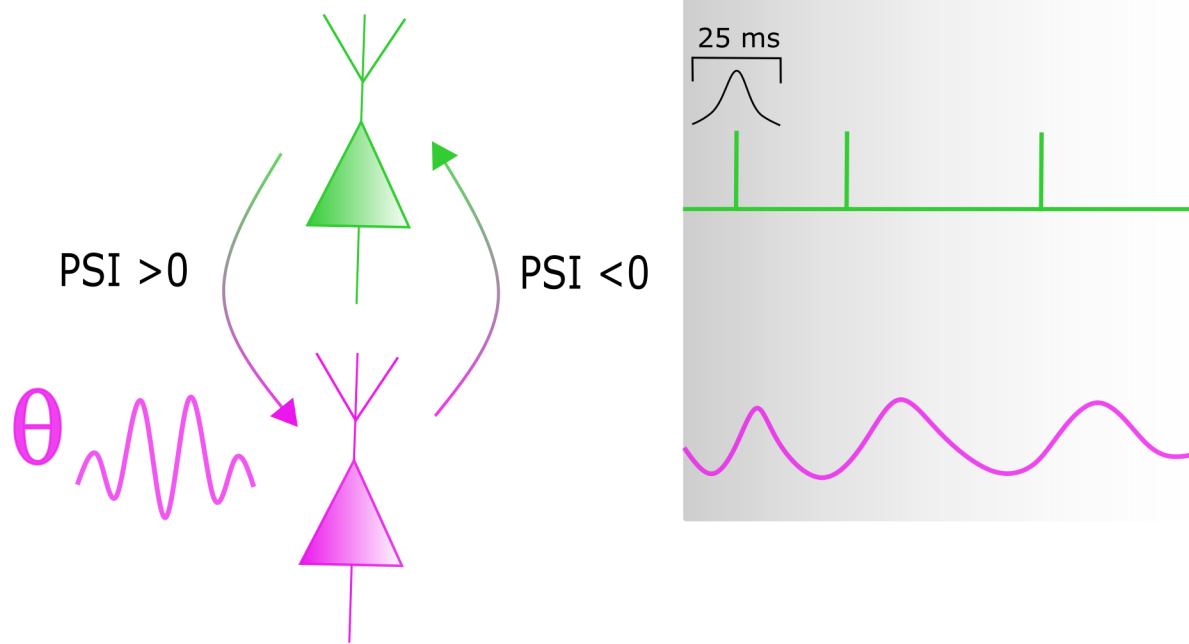
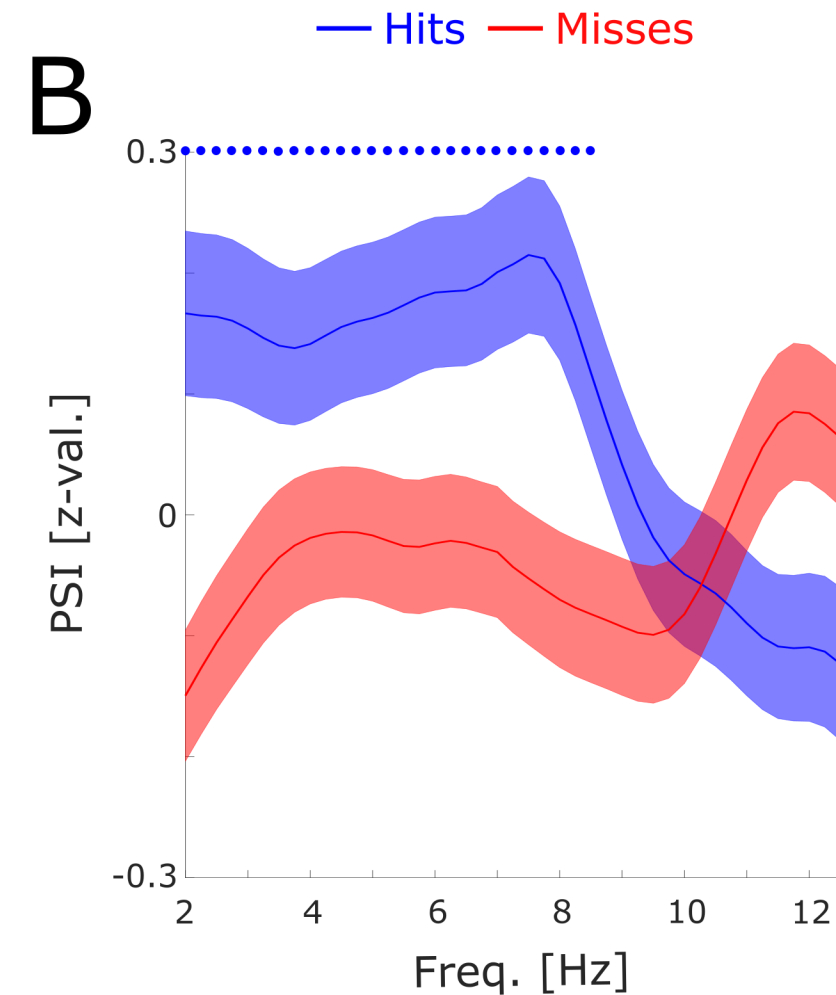
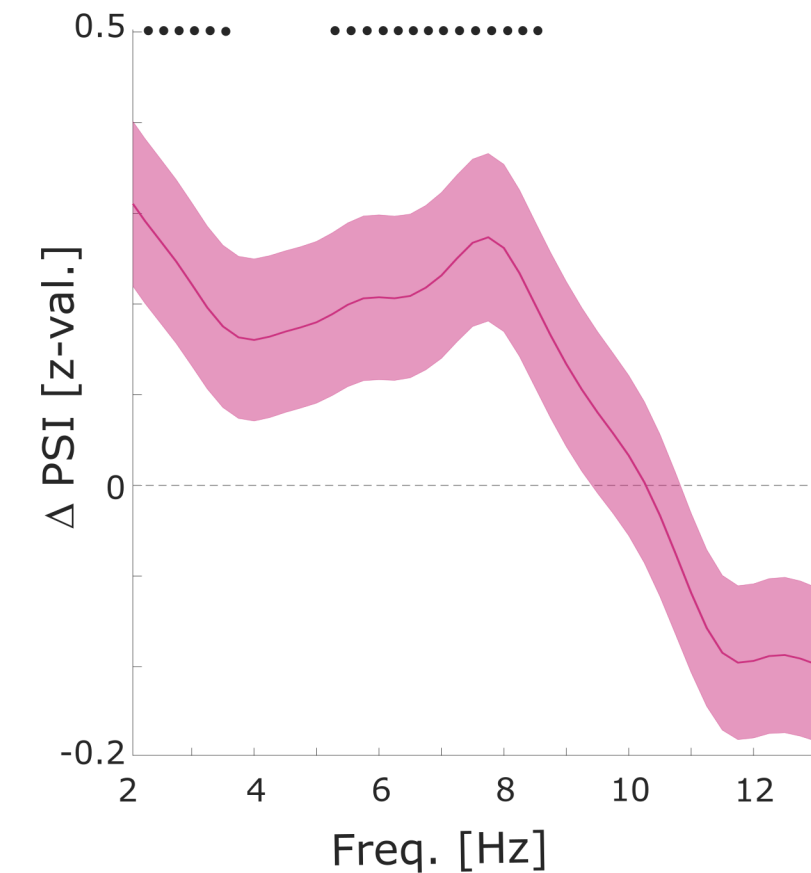
**B****C****D**

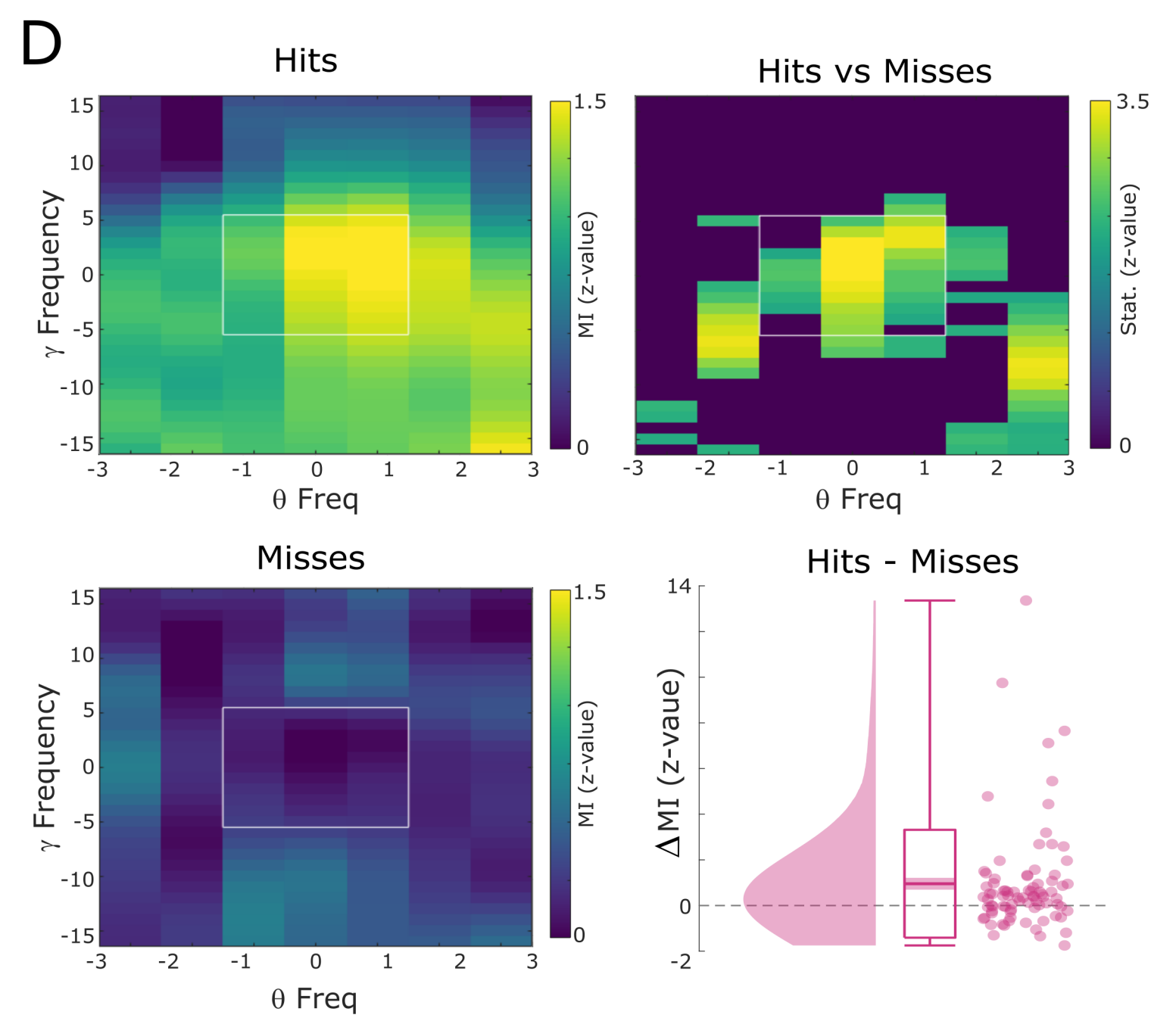
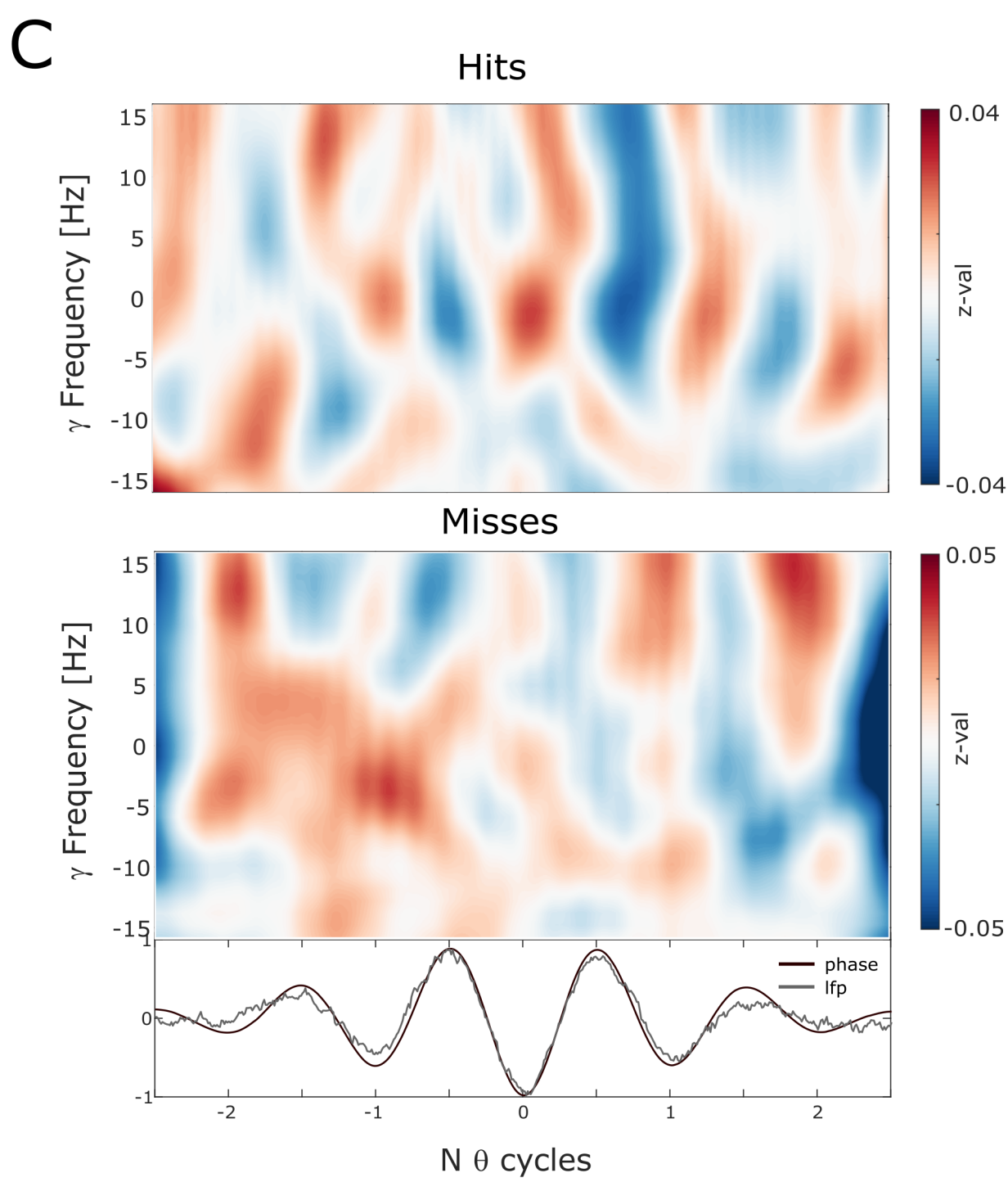
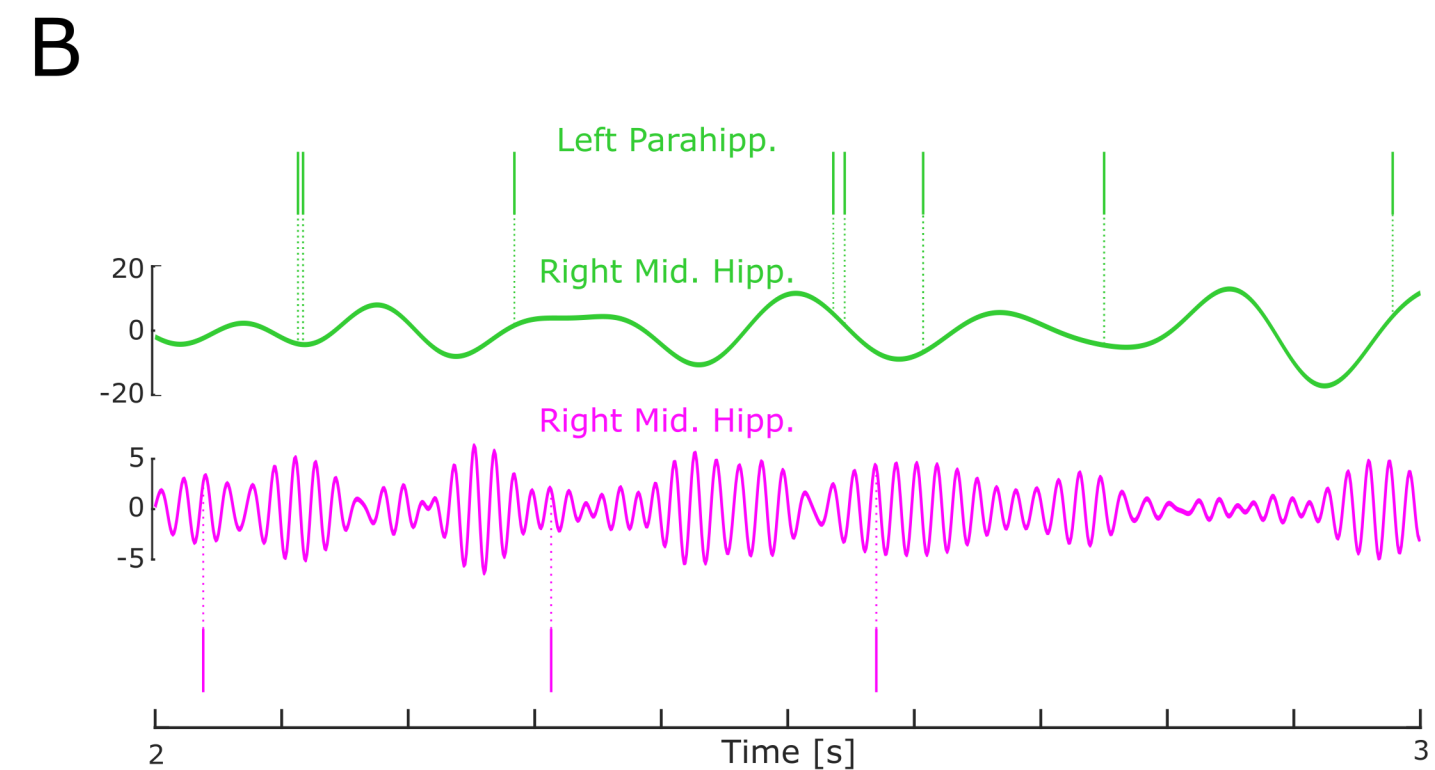
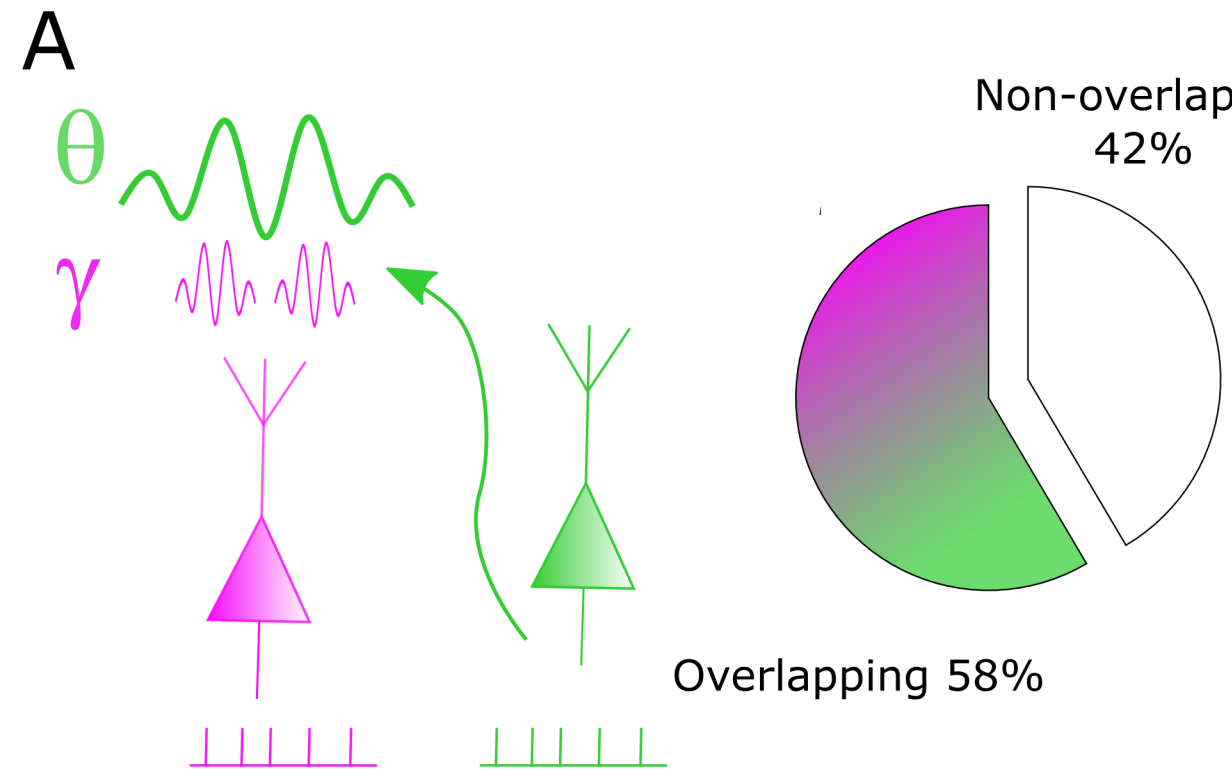


A**B****C****D****E**

A

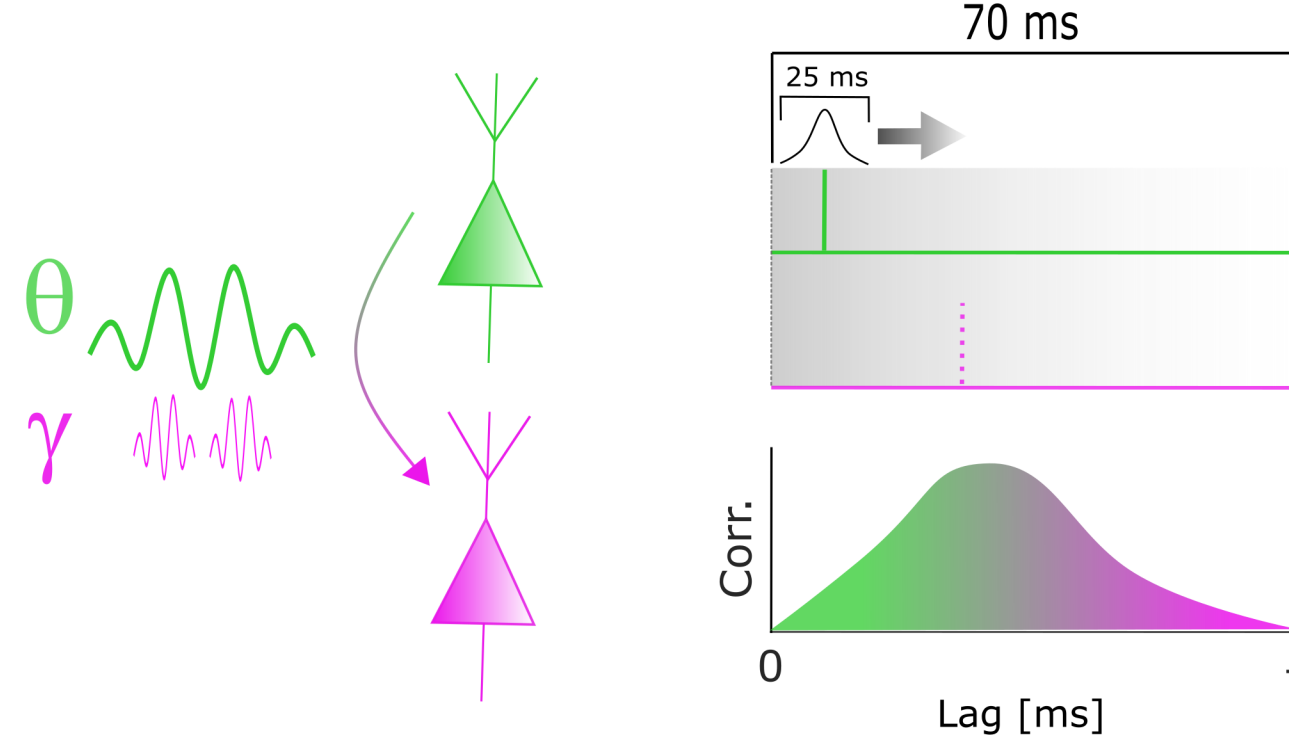
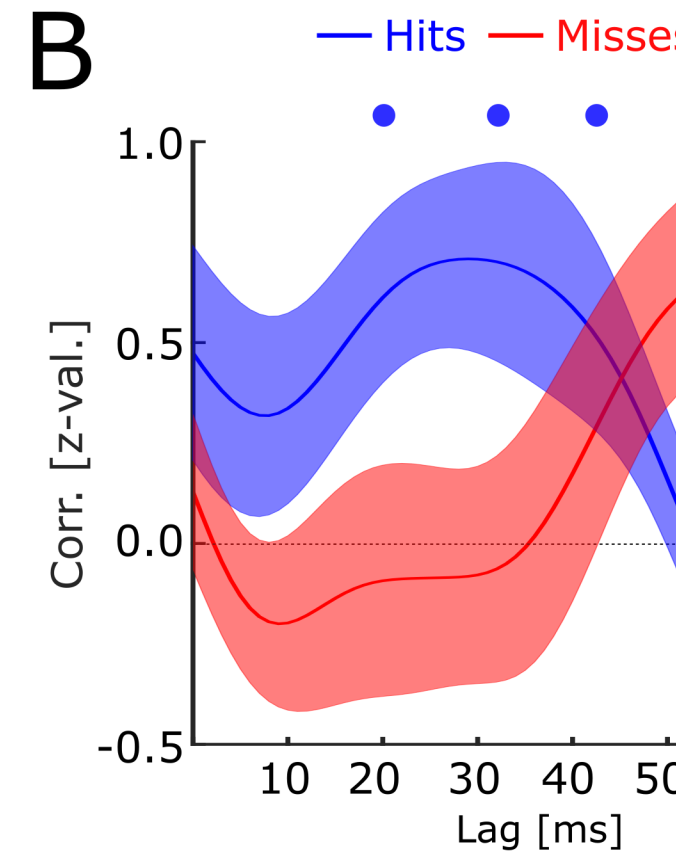
Directional Coupling (PSI) Analysis

**B****Hits - Misses**

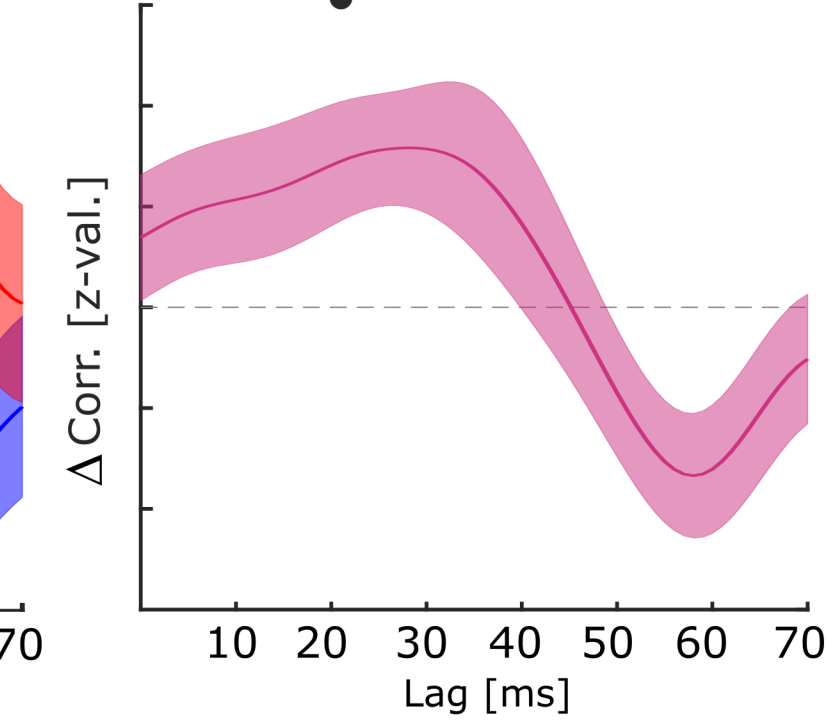
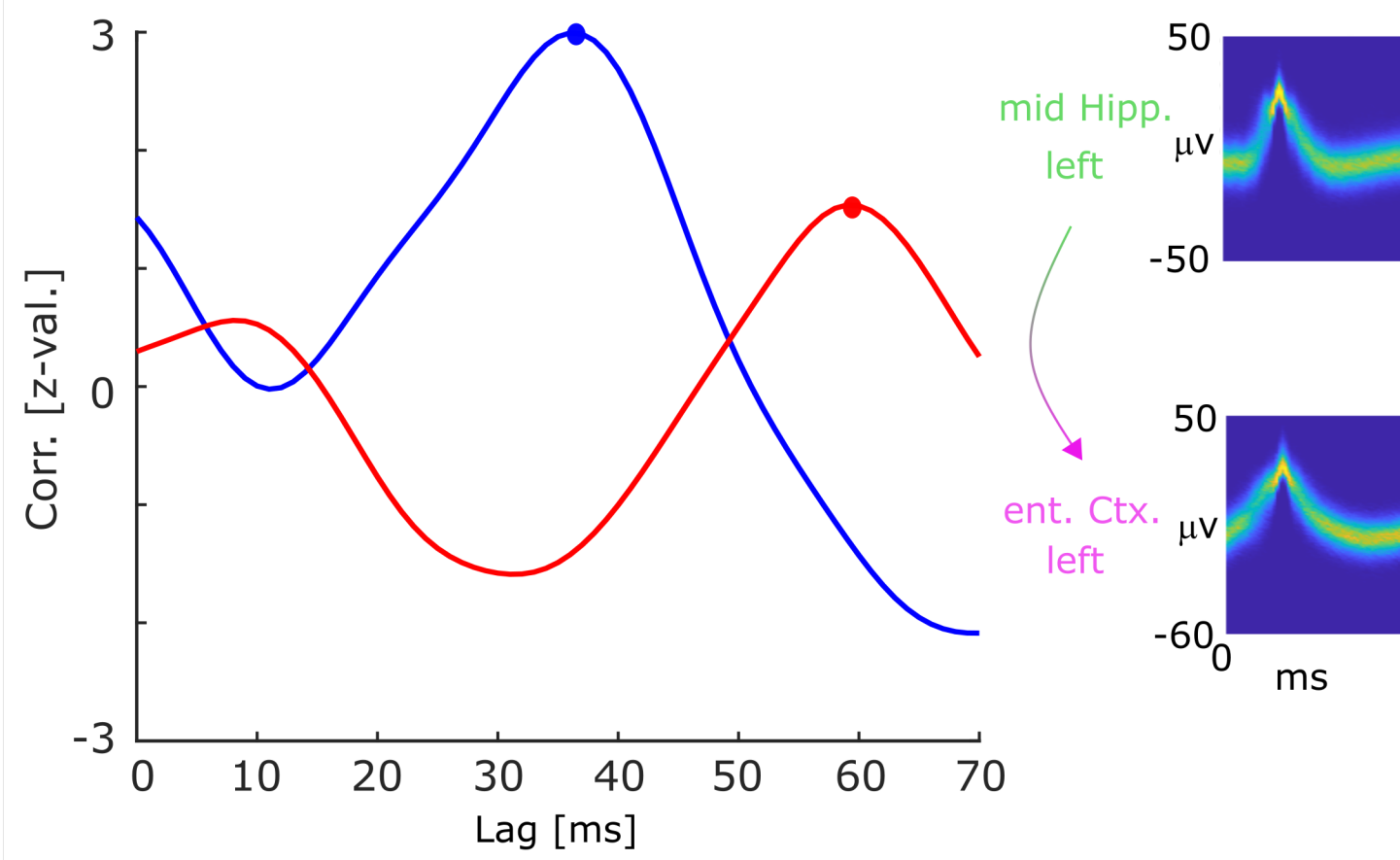


A

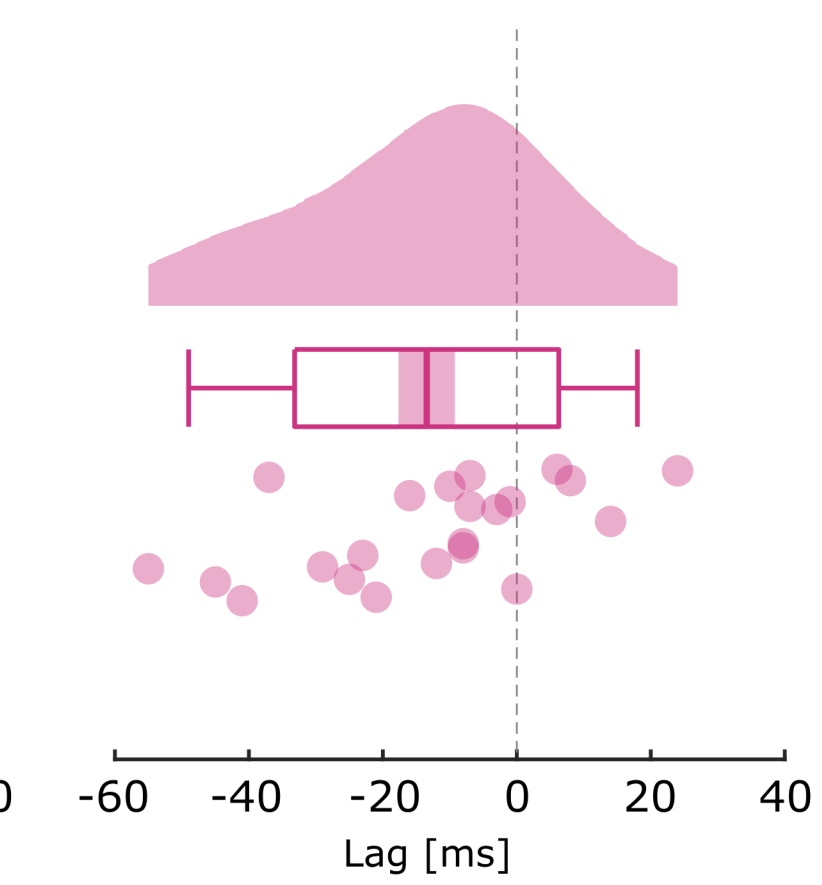
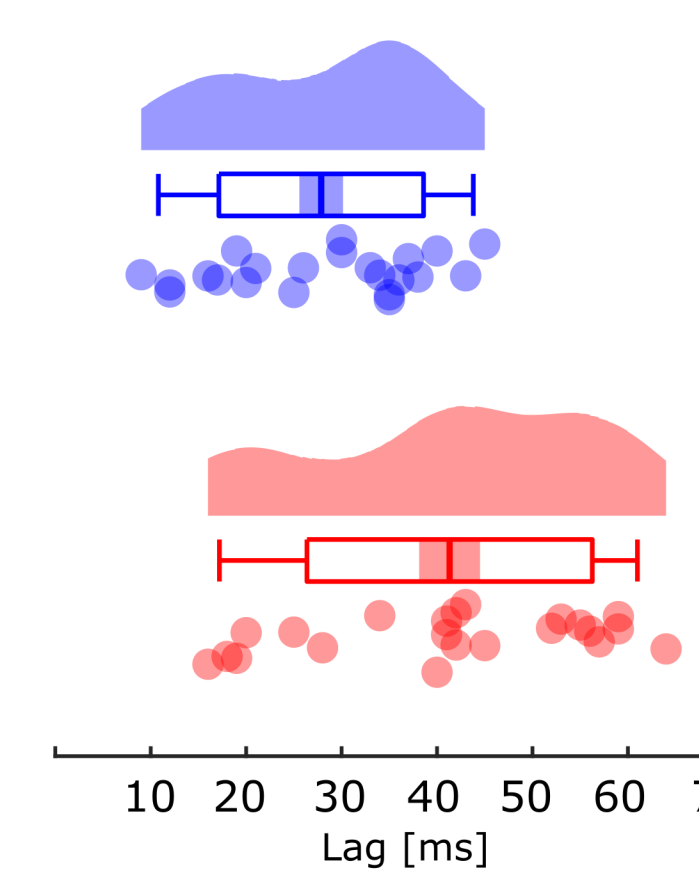
Spike Co-Firing Analysis

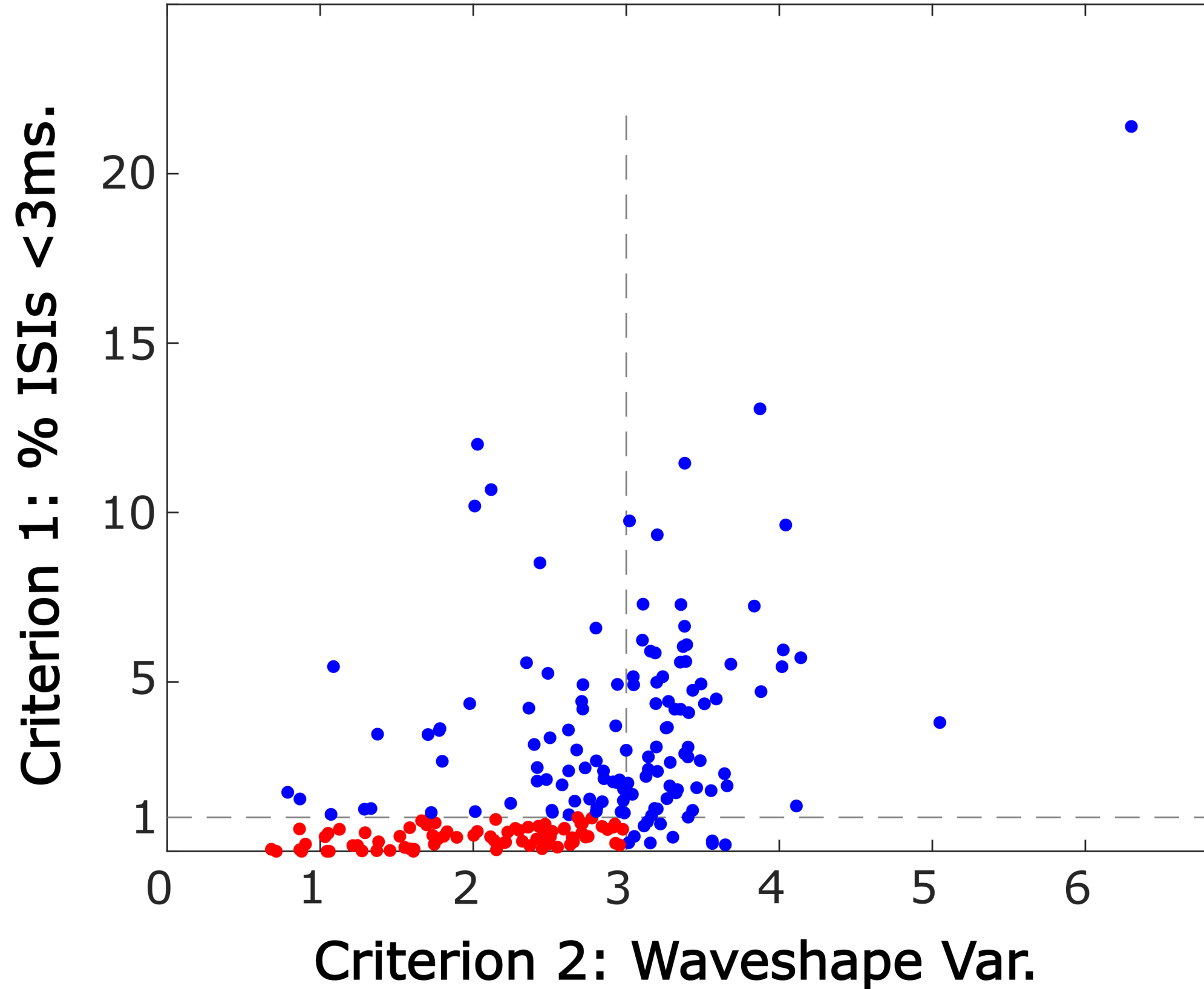
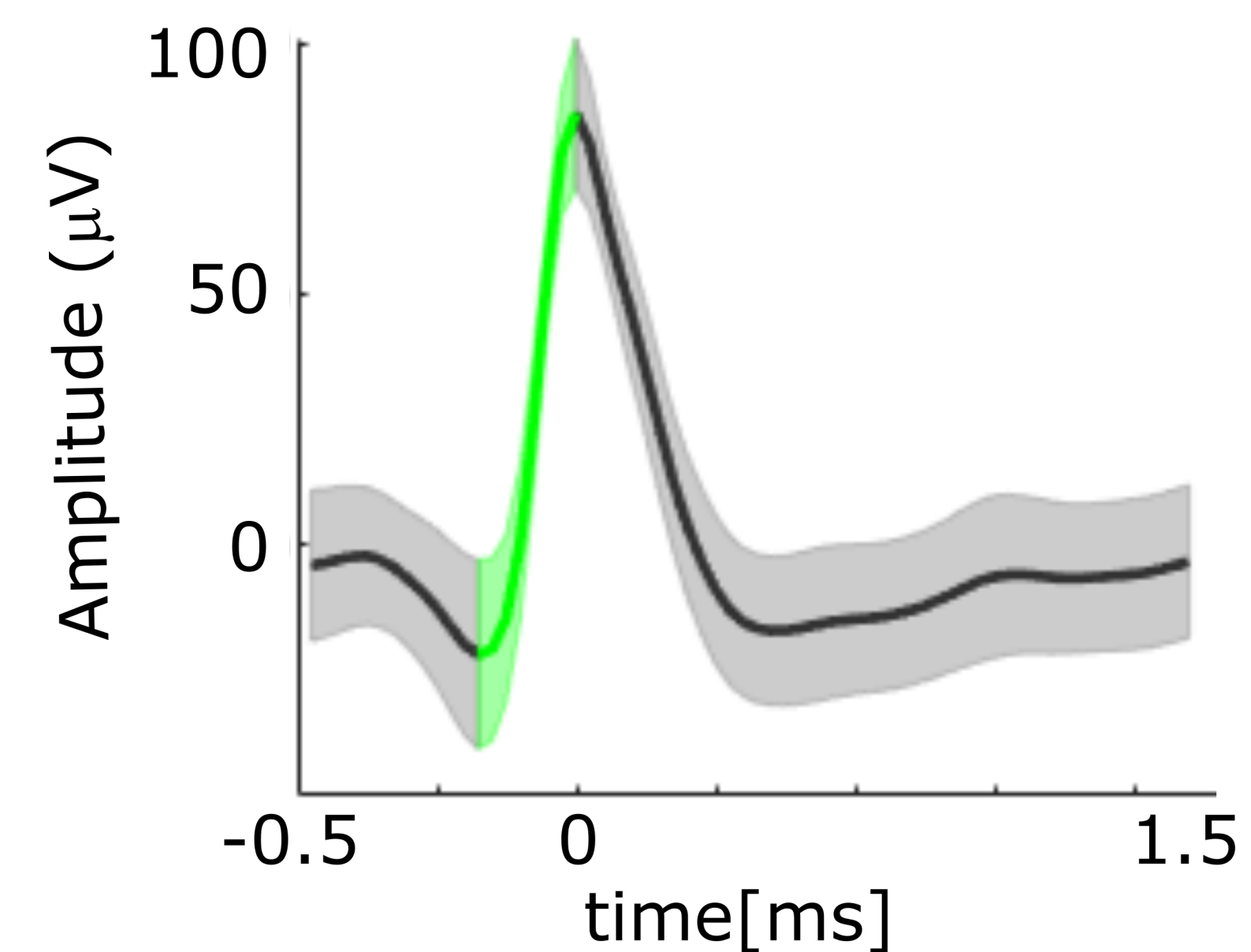
**B**

Hits - Misses

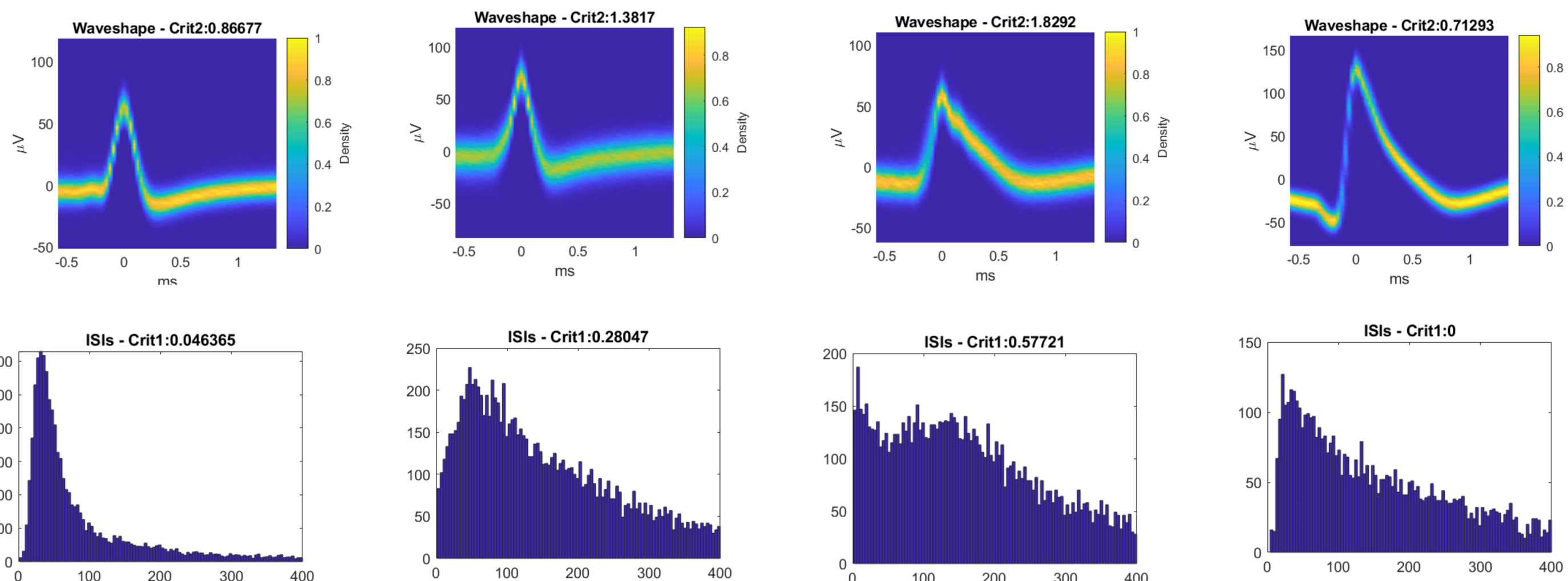
**C****D**

Co-Firing Peaks

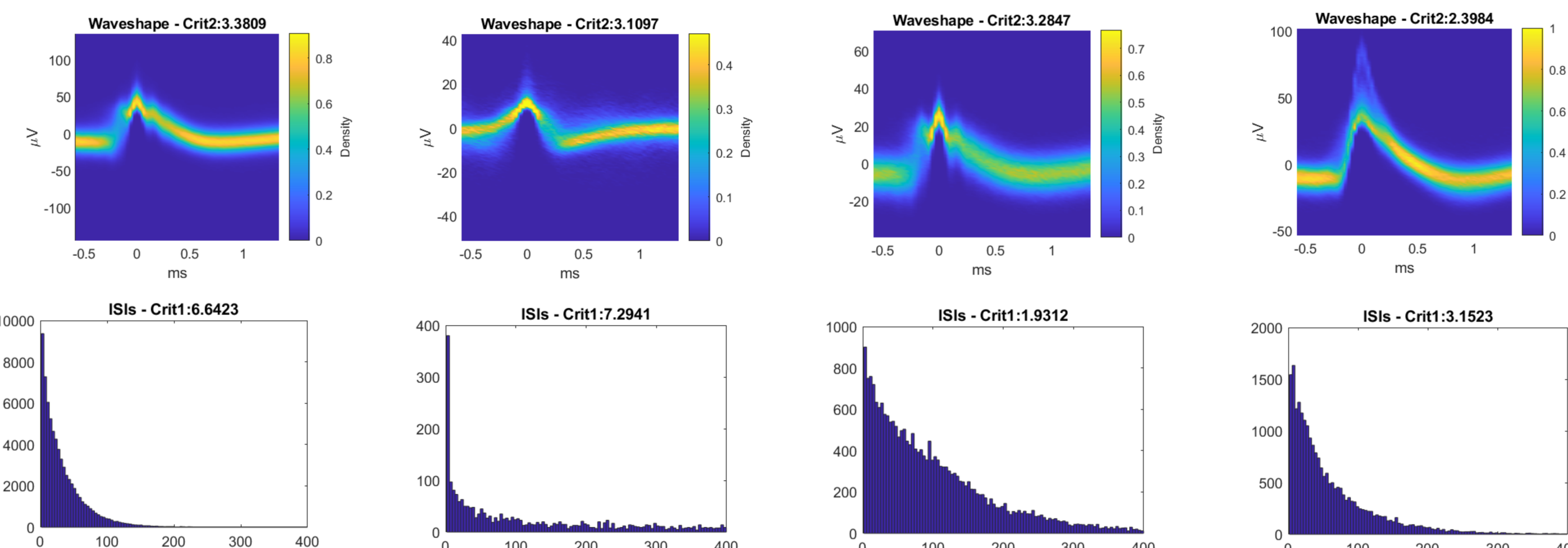


A**N SUAs: 82 N MUAs: 136****B****C**

SUAS

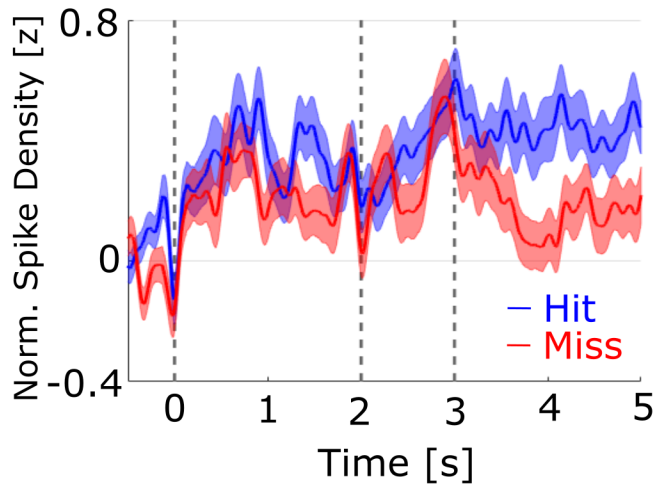


MUAS

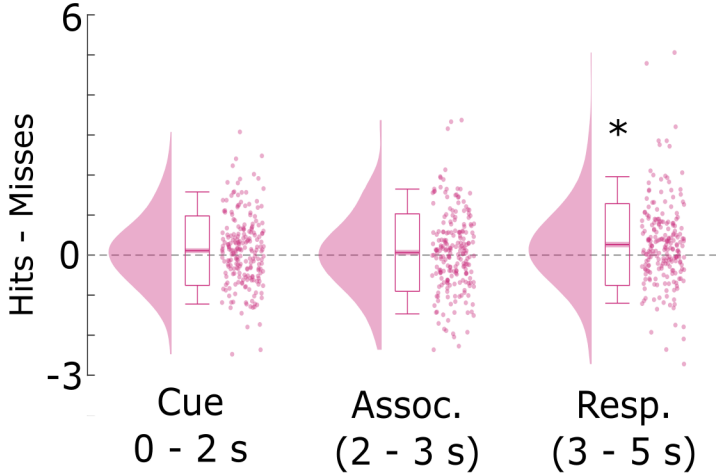


A

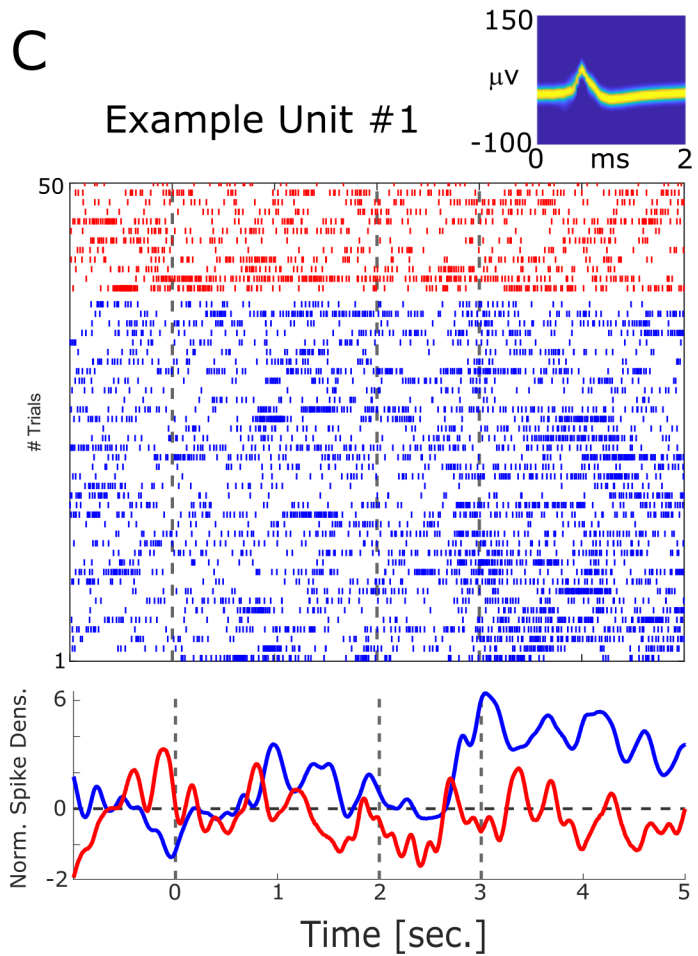
Spike Density (218 Units)

**B**

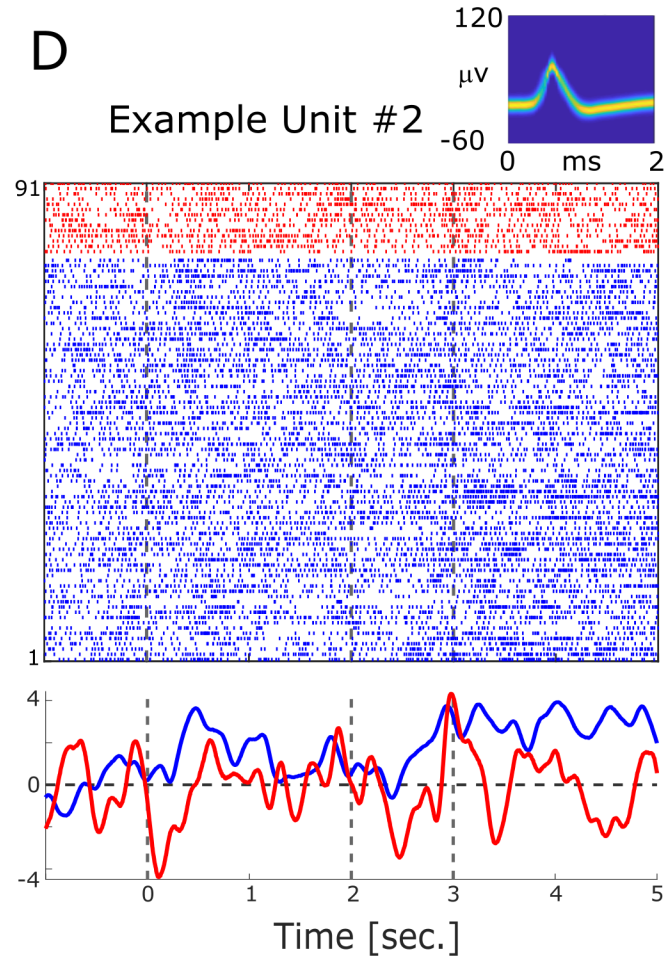
Spk. Dens. per Time Window

**C**

Example Unit #1

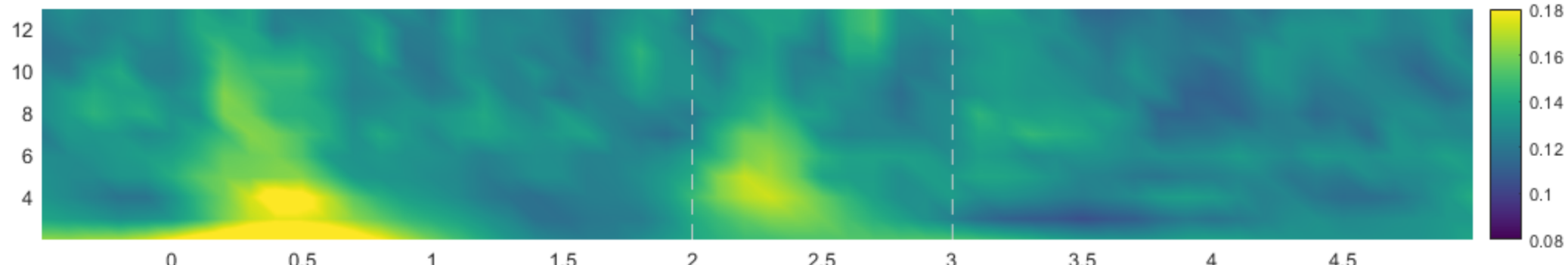
**D**

Example Unit #2



Average ITPC

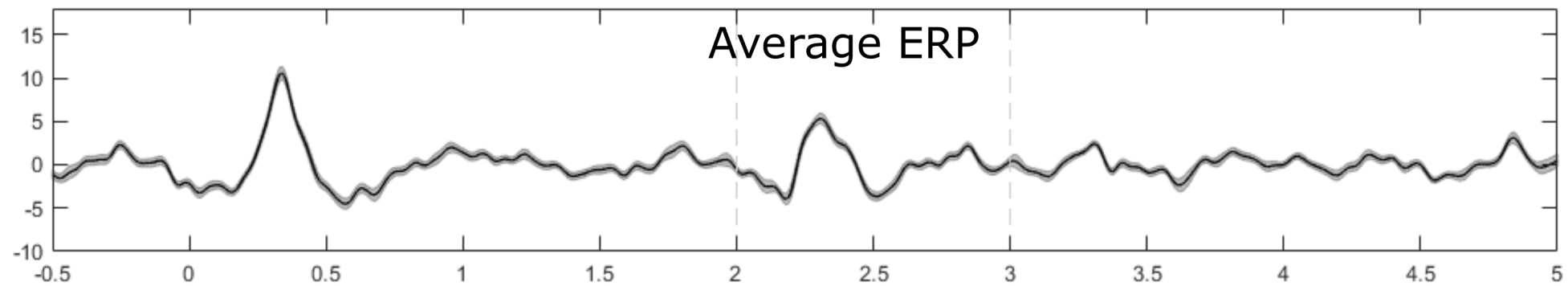
Freq [Hz.]



B

Average ERP

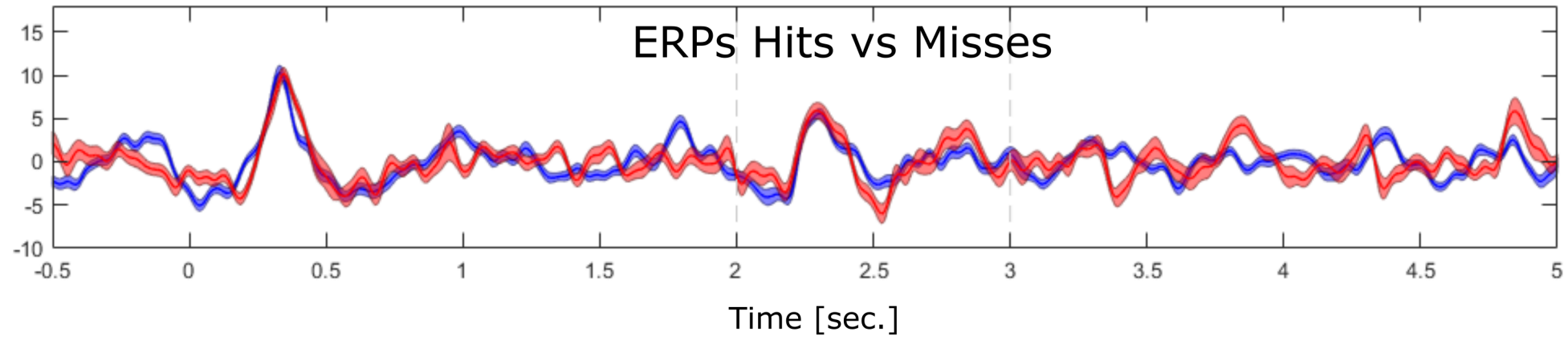
Amp. [a.u.]



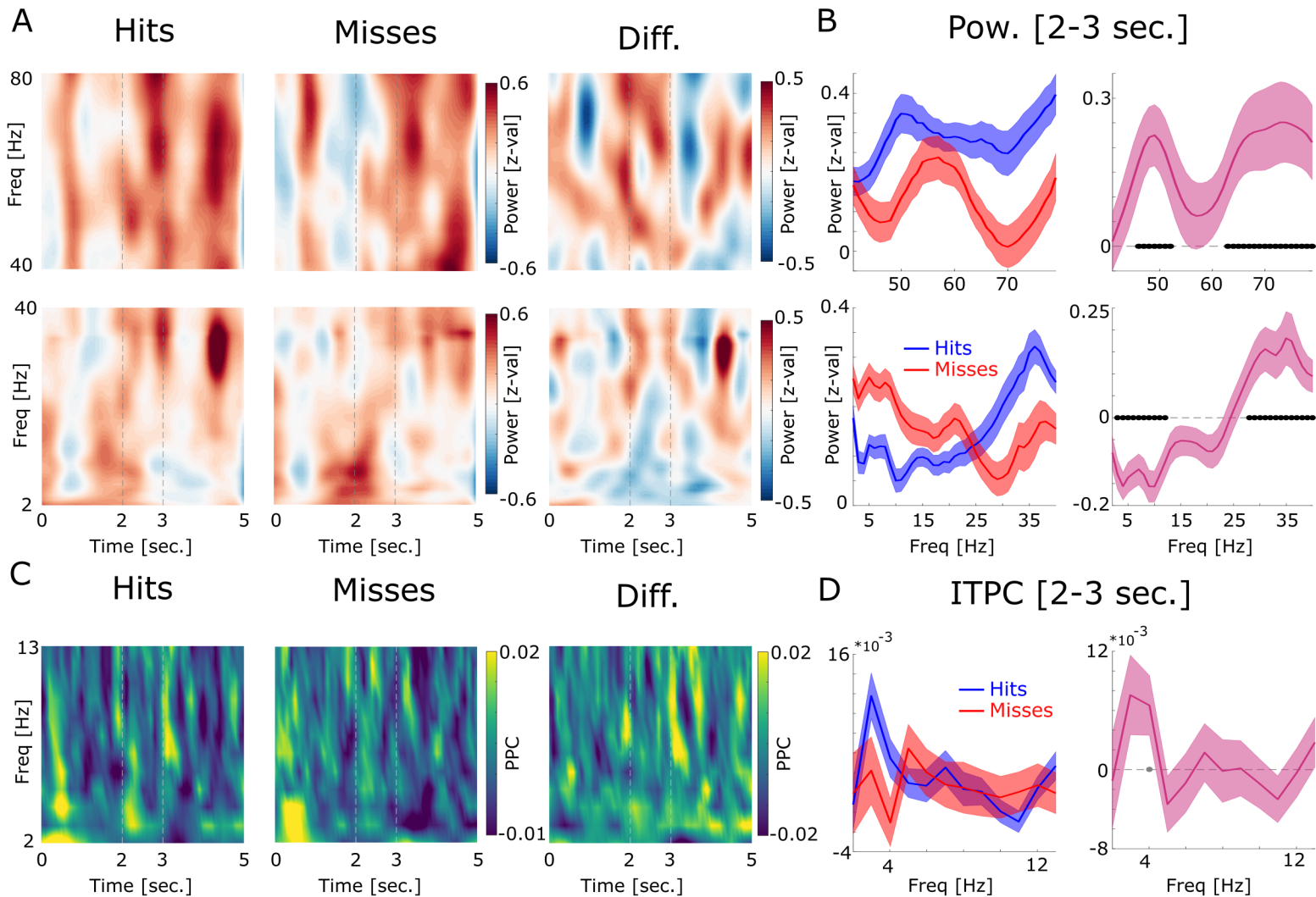
C

ERPs Hits vs Misses

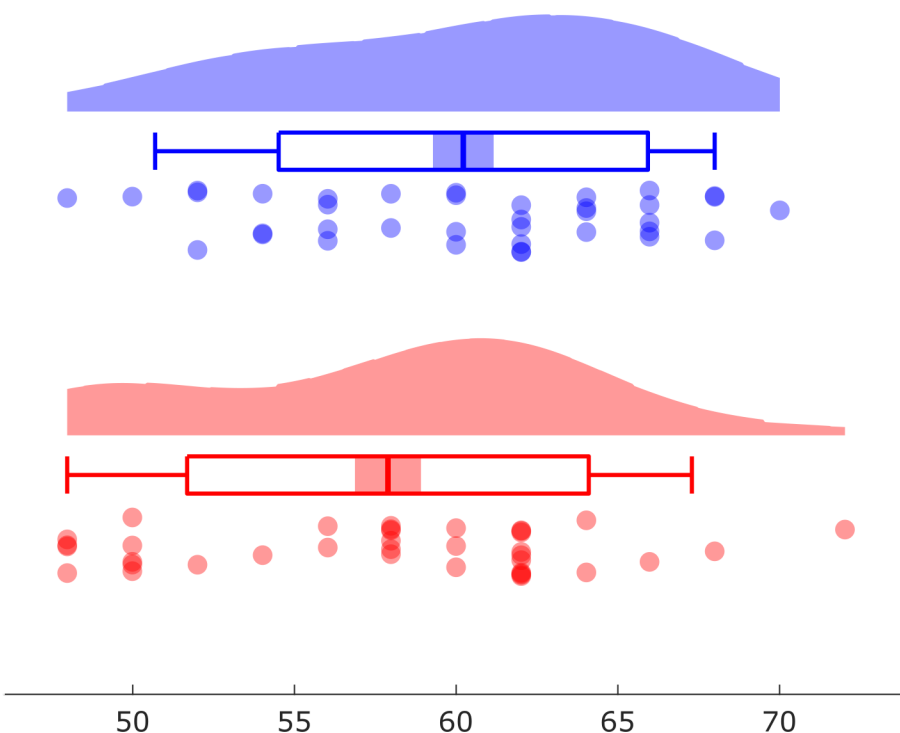
Amp. [a.u.]



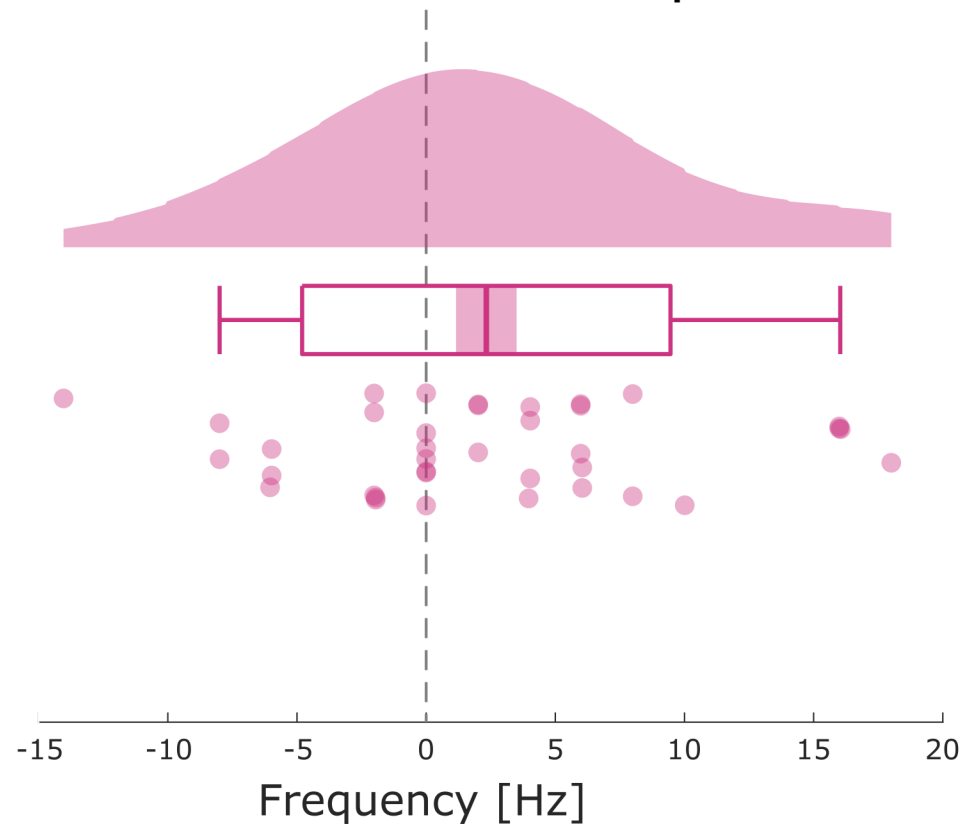
Time [sec.]

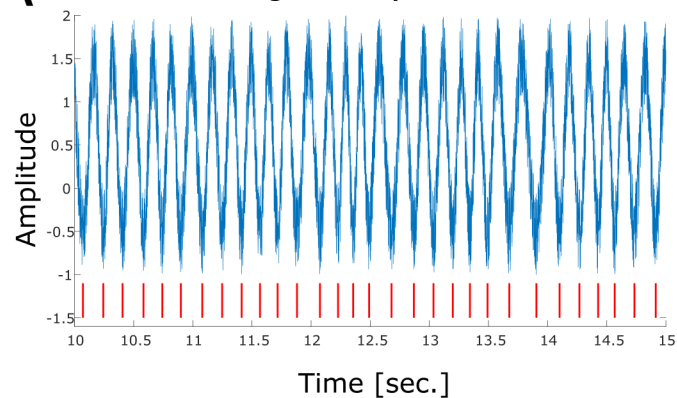
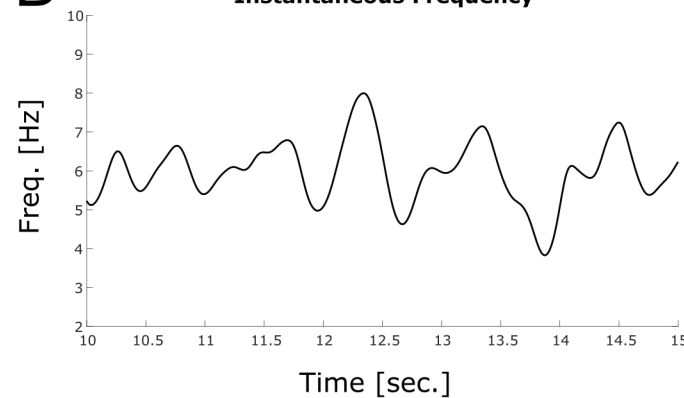
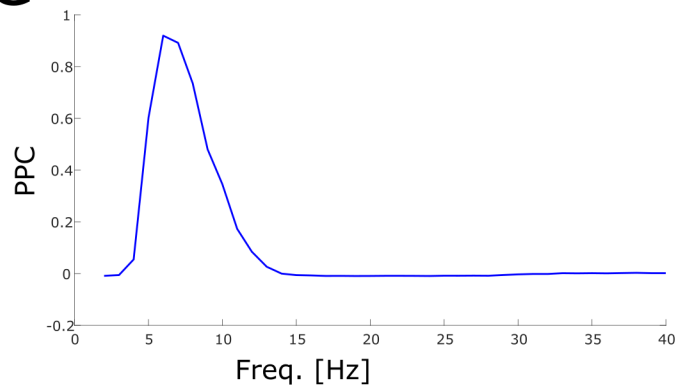
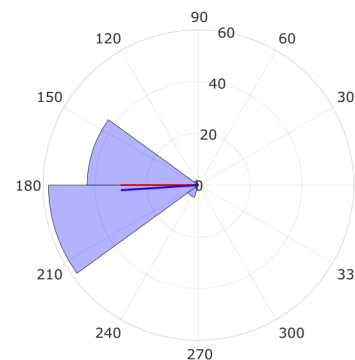


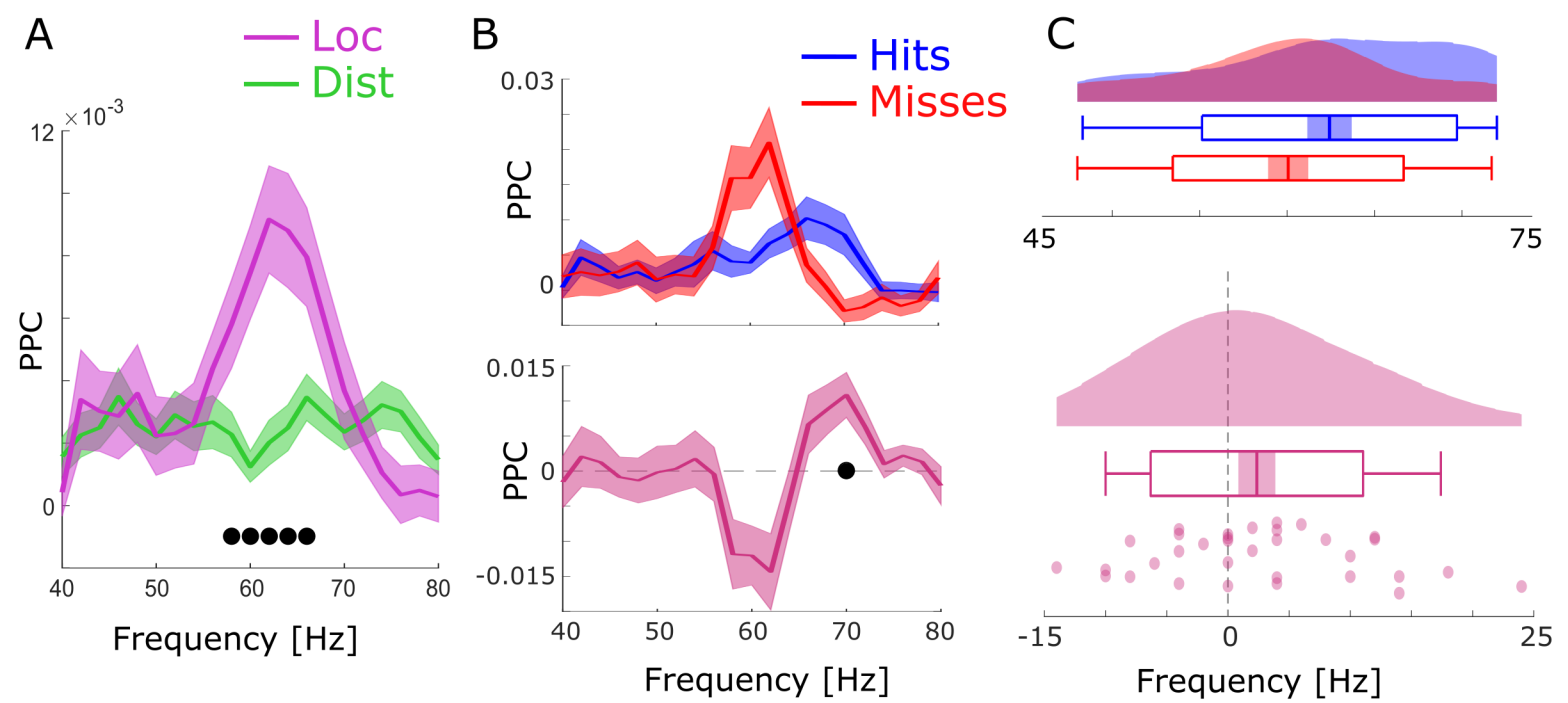
Peak SFC Gamma



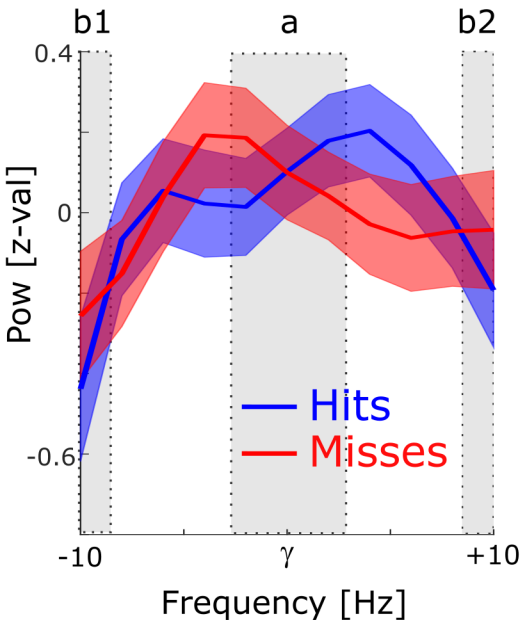
Peak Difference Hits vs Misses -- p=0.027287



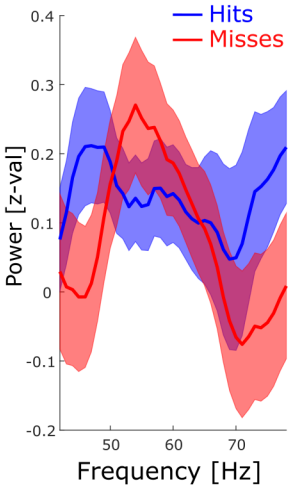
A**Signal and Spikes****B****Instantaneous Frequency****C****PPC Wavelet****D****Spike Phase at:6 Hz**



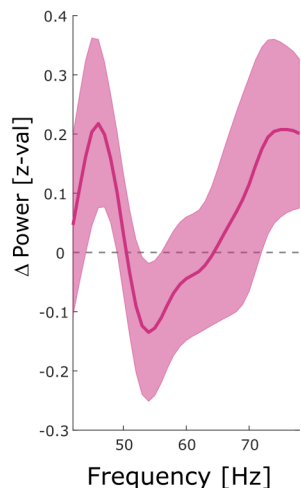
Gamma Power



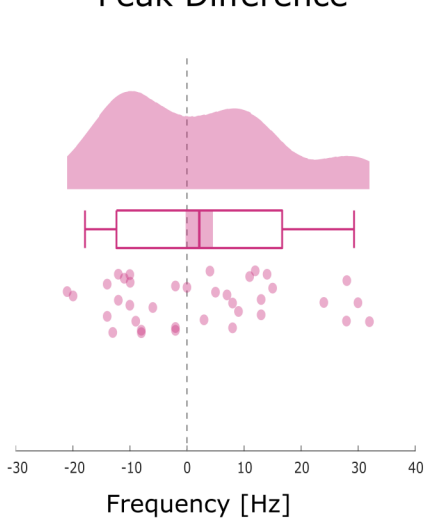
Hits vs. Misses



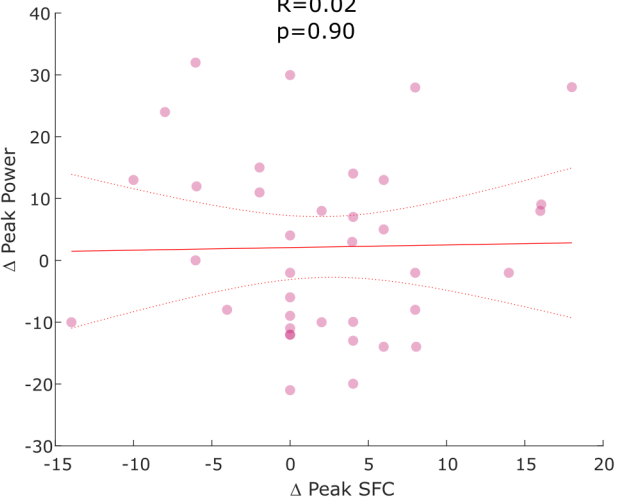
Difference

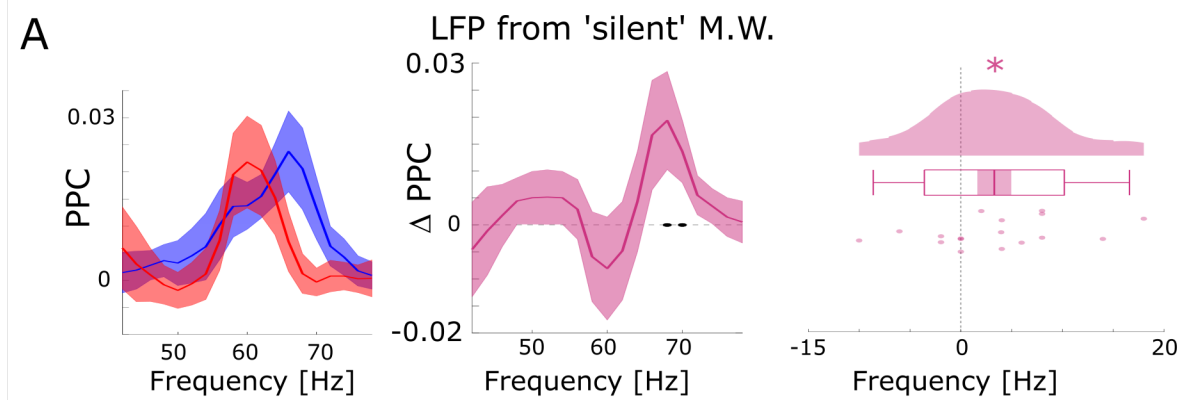


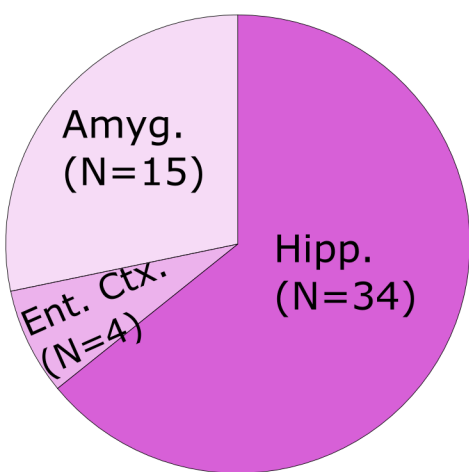
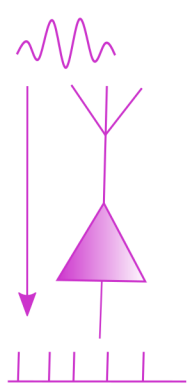
Peak Difference



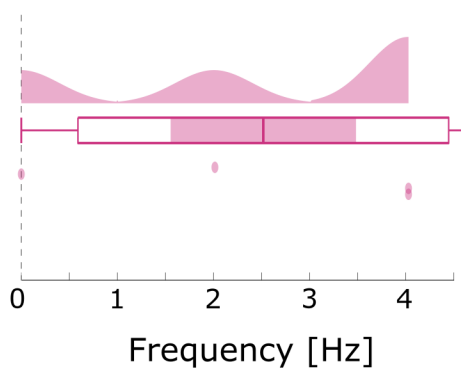
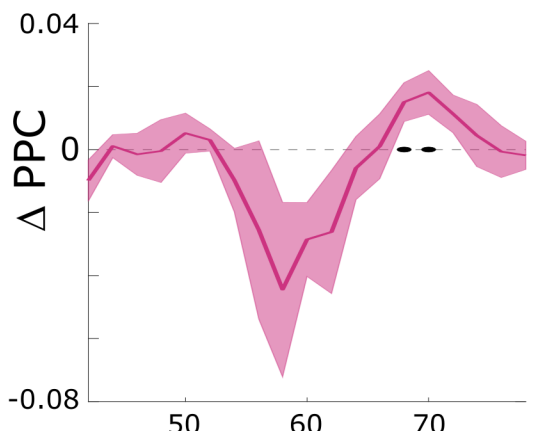
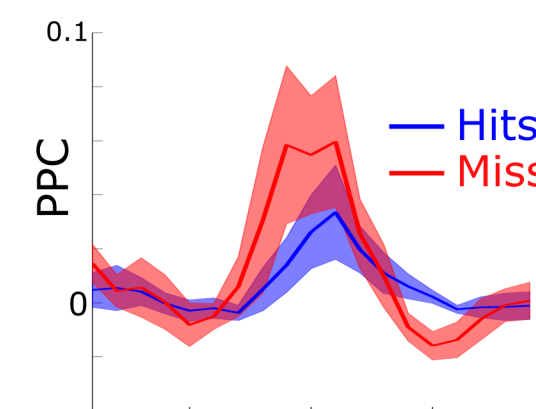
$R=0.02$
 $p=0.90$



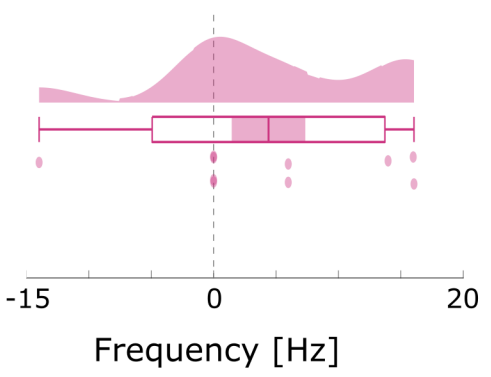
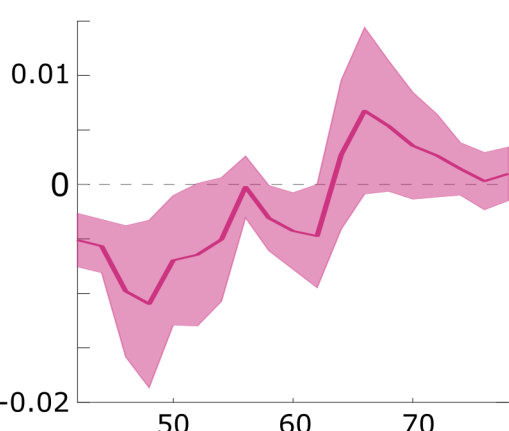
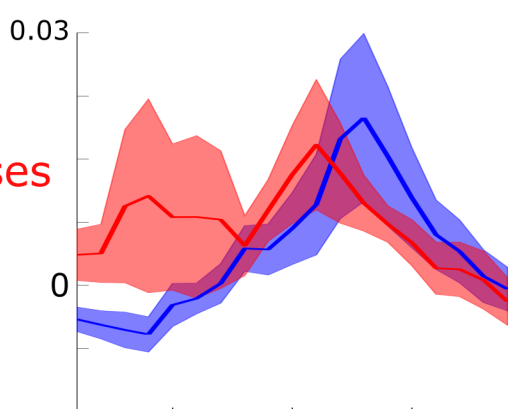
A



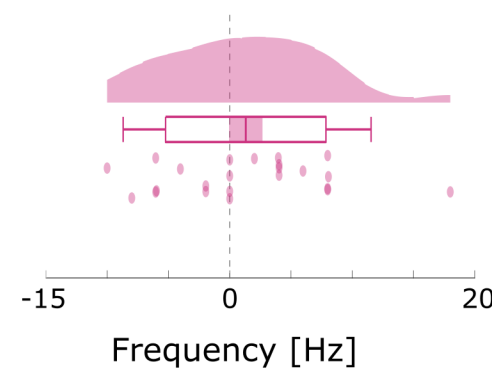
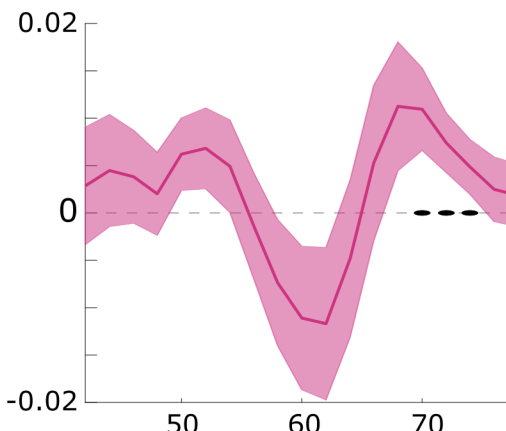
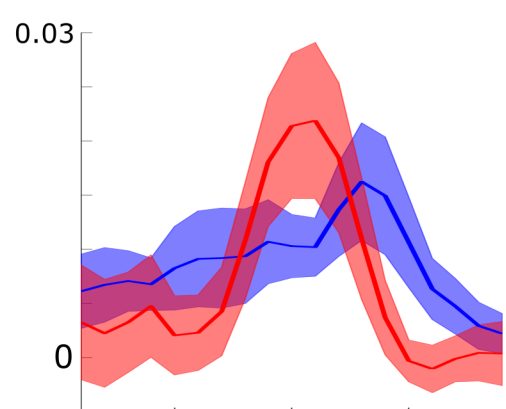
Entorhinal Cortex.



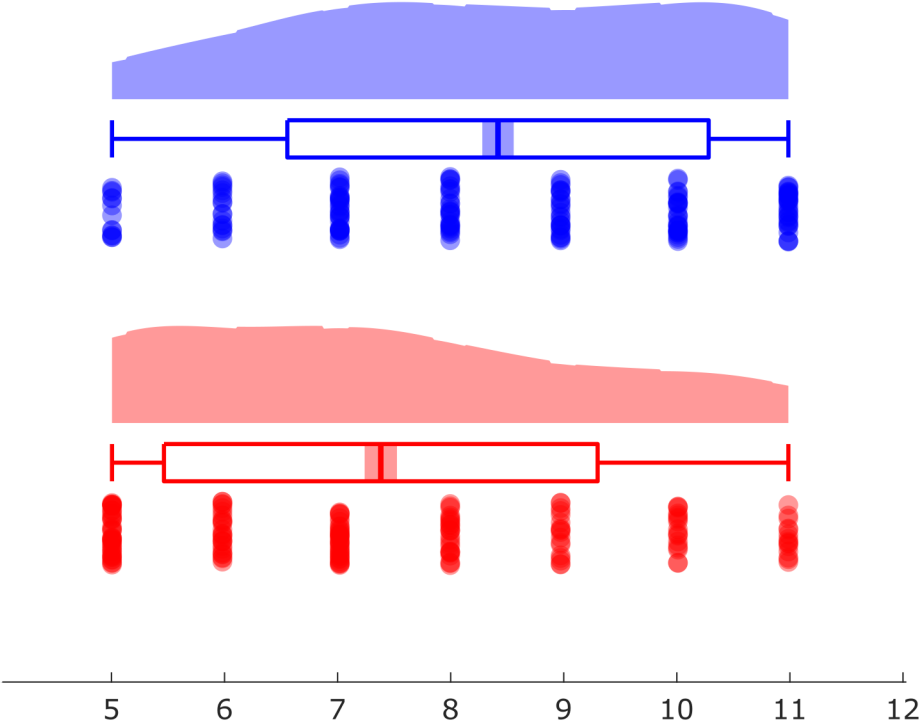
Amygdala



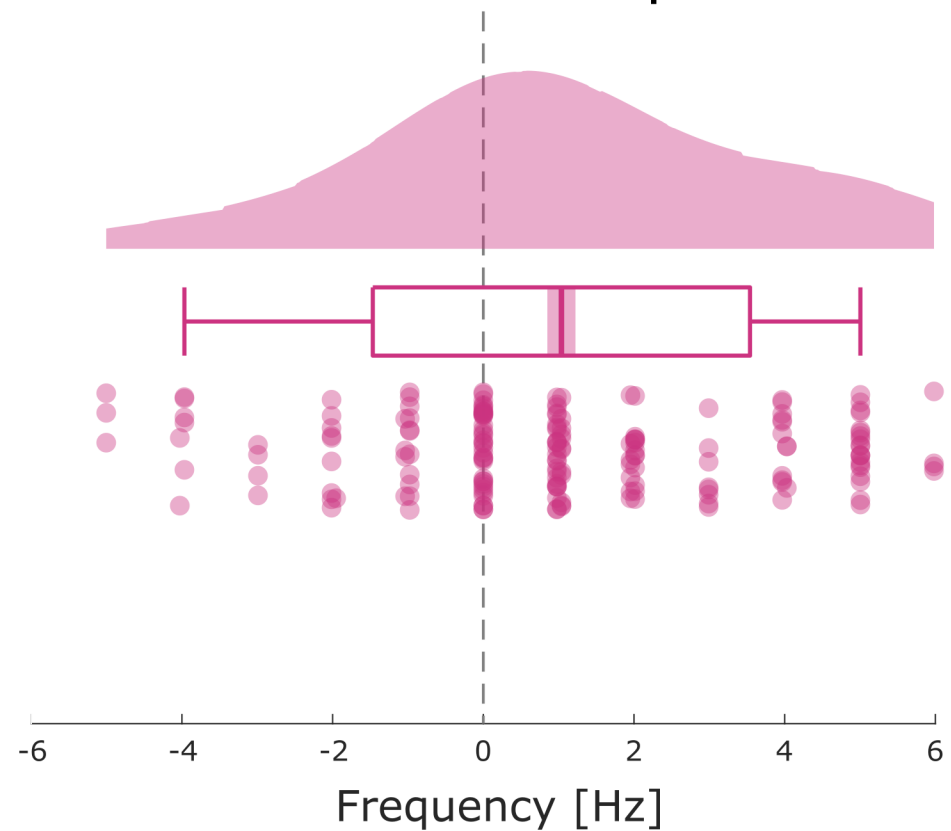
Hippocampus



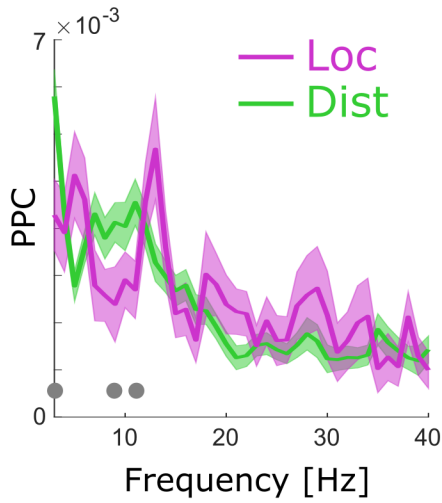
Peak SFC Theta



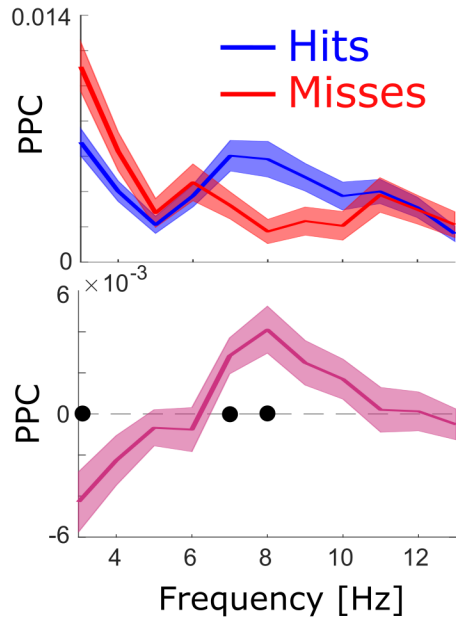
Peak Difference Hits vs Misses -- $p=4.9441e-08$



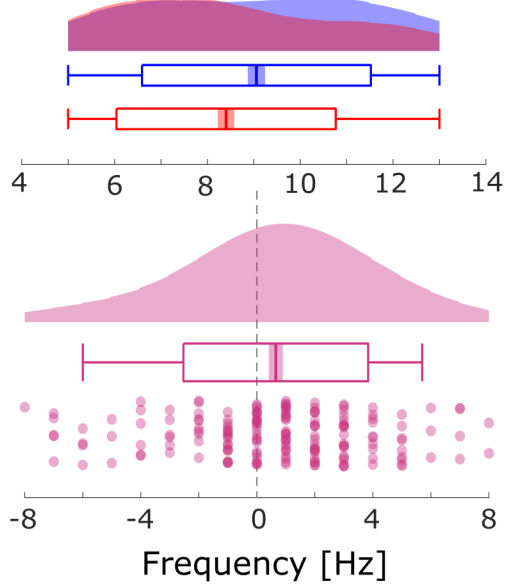
A



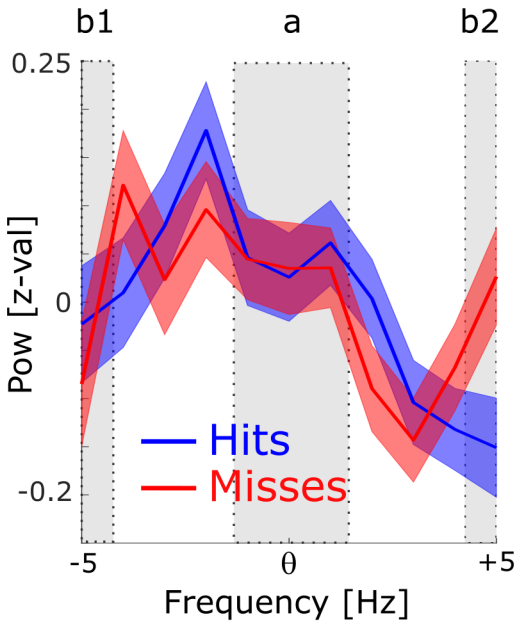
B



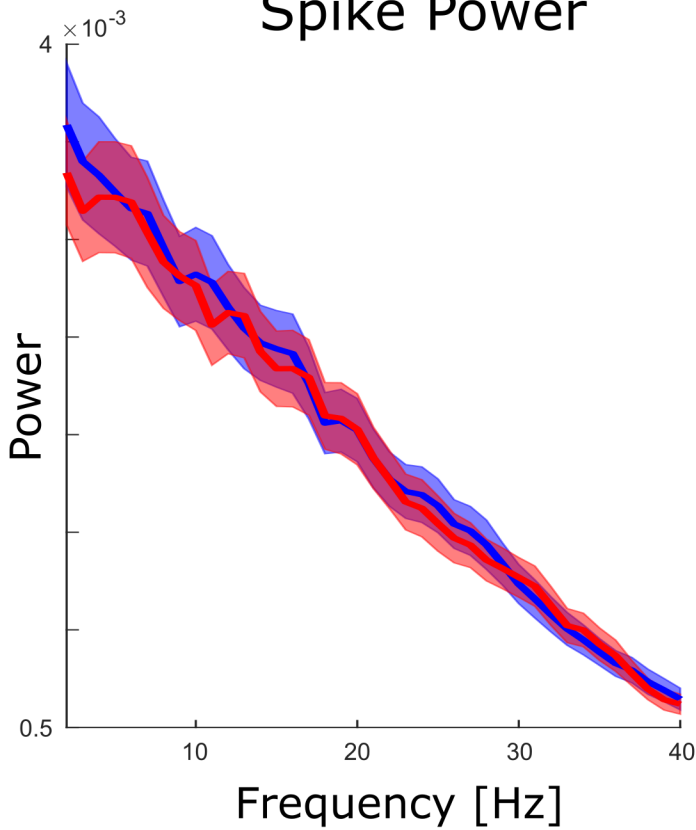
C

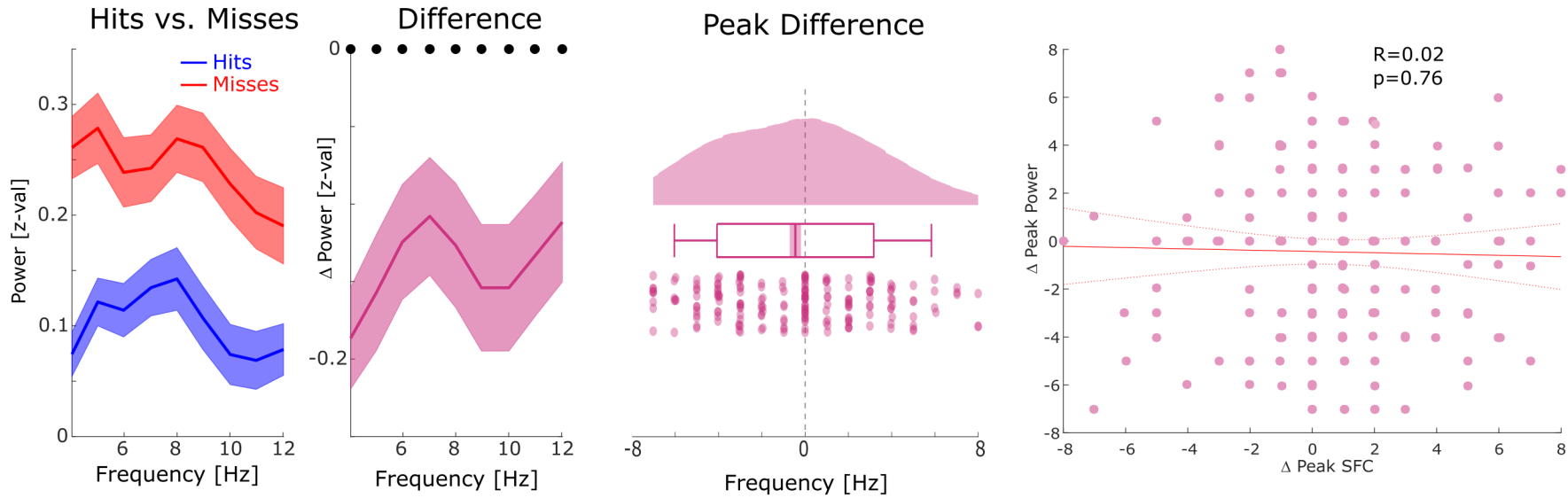


Theta Power

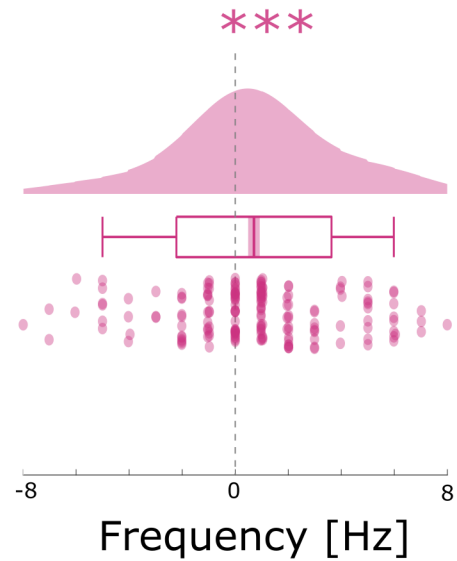
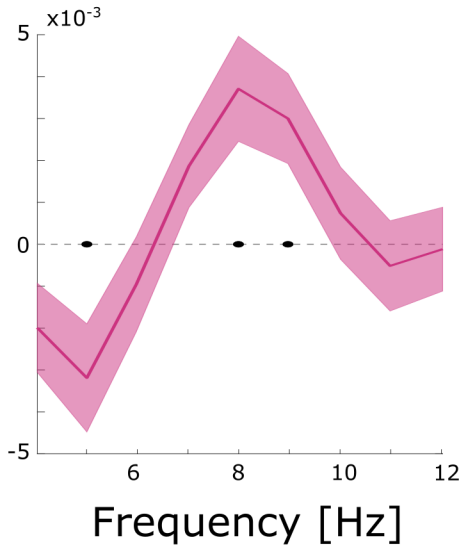
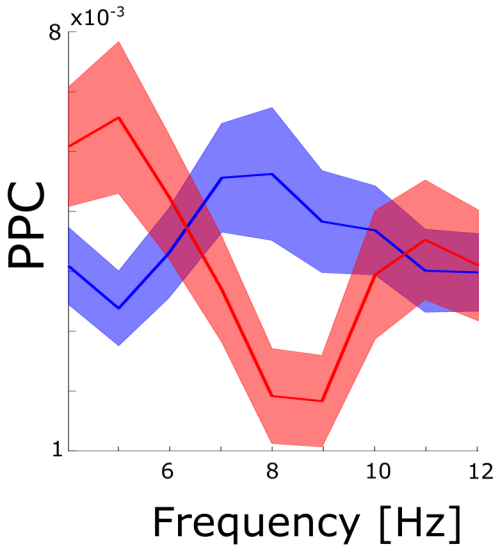


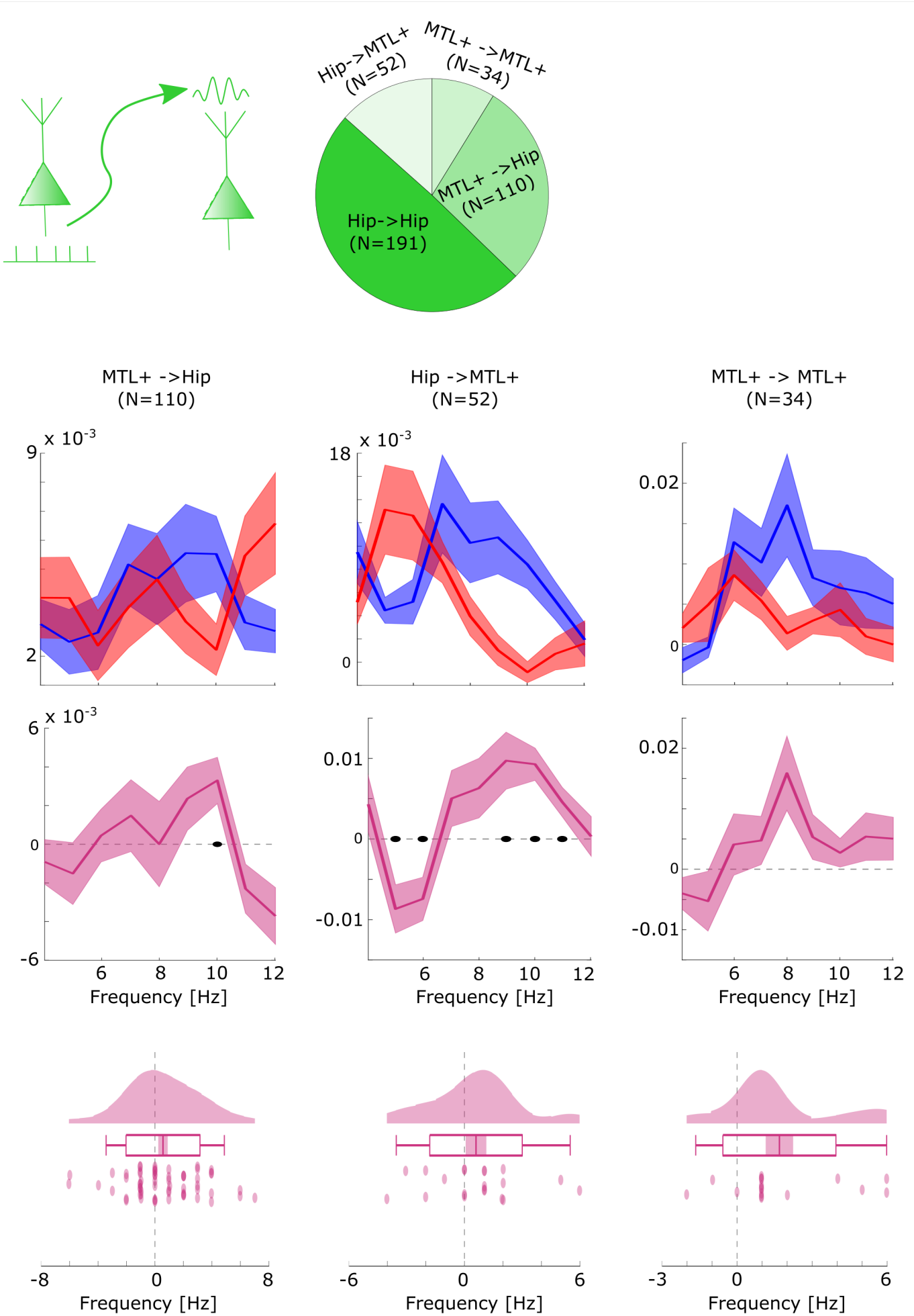
Spike Power

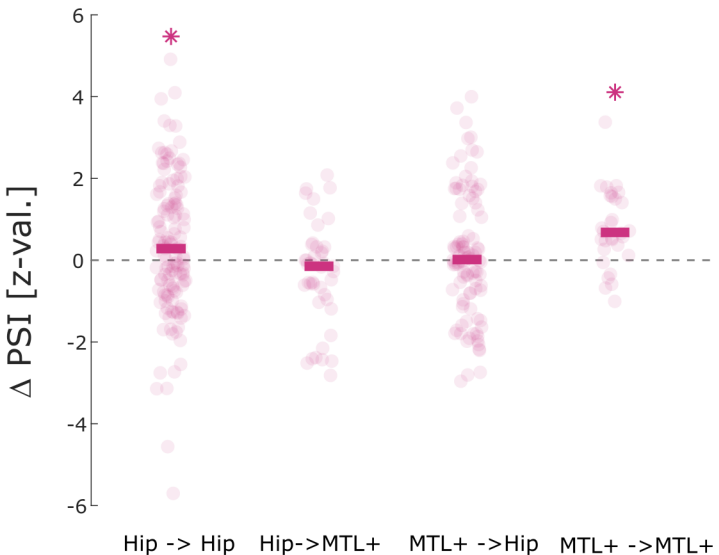
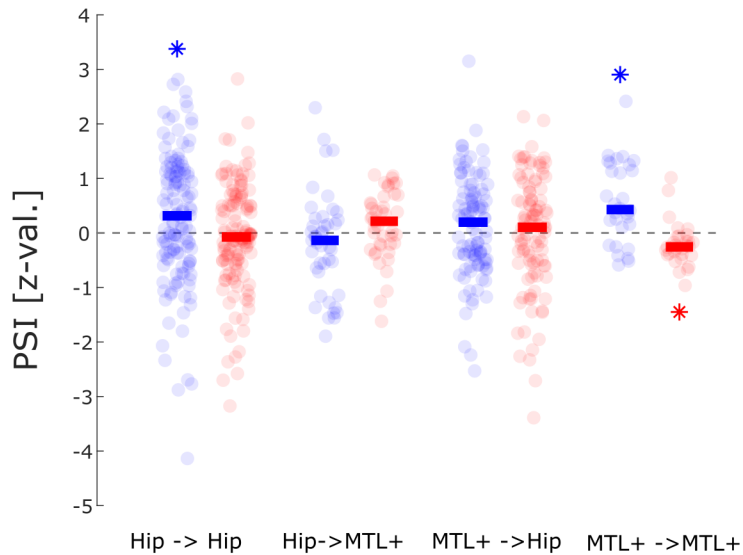


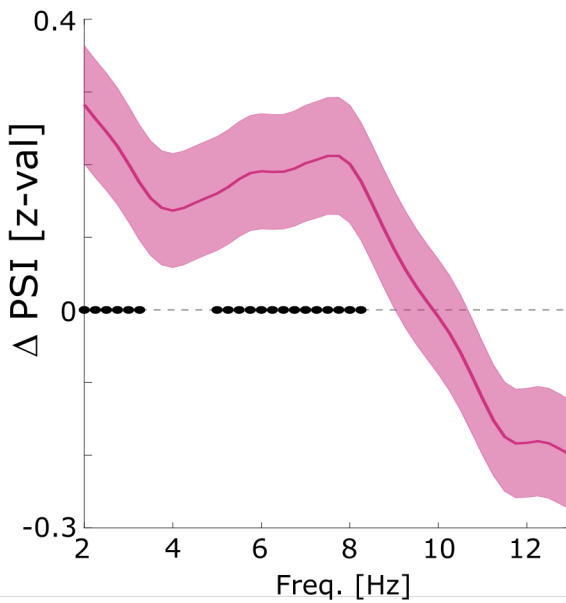
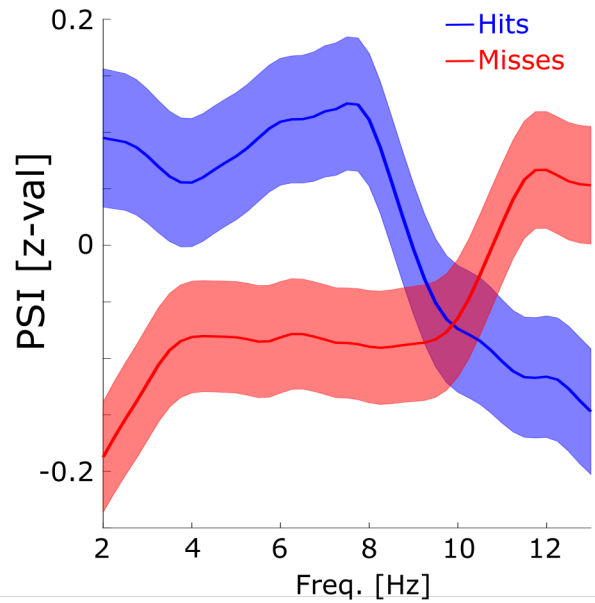


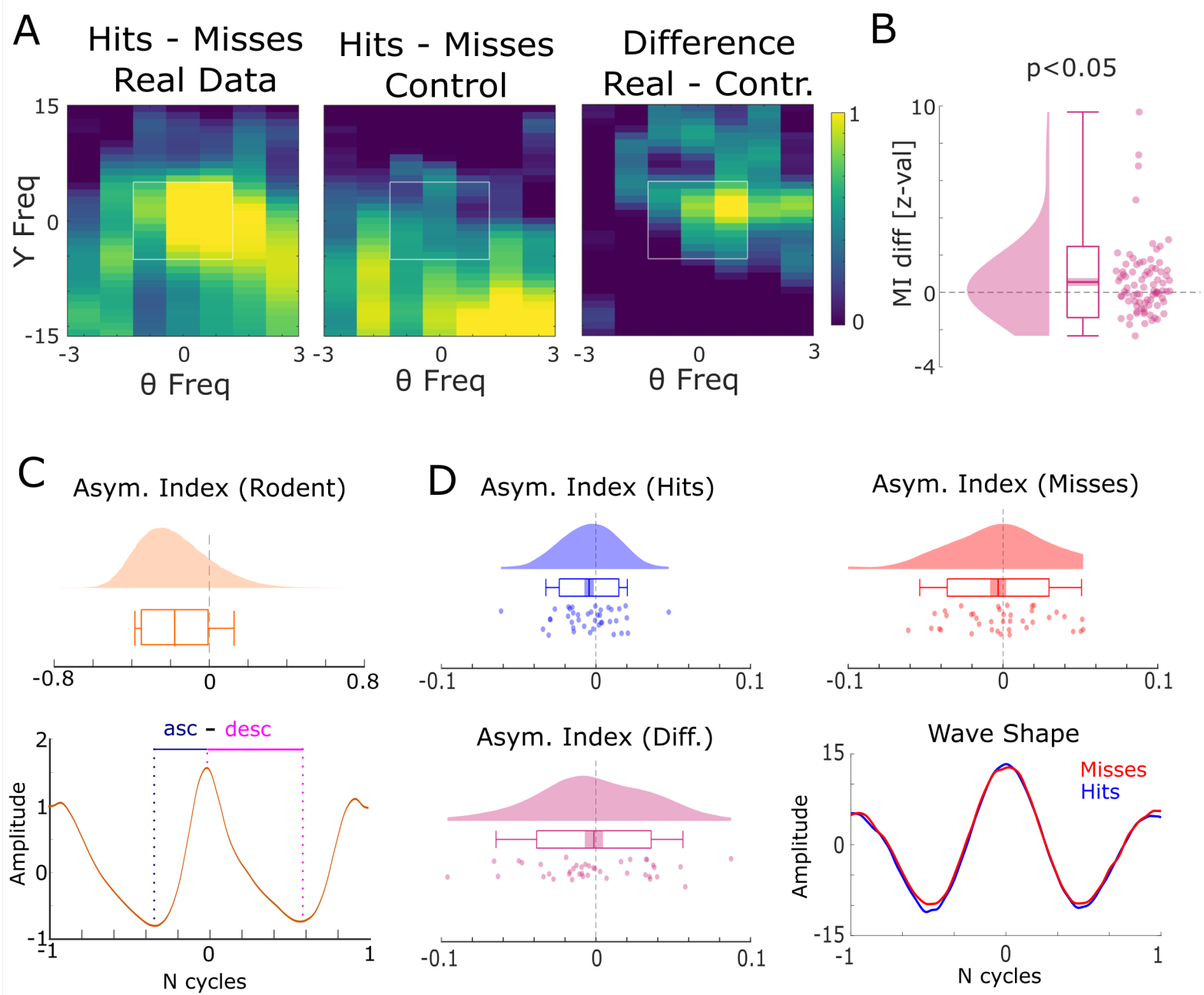
LFP from 'silent' M.W.

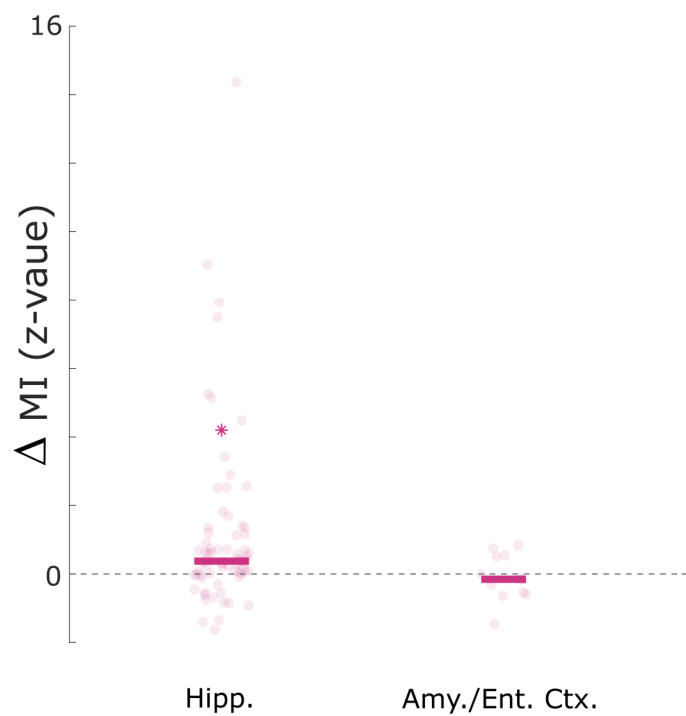
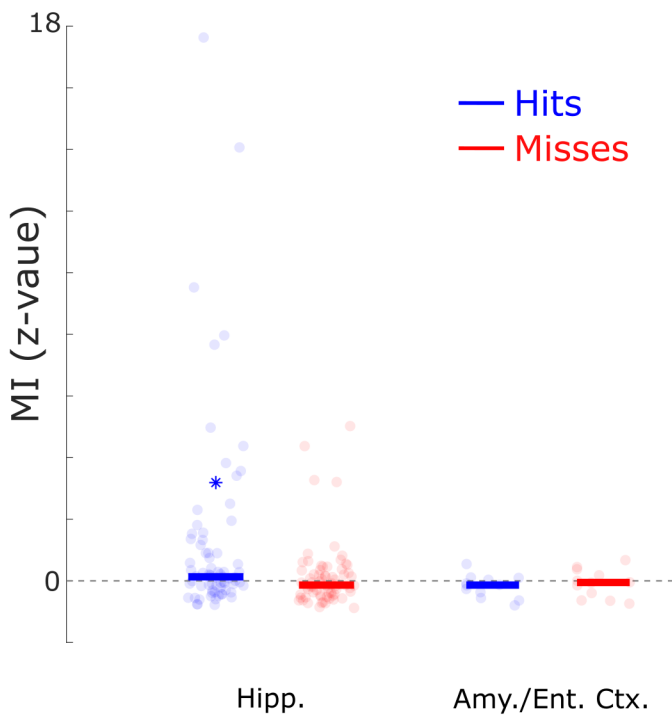
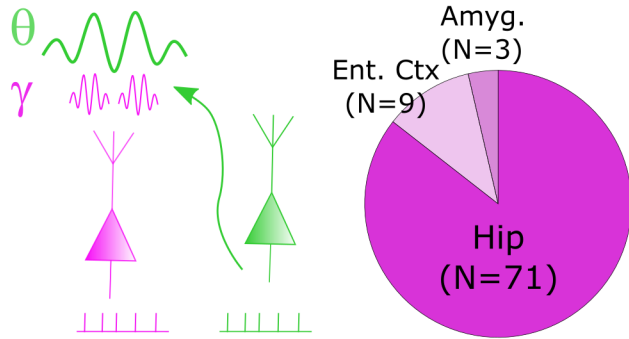


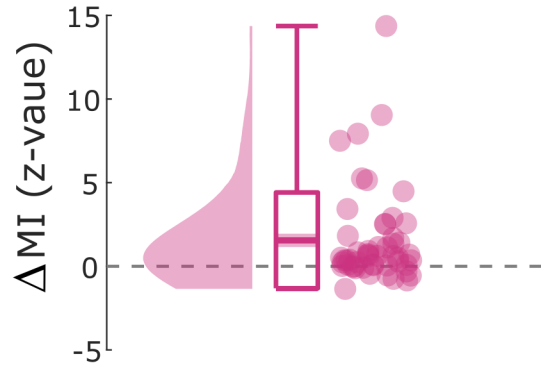
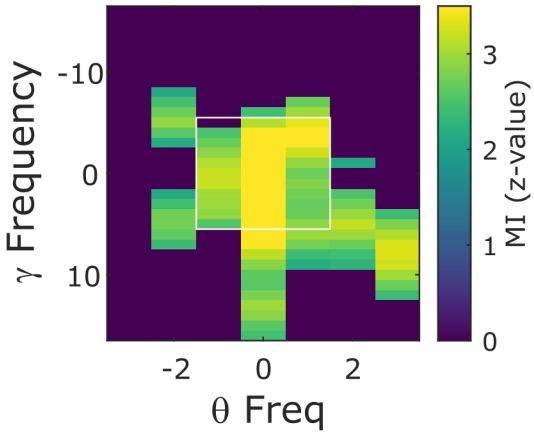


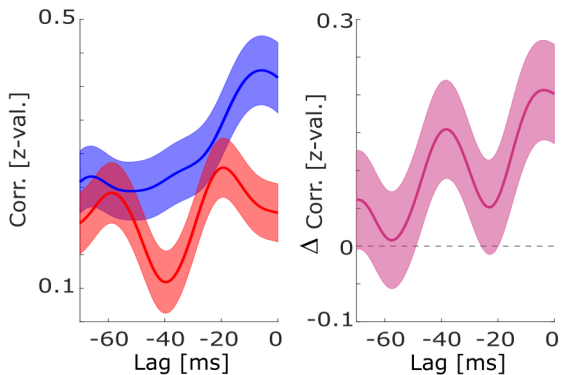
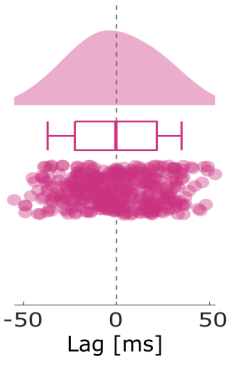
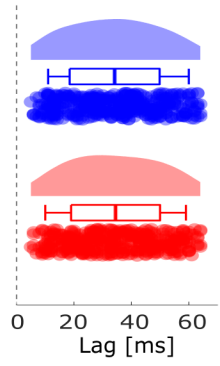
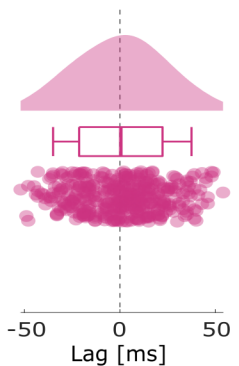
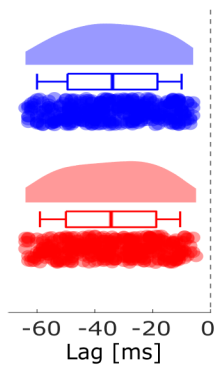
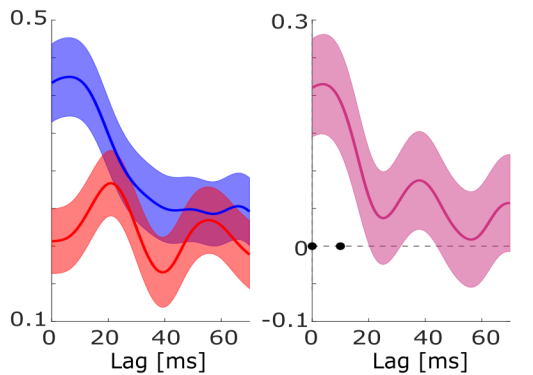


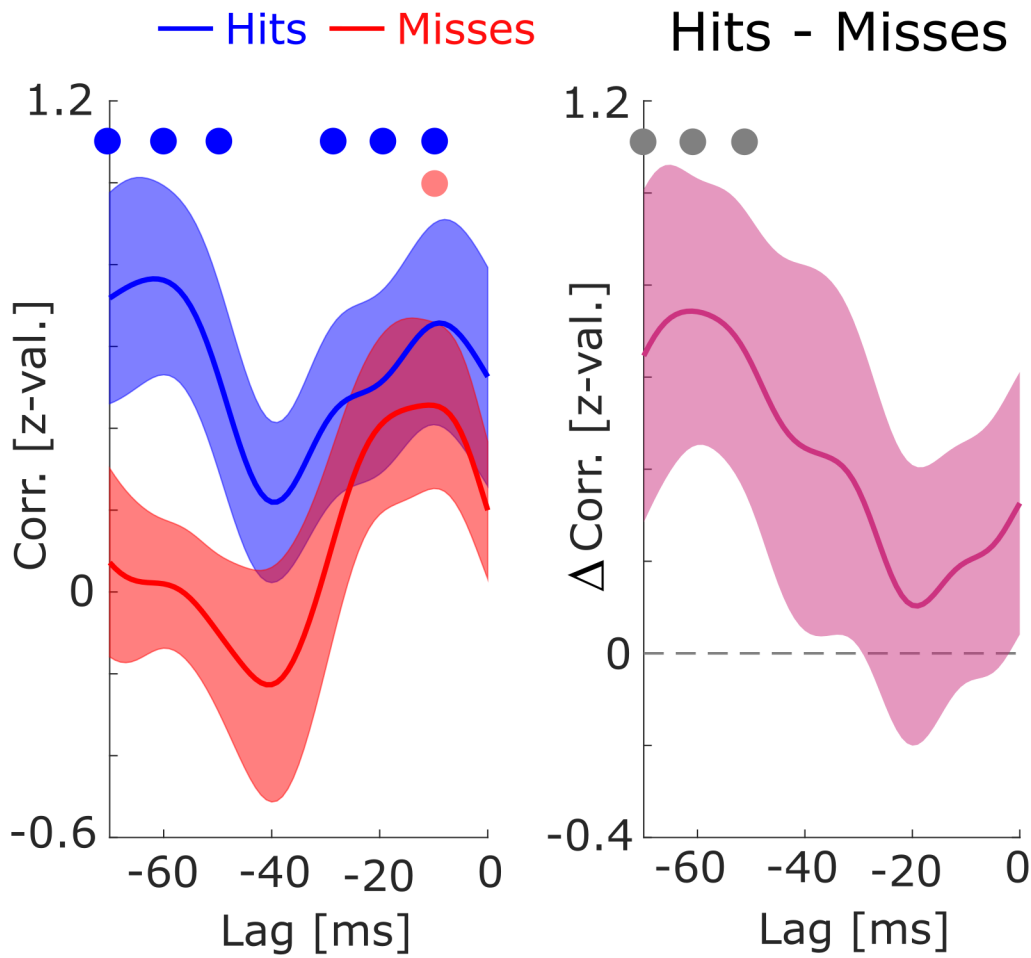
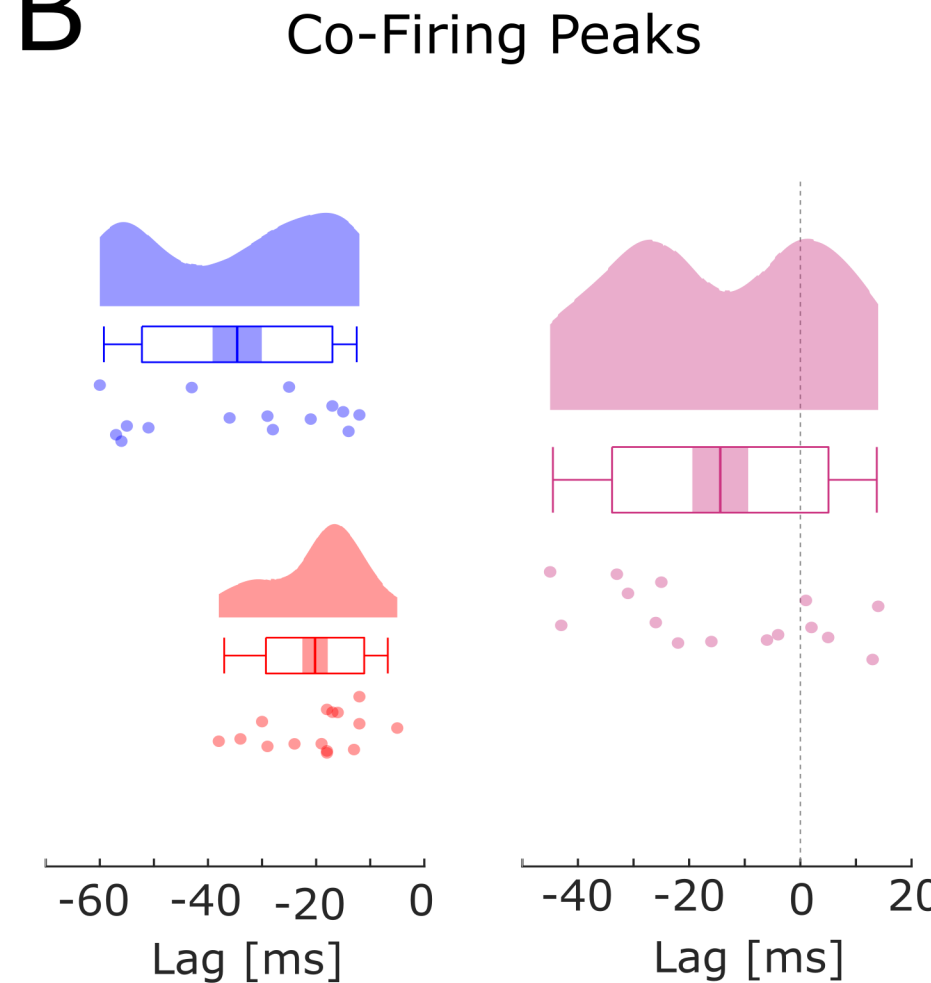
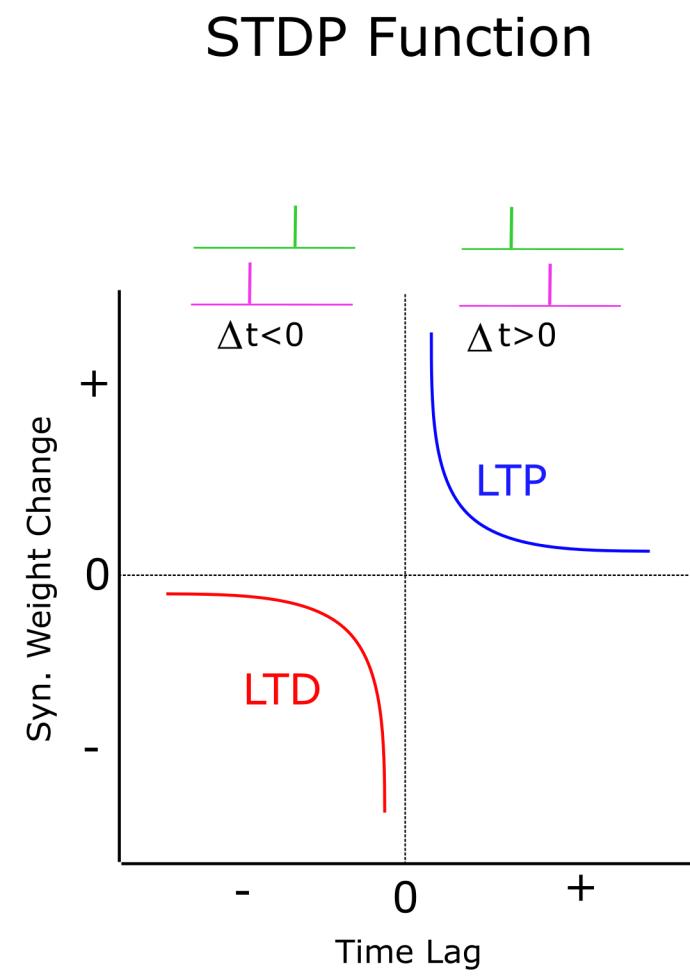




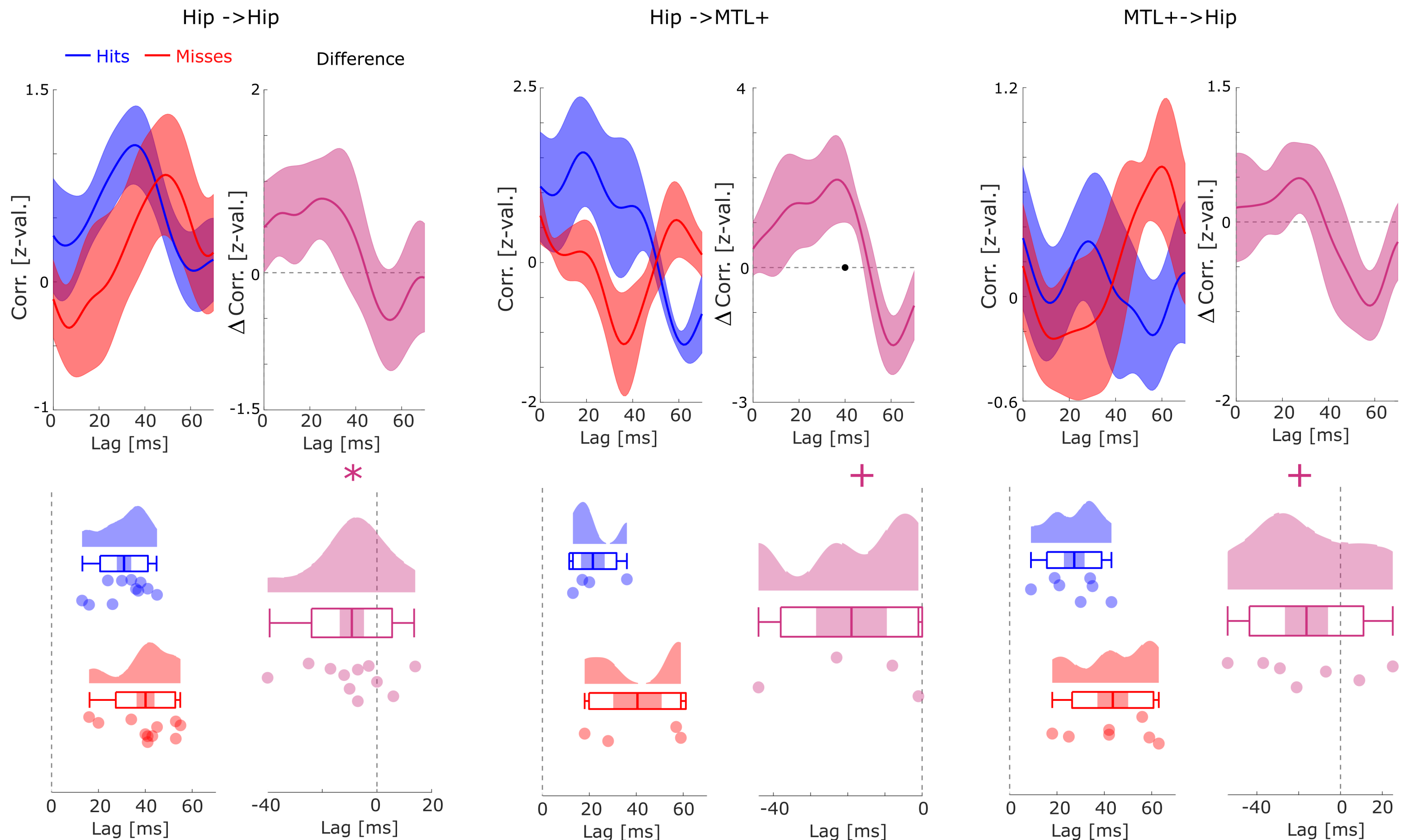
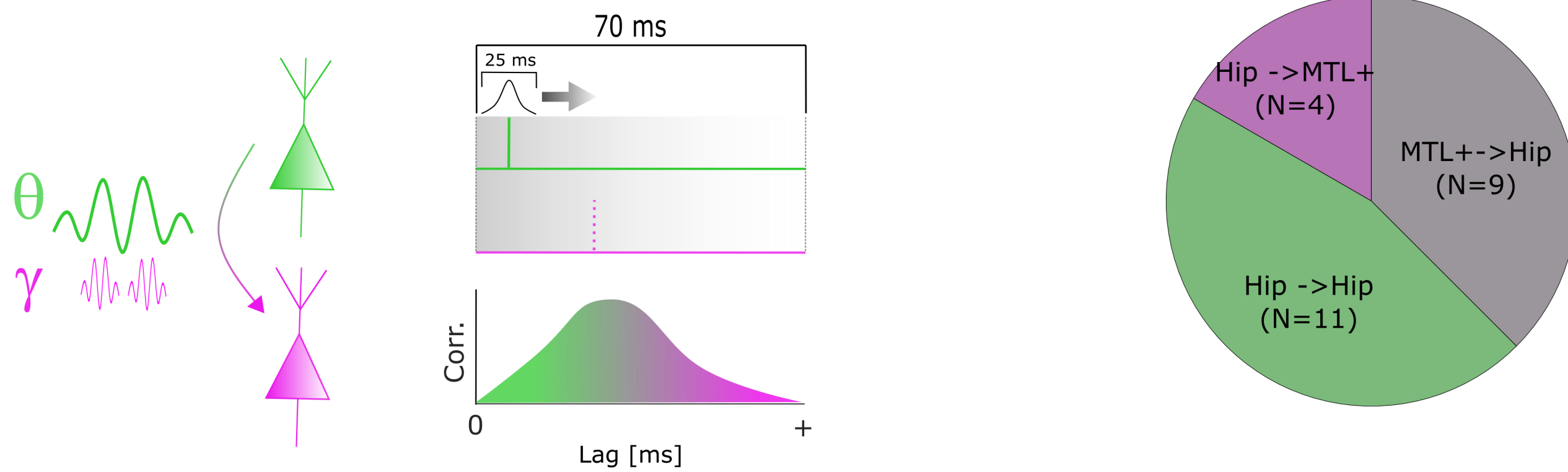




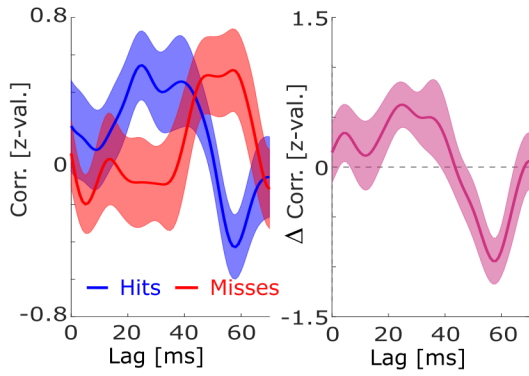
A**B**

A**B****C**

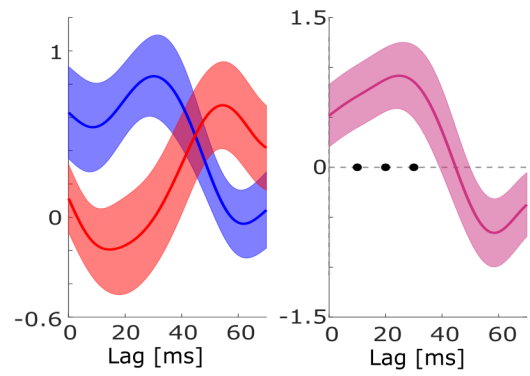
Spike Co-Firing Analysis



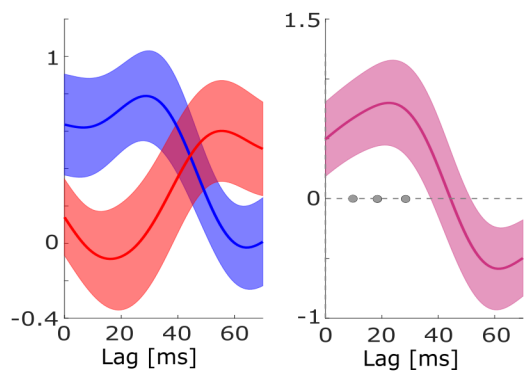
15 ms



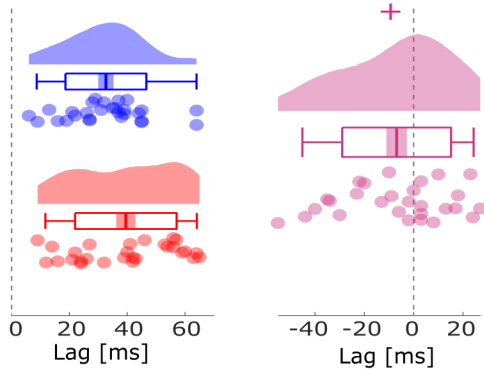
35 ms



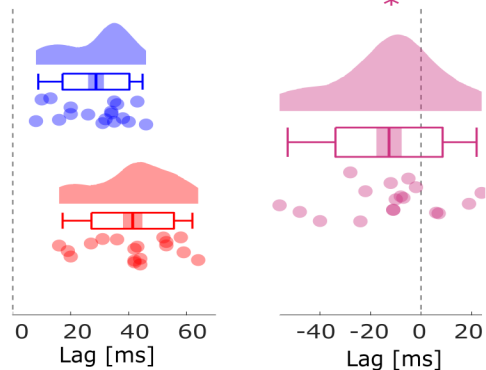
45 ms



+



*



*

